Bulk and Surface Radio-Frequency Response of Ice

By

Mark Stockham

Submitted to the Department of Physics and Astronomy and the
Graduate Faculty of the University of Kansas
in partial fulfillment of the requirements for the degree of
Doctor of Philosophy

David Besson, Chairperson

Christopher Allen

Committee members

Thomas Cravens

Douglas McKay

John Ralston

Date defended: June 15, 2018

The Thesis Committee for Mark Stockham certifies
that this is the approved version of the following thesis :

Bulk and Surface Radio-Frequency Response of Ice

David Besson, Chairperson

Date approved: August 22, 2018

Abstract

The flux and cross section of high energy neutrinos is an active area of research. Due to the expected low flux and cross section, interactions are rare and direct detection is ruled out. Large detector volumes with detection signals that can be observed from far away represent a reasonable and economical way to combat this problem. A currently popular detection strategy is to use a large, dense medium – such as ice – for the detector volume and radio antennas as the detectors. These radio antennas are sensitive to Cherenkov radiation produced via the Askaryan effect when a neutrino interacts in the detector volume. To determine the absolute amplitude of radio frequency (RF) emissions from high energy physics processes observed by Antarctic detectors, the bulk attenuation and surface reflection properties of Antarctic ice must be estimated. Neutrino experiments that intend to use polar ice as the detector volume must consider the depth-dependent attenuation length of the ice. Airborne experiments, such as the balloon-borne ANtarctic Impulsive Transient Antenna (ANITA), additionally need to consider the effects of the ice-air transition for both refracted signals produced by neutrino collisions in ice and reflected signals generated by cosmic ray-induced extensive air showers (EAS). Combining radar depth sounding (RDS) data for the estimation of attenuation length with radar scatterometer measurements for the estimation of surface roughness, we seek to create Antarctica-wide attenuation models. Though models and estimates for attenuation and reflection are motivated by ANITA analysis, the methods and results should have general use for the treatment of radio frequency signals interacting with ice and similar media.

Acknowledgements

I want to thank my parents for their guidance, support, and love. I thank my brother for providing a strong example of what to aspire to, even if I did not always follow directly. The greatest thanks to my wife Jessica for sharing her life with me and putting up with me as we have spent all of our years together as students. Thanks to Roland for making me laugh and giving me joyous breaks from school and work. Thanks to Margaret who was a nice gift we welcomed into our lives during the revision process of this dissertation.

Thank you to everyone who has tried to teach me something, especially Mr. Coleman, Mrs. Driskill, Mr. Geisert, and Mr. George. I can't imagine my life without the Department of Physics and Astronomy at KU and I'm thankful for all of the faculty and staff for making it such a unique, friendly, and lively atmosphere. I'm thankful to have had such helpful, intelligent, and friendly labmates through the years. I'd especially like to thank Michael, Pat, Sam, and Steven for their companionship on this long journey. Thanks to the whole ANITA crew, it was great being deployed with you all.

I thank my committee members for their patience and dedication to trying to improve my work. I'm especially indebted to Dr. McKay for his thorough edits of my very rough draft. I owe a great deal of thanks to Dr. Dave Besson for giving me the opportunity to conduct research and participate in some very rewarding collaborations, for answering the many thousands of emails over all of these years, giving me direction and perspective when needed, and jamming. His help with this document was indispensable.

Contents

List of Figures

List of Tables

Chapter 1

Physics Background

1.1 Introduction

The ANtarctic Impulsive Transient Antenna (ANITA) is a balloon-based experiment that flies "around the world" (at a latitude of $\approx 80^{\circ}$S) looking for radio frequency signals produced by neutrino interactions with the Antarctic ice shelf and Ultra-High Energy Cosmic Ray (UHECR) interactions with the atmosphere above Antarctica (see [1] for extensive overview). ANITA-3 flew during the 2014 Austral Summer season for 22 days. ANITA is made up of many antennas (48 channels each of vertically polarized and horizontally polarized) that allow for the use of the interferometric technique. The received voltage time series in each channel can be time-shifted to "steer" the pointing direction of the array as a whole. In this way, signals that are received on many channels can be shifted for maximum correlation with the resulting shifts corresponding to a unique arrival direction. For cosmic rays the most likely signal path is a downward-pointing extensive air shower (EAS) leading to a charge separation that radiates radio frequencies via the geosynchrotron effect [2] as well as the Askaryan effect. ANITA would see such a signal as it is reflected off of the ice surface and would appear as upward-traveling. Understanding how the ice surface reflects the entire spectrum that ANITA is sensitive to (200-1200MHz), as a function of location, is important for reconstructing such events. Neutrino interactions occur in the bulk ice and their Askaryan RF signals [2] would also appear to ANITA as upward-traveling, but primarily vertically polarized compared to primarily horizontally polarized for the CR reflected signals. When a neutrino interacts with the ice it produces a clump of charge that radiates coherently, this is the Askaryan effect. Such neutrino signals will have traveled up to 4km in ice, which is not entirely RF transparent. Colder ice, near the surface, typically has attenuation lengths of 1200m or more, while the deep ice near $0°C$ will have far shorter attenuation lengths of only several hundred meters (see Section 2.5). Developing a location-dependent attenuation length depth profile is essential in reconstructing the neutrino events observed by ANITA to estimate the energy of the incoming neutrino. Thus far, ANITA has not seen any neutrino events, so understanding the attenuation length of all of the ice within view of ANITA is required to accurately estimate sensitivity to the neutrino flux in the range to which ANITA is sensitive ($10^{18} - 10^{25} eV$).

1.2 Cosmic Rays

1.2.1 Introduction

Cosmic rays are relativistic particles that range from protons to iron nuclei ($Z = 1 \rightarrow Z = 28$), with the mass spectrum being an area of active research. For Ultra-High Energy (UHE) cosmic rays ($E > 10^{18} eV$) the source acceleration mechanisms are not well known, though there are some candidates (gamma-ray bursts, neutron stars, and active galactic nuclei, for example). Even though they possess charge, if the energy is high enough the cosmic ray path does not deviate much due to intergalactic and galactic magnetic fields as it travels, and thus should point back to its source. The deflection of the cosmic ray is proportional to the magnitude of the magnetic field it is traveling through, the distance it travels, and its charge, while being inversely proportional to the energy of the cosmic ray. When a cosmic ray collides with an atmospheric particle an explosion of secondary particles occurs, known as an Extensive Air Shower (EAS). After initial hadronic interactions, many electron-positron pairs are produced, after which, via the Askaryan effect, the electron population begins to dominate over positrons. As these clumps of charge interact with the magnetic field lines of the Earth, radio-frequency radiation is generated along a cone in the direction of the acceleration. Since this resembles synchrotron radiation this process is known as geosynchrotron radiation. Due to the near-vertical alignment of the magnetic field lines in Antarctica, this radiation is nearly purely horizontally polarized (h-pol).

Cosmic ray-induced extensive air showers can also lead to Askaryan radiation [3], but it is believed to be weaker than the geosynchrotron radiation because only the charge excess particles contribute, compared to all charged particles in the geosynchrotron case [2].

1.2.2 Flux

Since the second decade of the 20th century cosmic rays have been an active research topic in physics. The contemporary research is focused on determining the energy spectrum, composition of the primary particles, and the original sources of the cosmic rays. The flux as measured by several experiments is shown in Figure 1.1. The equivalent center of mass energy for collisions at the Large Hadron Collider are approximately an order of magnitude below the energies in the labeled "ankle".

Above energies of 10^{10} eV the cosmic ray energy spectrum, given by the equation

$$J(E) = \frac{d^2\phi(E)}{dEd\Omega} \approx \left(\frac{E}{eV}\right)^{-\gamma} \tag{1.1}$$

follows a broken power law, with spectral index (γ) ranging in value from $\approx 2.6-3$. The breaks in the power law consist of "the knee" at $10^{15.5}$ eV where γ changes from ≈ 2.7 to ≈ 3 and "the ankle" at $10^{18.5}$ eV where γ changes back from ≈ 3 to ≈ 2.6. The measured flux beyond energies of 10^{19} eV is lower than the continuation of this power law but suffers from very low statistics.

The features of the spectrum can be partially explained by changes in composition and accelerating mechanism, as well as energy-loss mechanisms. At energies beyond the knee, there is an apparent lack of accelerating sources within the galaxy and for energies below the the knee, the galaxy acts to confine the cosmic rays [5]. The cutoff at the high energies are likely due to in-

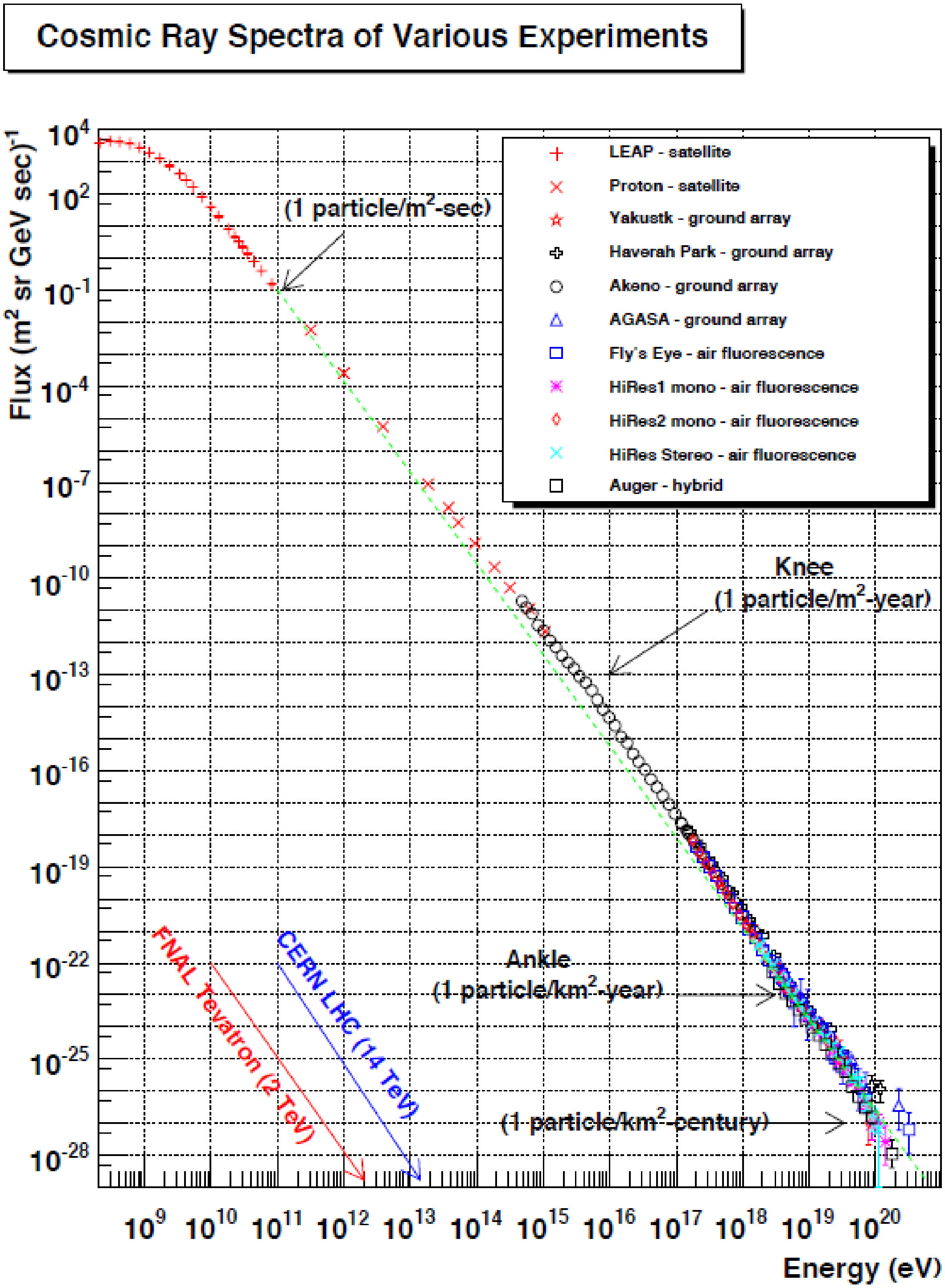

Figure 1.1: The cosmic ray energy spectrum as measured by multiple experiments. The $\gamma = 3$ spectrum is shown in the dashed line. Figure from [4].

teractions between high energy cosmic rays and the cosmic microwave background (CMB). If the cosmic ray is a heavy nucleus, the CMB photons attenuate the energy of the cosmic ray by the following processes, representing photodisintegration and pair creation [6]

$$\begin{aligned} A+\gamma_{CMB} &\rightarrow (A-1)+N \\ A+\gamma_{CMB} &\rightarrow (A-2)+2N \\ A+\gamma_{CMB} &\rightarrow A+e^{-}+e^{+}. \end{aligned} \tag{1.2}$$

All of these interactions reduce the energy of the cosmic ray while the first two also skew observed cosmic rays to lighter nuclei than their sources. For protons, Greisen, Zatsepin, and Kuzman (GZK) independently predicted a high-energy cutoff [7, 8]. Protons of energy $\sim 5\times10^{19}$ eV see a CMB photon as having 300 MeV energy due to blueshift. This is the threshold for photopion production through the delta resonance[6], shown below

$$\begin{aligned} p+\gamma_{CMB} &\rightarrow \Delta^{+} \rightarrow n+\pi^{+} \\ p+\gamma_{CMB} &\rightarrow \Delta^{+} \rightarrow p+\pi^{0} \end{aligned} \tag{1.3}$$

The mean free path for a proton above the delta resonance threshold energy traveling through CMB photons is 8Mpc [9]. Each time the CR interacts with the CMB photons on average its energy is reduced by 20% until the point that it is below the delta resonance interaction threshold energy. This creates a relative excess of $10^{20}eV$ CR known as the GZK pile-up. For CR with energy less than the delta resonance threshold, most of the energy loss comes from pair production (with a threshold of 800 PeV, where a "second knee" has been observed) and from redshift propagation loss [5]. This is a possible cause of the steepening of the spectrum after the ankle. Figure 1.2 shows the energy of several UHE protons as they propagate. The implication is that CRs with energies above the GZK cutoff must originate within $\sim$ 100Mpc.

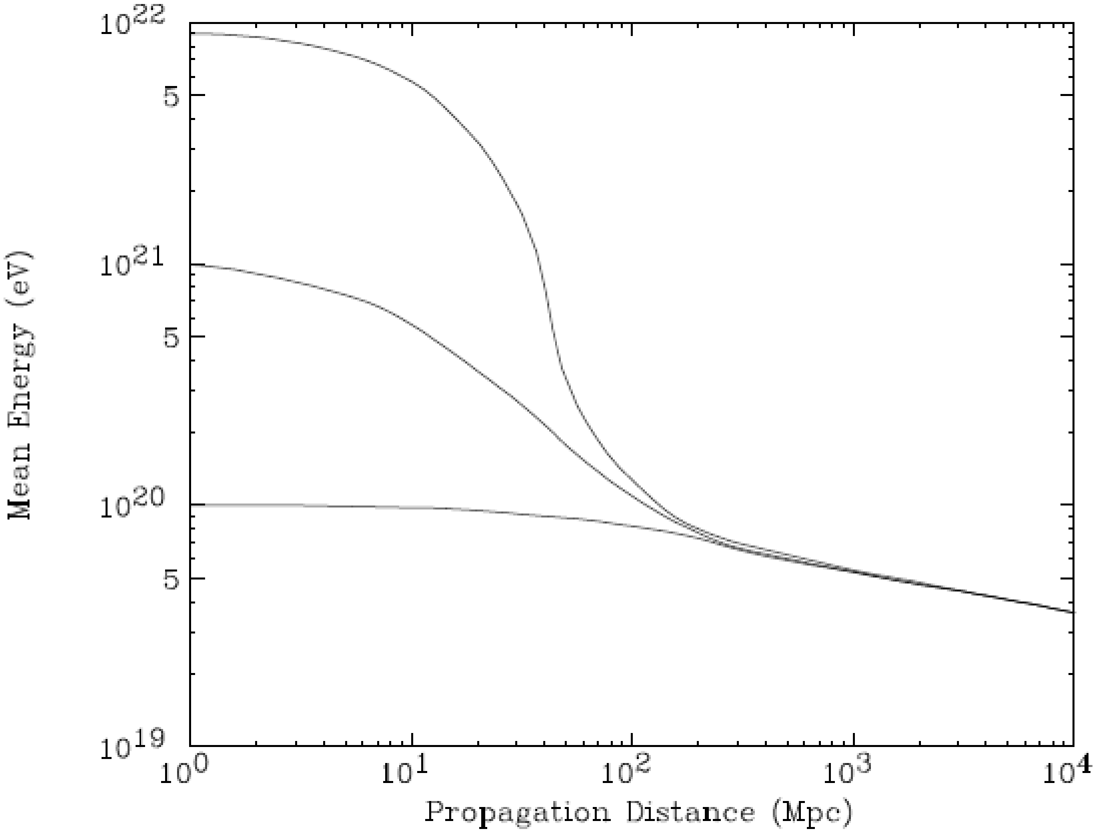

Figure 1.2: The effect of CMB interactions on UHE cosmic rays as they propagate. The delta resonance with a mean free path of ∼ 8Mpc will eventually bring all CRs to that threshold energy, the GZK cutoff. Below that threshold pair production acts to further attenuate the energy. Figure from [10].

1.2.3 Possible Sources

Two general approaches are taken to explain sources of UHECR, they can either be the byproduct of higher energy interactions (top-down) or they may be accelerated by very strong magnetic fields (bottom-up). Figure 1.3 shows the proposed possible sources based on radius of the source and its magnetic field strength (Hillas plot). There are possible sources to explain the acceleration of protons to energies up to $10^{21} eV$, or heavier nuclei up to $10^{20} eV$. The reasoning behind the Hillas plot is that it balances accelerating mechanisms against the strength of the magnetic field that contains the CR until it has reached a threshold energy, that is that the Larmor radius must be smaller than the size of the accelerating mechanism, $r_L = \frac{\varepsilon_{CR}}{q_{CR} B_S} \leq R_s$. This constraint means that if a candidate accelerator has a small radius, it must posses a very large magnetic field to contain the particle. Conversely, mechanisms that accelerate a cosmic ray via a weak magnetic field would be required to have a large radius of acceleration.

1.2.4 Anisotropies

Determining the arrival direction of UHECR is key to the efforts of identifying the sources (acceleration mechanisms). Due to the magnitude of the galactic magnetic field, it is unlikely that UHECR could be accelerated to energies > $10^{19} eV$ within the galaxy. Recent studies have not shown with high significance any concentration of UHECR originating in the galactic plane. Since the sources of the highest energy cosmic rays is likely to be extragalactic, their paths will be influenced by galactic and intergalactic magnetic fields as they travel. As the amount of deflection the cosmic ray undergoes is inversely proportional to its energy, this makes the highest energy cosmic rays even more interesting as they will more directly point to their source. The strategy thus far for investigating candidate sources of UHECR has been to correlate maps of UHECR arrival directions with maps of the locations of known energetic sources (of which there is a finite number within the GZK horizon).

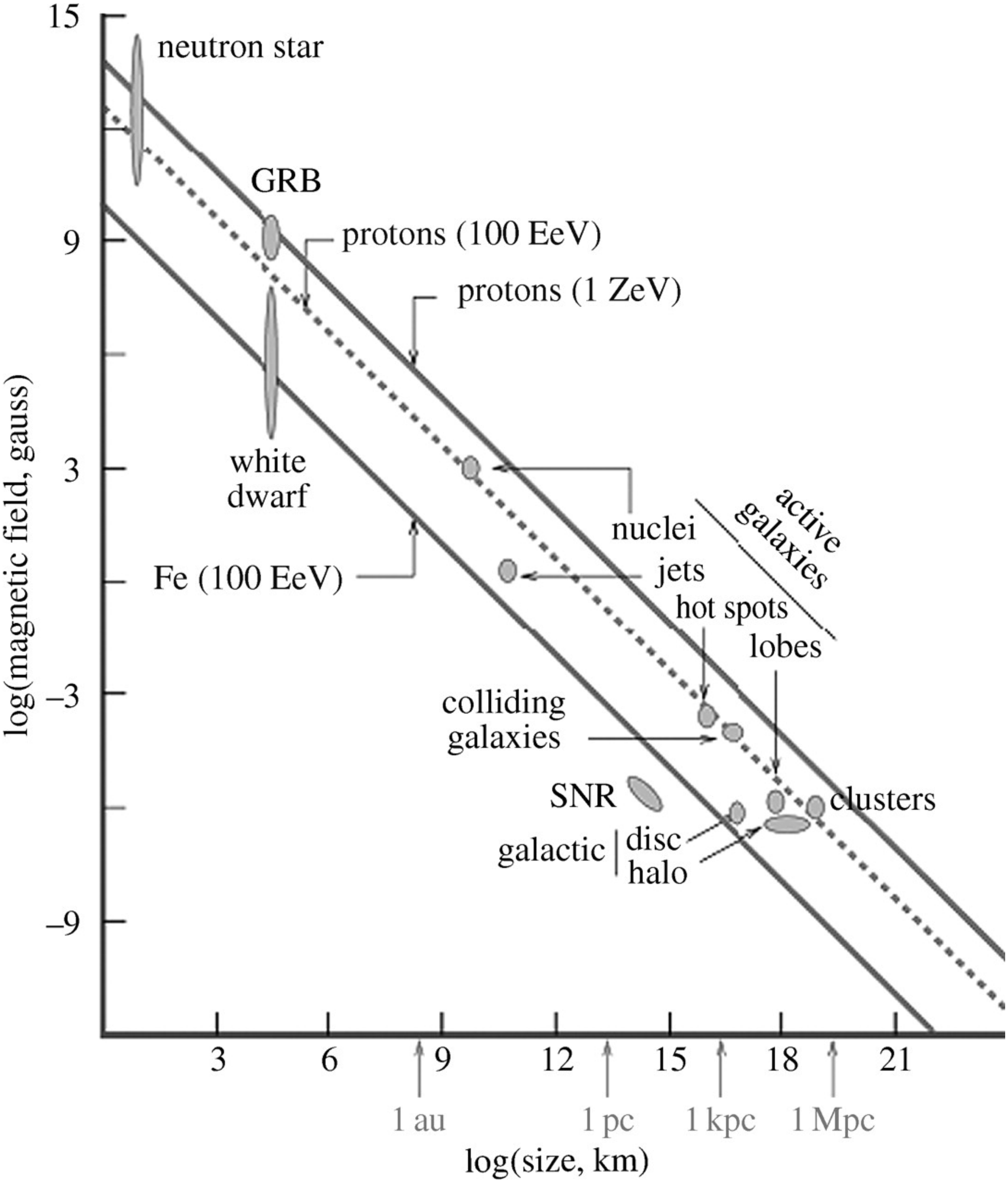

Figure 1.3: Proposed sources of acceleration of UHE cosmic rays with their radius and magnetic field strength. Figure from [11].

1.2.5 Cosmic Ray Mass Spectrum

Knowing the mass distribution (from proton to iron nuclei) of arriving cosmic rays would allow for more constraints to be put on candidate sources. CRs with energies <10^{16}eV can be directly measured with spectrometers and calorimeters on satellites. Of course, the flux is too low for this to be practical for higher energies. For higher energies, we must resort to indirect detection techniques (as for determining flux). Simulations of EAS evolution indicate that composition can be determined from shower characteristics, namely the depth at which the shower population is maximal (Xmax) and the number of secondary muons [12].There are some differing results based on experiment, [13] shows proton-dominated mix at the knee, changing to heavier nuclei at 10^{17}eV, then switching back to lighter nuclei at $10^{18} eV$. The Auger experiment suggests light nuclei dominate from $10^{18} - 10^{18.5}$eV [14] and heavier nuclei dominant above $10^{18.5}$eV [15]. Telescope Arrays results are still consistent with protons in this range [16].

These composition results are not fully resolved and are an active area of research.

1.3 Neutrinos

Neutrinos are electrically neutral fundamental particles with small interaction cross section. The flux of low energy neutrinos (solar neutrinos) is approximately 10^{11} neutrinos per square centimeter per second, and falling as a power law of the neutrino energy. This low flux at high energies, combined with a small interaction probability requires a large interaction volume for an interaction to occur in a reasonable experimental time frame. Because of the large available volume, low background noise levels, and relative RF transparency, Antarctic ice offers a suitable detector volume. When a neutrino interacts with a particle in the ice it creates many secondary particles. After several generations of reactions, many electron-positron pairs are created. Interaction with atomic electrons and inverse Compton scattering lead to a net-negatively charged cluster of particles about one Molière radius (10cm) wide traveling greater than the speed of light in ice. Radiation from this non-accelerating charge occurs along a cone as initially derived by Cherenkov and Vavilov (as an

EM shockwave). Radiation at wavelengths greater than the size of the cluster is emitted coherently due to the many discrete radiators that exist within the cluster. This was first noticed by Askaryan and the effect bears his name. The neutrinos that may be detected are downward moving through the ice, but are most probably at inclined angles (more effective ice) versus completely vertical. The angle also has to be sufficiently inclined that the signal is not totally internally refracted. Due to this inclined angle and the refraction from transitioning from ice to air, only the top portion of the Cherenkov cone will be observed, implying signals that are dominantly vertically polarized (v-pol).

Neutrinos that have cosmic origin and travel to Earth can come from many sources and can be categorized based on the source and the energy scale. The Sun gives a near-constant flux of low energy neutrinos as a result of nuclear fusion. A short-lived neutrino output increase happens as a result of supernovae, as shown with the detection of SN1987A. There are atmospheric neutrinos produced by cosmic ray interaction with air molecules in the atmosphere. Lastly, of the greatest energy and current interest, are astrophysical and cosmogenic neutrinos. Astrophysical neutrinos can be assumed to be produced by the same source that is accelerating UHECR. Cosmogenic neutrinos are those produced after pion decay from the interaction of cosmic rays with CMB photons (from 1.3)

$$\begin{aligned} \pi^+ &\rightarrow \mu^+ + \nu_\mu \\ \mu^+ &\rightarrow e^+ + \nu_e + \bar{\nu_\mu} \end{aligned} \tag{1.4}$$

As the neutrinos are uncharged, direct detection of the astrophysical and cosmogenic neutrinos would provide the best chance of pointing back to the source of UHECR. Currently, an extrapolated value of lower-energy neutrino cross-section is used for modeling and determining flux limits, but the flux and cross-section are, by default, measured in such a way that they are convolved.

1.4 Surface Waves

Due to the vertical polarization of the portion of the radiation likely to be observed, it is also possible that the neutrino-produced RF signals couple with the the ice-air interface and propagate as surface waves (the amplitude decreasing as the square root of distance) [17]. Surface-based measurements of these signals could potentially be made, but would still depend on ice properties to be calibrated. The attractiveness of this detection approach is two-fold, the geometrical spreading is cylindrical as opposed to spherical and the attenuation at the surface of the ice is at a minimum. Due to this relatively low signal loss, receiving stations can be set up at a lower density than englacial stations to have the same sensitivity. The cost reduction due to fewer stations would be further enhanced by the much less expensive option of very shallow radio stations (like the Antarctic Ross Ice-Shelf ANtenna Neutrino Array) compared to drilling hundreds of meters into the ice.

A consequence of the coupling of these surface waves is that they will have a group velocity greater than the speed of light [17]. This implies that an observation of an index of refraction < 1 for an incoming signal would support evidence for surface wave transmission taking place. Further evidence would be the tell-tale amplitude fall off of $1/\sqrt{r}$ as opposed to $1/r$. Preliminary work (arXiv:1509.04997) has been done to look for this, trying to excite surface waves along the walls in a rock salt mine, over the surface of a sand volleyball court, and in a pool of water doped with various concentrations of salt. Thus far, the measured indices of refraction for these materials have been lower than expected, but none have been < 1. Also, the expected “boost" of a factor of $\sqrt{r}$ has not been observed. Ideally, further study will be done on the Antarctic ice sheet.

1.5 ANITA

The ANtarctic Impulsive Transient Antenna is an international collaboration that started as a neutrino telescope that used the Antarctic ice sheet as the detector volume. This is accomplished by flying RF antennas and a Data Acquisition System (DAQ) on a gondola attached to a long duration balloon. The first full flight of ANITA consisted of 32 dual-polarization horn antennas and a DAQ that was designed to trigger on pulses in either polarization. ANITA-1 flew for 35 days and while no neutrinos were found in analysis the upper limit on the neutrino flux in the energy regime to which ANITA-1 is sensitive was improved upon. A fortunate byproduct of the neutrino search was that 16 cosmic ray events were identified in analysis (14 reflected from the ice surface, 2 direct events). The triggering scheme for ANITA-2 was changed to eliminate h-pol triggers before these cosmic ray events were identified, so unfortunately ANITA-2 only observed 4 cosmic ray events even though it flew for 31 days. Like ANITA-1, ANITA-2 did not observe any UHE neutrinos, but further reduced the upper limit in the relevant energy regime. With ANITA-3 the h-pol triggers were re-instituted so that there would be more cosmic ray triggers and 18 CR signals were observed. ANITA-4 analysis is currently being conducted.

Chapter 2

Glaciology Background

2.1 Introduction

Properties of Arctic and Antarctic ice are a currently rich area of research. Most of this research is intended to answer the questions of climate history, as well as recent changes in ice depth and flow. As a correction to some of these measurements, the RF attenuation length (distance of travel required to reduce amplitude by a factor of $\frac{1}{e}$) is a quantity of interest. The most common method for measuring the attenuation length is to measure the amplitude of a bedrock-reflected signal and compare it to the known output amplitude of the signal. This can result in the so-called “depth averaged” attenuation length, which represents what the value of attenuation length would be if it was constant as a function of depth to produce the attenuation observed in the basal reflection. There are no robust methods to estimate the depth-dependent attenuation length currently in the glaciology literature. The Center for Remote Sensing of Ice Sheets (CReSIS, [18]) has a large data repository with ice thickness data in the form of echograms (Fig. 2.1) that can potentially be repurposed for depth-dependent attenuation length estimates.

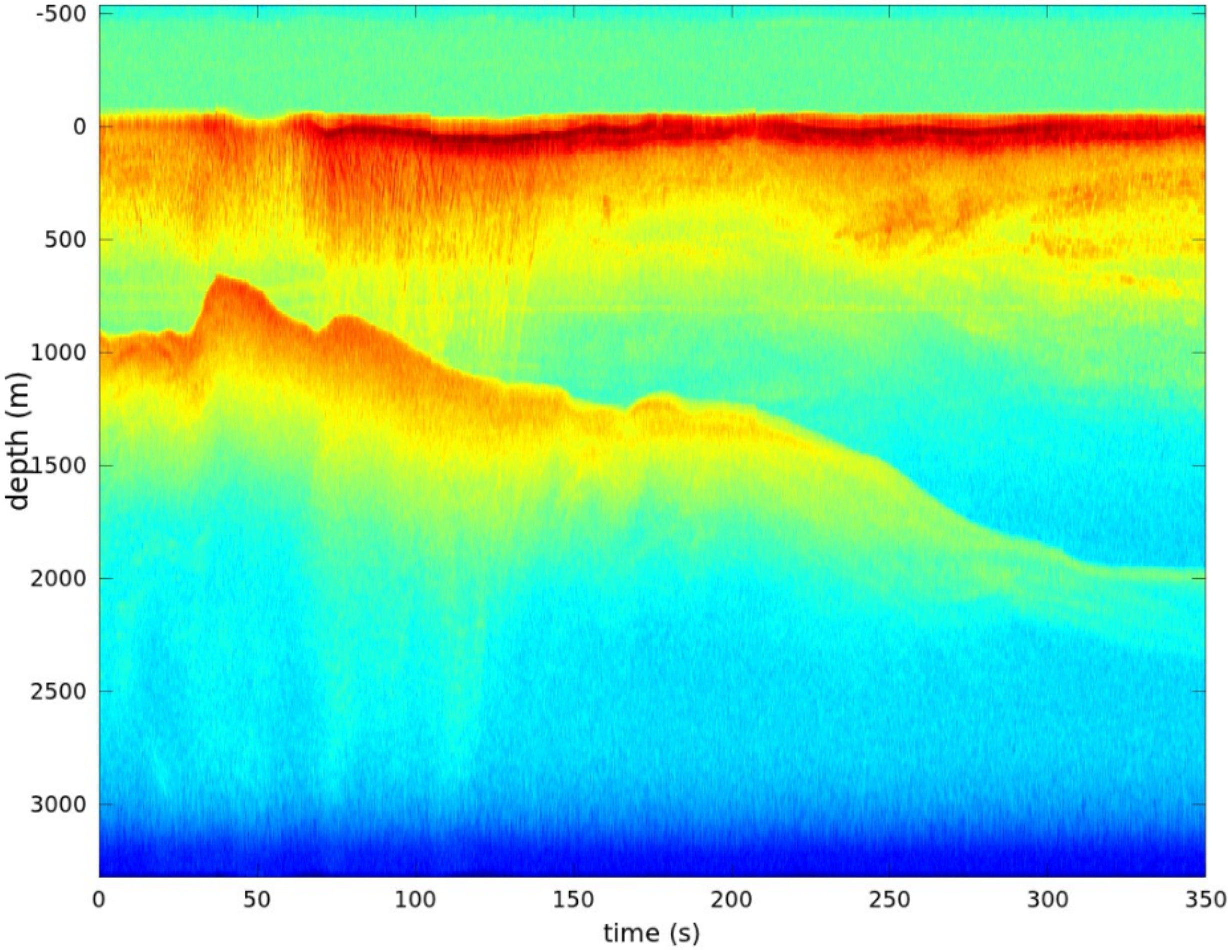

Figure 2.1: An example echogram. The x-axis represents the flight time (corresponds to horizontal displacement). The y-axis is depth within the ice, and the color "axis" is power in arbitrary units, with red corresponding to most received power and blue corresponding to least received power..

2.2 Attenuation and Reflection

Pure, cold ice is a poor conductor and is nearly RF transparent. Antarctic ice can have many impurities that increase the conductivity and thus decrease the attenuation length. Most impurities fit two categories, acids that are a result of volcanic ash deposits and salts that come from proximity to ocean water. MacGregor presents models for how impurity concentrations affect the attenuation of ice in Antarctica [19]. It is common in Glaciology to take field measurements, in this case ionic concentrations from ice cores, and interpolate for whole-continent coverage using the Kriging technique (essentially weighted interpolation). This is not ideal and assumes some slowly-varying concentration levels, but because new measurements are few and the Antarctic ice sheet so voluminous some interpolation must be resorted to for a whole-continent model. Such a model has been developed by Amir Javaid [20], but until now there have not been efforts to verify the general accuracy of this model using RF signals.

The quality of the ice-air interface is important to know for reconstruction of both upward going neutrino-generated RF signals (refracted) and downward moving cosmic ray-induced RF signals (reflected). The surface is prone to both large scale slopes as well as local roughness (mostly due to wind-blown snow). The interface has frequency-dependent effects which can be probed with satellite and airplane backscatter measurements in different frequency bands. Based on the frequency of these signals, the difference between genuine surface effects and sub-surface effects can be estimated. It is desired to develop a model of the surface reflection coefficients of Antarctica, possibly with surface windspeed data as input if it is shown to cause time-dependent effects.

Both the surface roughness and attenuation measurements are also important to other RF-based neutrino detectors, such as those proposed using lunar regolith as well as the moons of Saturn and Jupiter. It has been proposed by the Passive Radio Ice Depth Experiment to measure the depth of the ice of of Enceladus using an orbiter that would work similarly to ANITA (the observed flux implying the volume, in this case).

2.3 CReSIS

The Center for Remote Sensing of Ice Sheets (CReSIS) makes use of synthetic aperture radar mounted on planes to survey many areas of Greenlandic and Antarctic ice over the wavelength regime of 1.8cm-2.5m [21]. Different bands are suited to different purposes, with higher frequency signals intended to measure surface features like recently accumulated snow and the longest wavelength signals useful for penetrating to the bedrock layer to measure the depth of the ice. CReSIS is largely interested in the depth of polar ice and in particular the changing depth near the coasts (for mass balance calculations), predominantly in West Antarctica. The interior flight paths are rarer than the coastal, but there is significant interior coverage where there is overlap with ANITA flight paths. For the basal-reflected measurements, or RDS (Radar Depth Sounding), CReSIS uses a chirped pulse centered at 190 MHz. The pulse is reflected at the air-snow transition and the CReSIS DAQ measures this on a low-gain channel (to avoid saturation). The DAQ then switches to a high-gain channel to search for the basal reflection (that can be more than 4km deep). The time series are stitched together at a common gain value during data processing. Many time series are stacked together to create images called echograms or radargrams. In the publicly available CReSIS data repository one can find some combination of the high-gain channel echogram, the low-gain channel echogram, and/or the combined echogram. These have already been processed to adjust for side-lobe returns (using beam-forming to steer the radar) and only give power time-series, with the phase information not available. Because of the way the gain switching scheme works, one cannot assume that the low-gain channel is at full gain value by the time the snow surface return arrives at the transceiver. Although this makes a depth-averaged attenuation estimate inconsistent (due to different flight altitudes) and is prone to introducing a potentially large error, it can be used to estimate the depth-averaged attenuation length given a few assumptions, as shown in Chapter 4. For the surface-bottom method detailed in Chapter 4 any explicit correction for the possible DAQ gain effect would lead to shorter estimated attenuation length values. The surface-bottom method only uses same-altitude pairs of data, so differing altitude effects, if any, should cancel out. Even though CReSIS samples both polar ice sheets, the Greenland data is sampled at a higher rate and has more complete coverage, so analysis has been concentrated with that data set to develop attenuation estimation techniques before generalizing to Antarctic ice.

2.4 Satellite Experiments

Satellite-borne RF and microwave surface reflection studies have been conducted that have significant coverage of polar ice. The backscattered signal received by these satellites are frequency dependent, both due to surface features (roughness of the snow/ice, wind blown ridges known as sastrugi, liquid water, rock protrusions, local slope) and sub-surface composition. Most of the Antarctic ice sheet has been imaged in 3 radio bands (S-, Ka-, and Ku-bands) by the Envisat and AltiKa satellites [22], as well as in the L-band by Aquarius [23].

2.5 Conductivity of Polar Ice

Along with temperature and density the chemical impurities in ice also influence the dielectric properties. In pure ice absorption comes from Debye relaxation and the LF tail of infrared absorption bands [24]. An empirical equation for the imaginary part of the permittivity is given by

$$\varepsilon'' = \frac{A}{f} + Bf^{C} \tag{2.1}$$

where A, B, and C are empirically determined constants and f is the frequency in GHz. Values for these constants are given in Figure 2.2. The imaginary part of the permittivity is related to the conductivity, σ, by the equation

$$\varepsilon'' = \frac{\sigma}{2\pi f \varepsilon_0}, \tag{2.2}$$

where ε_0 is the permittivity of free space and f is frequency in Hz. The attenuation of the EM radiation is a function of the conductivity and the real part of the permittivity, ε',

$$\alpha(dB/m) \approx 8.686\sqrt{\frac{\mu_0}{\varepsilon_0 \varepsilon'}}\frac{\sigma}{2}. \tag{2.3}$$

The attenuation length (in meters), then, can be expressed as

$$L_\alpha = \frac{20\ \log_{10}(e)}{\alpha}. \tag{2.4}$$

The values of permittivity, conductivity, attenuation, and attenuation length corresponding to the empirical values of ε'' shown in Fig. 2.2 can be found in Table 2.1. The real part of the permittivity

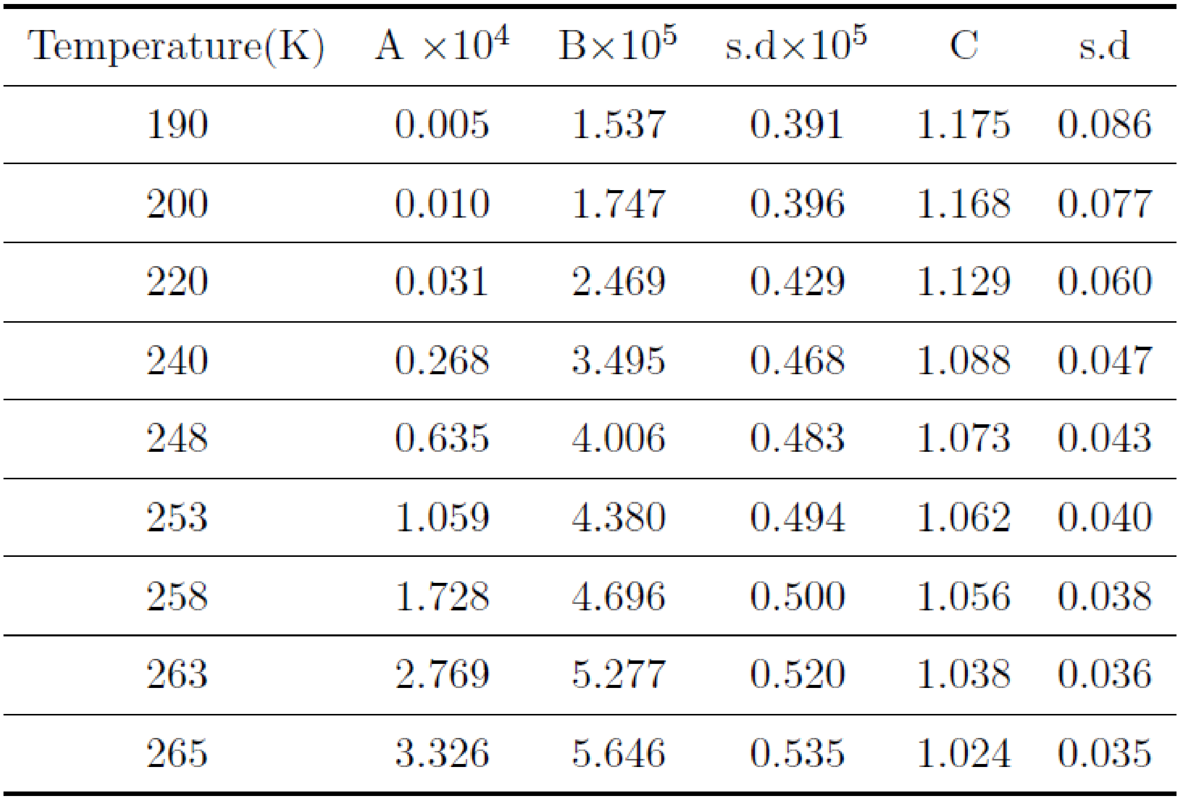

Temperature(K)	A $\times 10^4$	B$\times 10^5$	s.d$\times 10^5$	C	s.d
190	0.005	1.537	0.391	1.175	0.086
200	0.010	1.747	0.396	1.168	0.077
220	0.031	2.469	0.429	1.129	0.060
240	0.268	3.495	0.468	1.088	0.047
248	0.635	4.006	0.483	1.073	0.043
253	1.059	4.380	0.494	1.062	0.040
258	1.728	4.696	0.500	1.056	0.038
263	2.769	5.277	0.520	1.038	0.036
265	3.326	5.646	0.535	1.024	0.035

Figure 2.2: Emprical values for the permittivity of pure ice. The columns with “s.d.” refer to the standard deviation of the preceeding column. Table from [25]

Temperature(K)	$\varepsilon'' \times 10^4$	$\sigma(\mu S/m)$	$\alpha(dB/km)$	$L_\alpha(m)$
190	0.048	0.051	0.047	184000
200	0.078	0.082	0.076	114000
220	0.201	0.213	0.196	44300
240	1.468	1.552	1.429	6080
248	3.410	3.604	3.315	2620
253	5.649	5.971	5.488	1580
258	9.176	9.699	8.908	975
263	14.668	15.504	14.229	610
265	17.608	18.612	17.077	509

Table 2.1: Empirical values of permittivity, conductivity, and attenuation of pure ice at 190 MHz derived from the empirical results presented in [25].

is largely dependent on temperature, with [24] parameterizing it as

$$\varepsilon' = 3.1884 + 9.1 \times 10^{-4} T, \tag{2.5}$$

with T in Kelvin. Conductivity can be increased based on chemistry and crystal structure. Ice can be described as a “protonic semiconductor” [20], the conductivity depends on the polarization of the H_2O molecules and defects in the crystal. Crystal defects can be ionic or Bjerrum. Bjerrum defects are due to rotation of the H_2O molecule such that there is either an extra proton (D defect) or no protons (L defect) in the hydrogen bond, but maintaining the H_2O molecule. Ionic defects are the formation of H_3O^+ and OH^- from proton transfer between water molecules. Jaccard theory suggests that DC (and LF) conductivity is due to minority carriers (ionic defects) and HF conductivity is due to majority carriers (Bjerrum defects) [20]. Other sources of increased conductivity include acids (largely deposited through snow that was influenced by volcanic ash) and sea salt. The overall conductivity can be considered as the sum of these components, $\sigma = \sigma_{pure} + \sigma_{H^+} + \sigma_{ssCl^-}$. Once a high frequency conductivity has been measured it can be scaled to other temperatures via the Arrhenius equation,

$$\sigma_\infty = \sigma_{\infty,258} \exp\left(\frac{E}{R}\left(\frac{1}{T_{258}} - \frac{1}{T}\right)\right), \tag{2.6}$$

where $\sigma_{\infty,258}$ is the measured reference impurity component of the conductivity (at 258 K), E is the activation energy (typical value of 0.22 eV), R is the universal gas constant, T_{258} is 258 K, and T is the desired temperature in Kelvin. As can be seen in Fig. 2.3 the impurities are a dominant affect on the conductivity at lower temperatures.

2.6 Ice Layers

The precise history and cause of internal ice layers are not well-understood, but they can still be described by their effect on radio signals. A given layer of ice, as with bulk ice, has a set of dielectric properties that can be described by the complex relative permittivity, $\varepsilon = \varepsilon' - j\varepsilon''$.

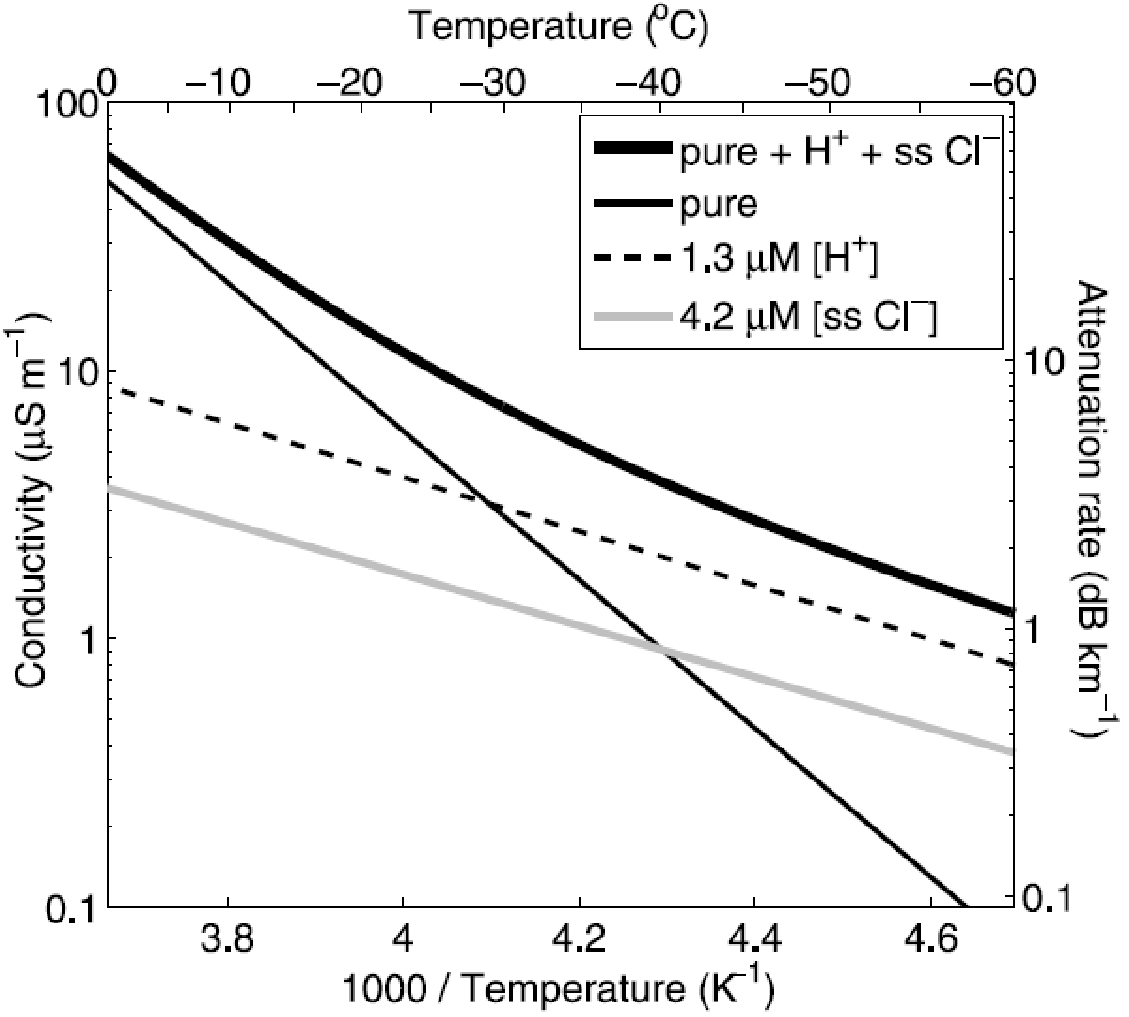

Figure 2.3: Total attenuation in ice from pure and impure components with the acid and salt concentrations measured at Siple Dome. At approximately -30° C and colder the contributions from the impurities dominate. The cross-over temperature would get higher with greater impurity concentrations. Plot from [26].

Behavior of individual layers and groups of layers will first be discussed assuming lossless media so that the changes to the permittivity are only due to changes in the real part, ε' ([27]). The small contrasts between internal layers in the ice have associated reflection coefficients that would be undetectable on their own, but many such layers combined can give stronger reflected signals (with a maximum being the half-space value, that is the reflection coefficient if there was a single transition to an infinite layer). Robin [28] showed small variations in ice density could produce reflected signals detectable at the surface for depths up to 1000m. Harrison [29] proposed that the anisotropy of the permittivity in the parallel and perpendicular directions with respect to the c-axis of the ice would produce "most" of the variation in the observed radar echoes. Paren and Robin [30] assume an intermediate model - changes in density (ε' changes) responsible for reflections to depths 1500m and changes in attenuation (ε'' changes) responsible for deeper reflecting layers. Clough [27] showed that any single layer due to dust, ash, or permittivity anisotropies would be unlikely to be observed, but that zones of layers will act as a single thick layer with averaged properties. We demonstrate this effect below.

2.6.1 Single Thin Layer

Consider a set of three layers that are arranged so that the bottom layer (medium 1) is a half-space, there is a thin middle layer (medium 2), and an upper space (medium 3) as shown in Figure (2.4).

If there is cw plane wave radiation incident at medium 3 the received reflected signal from such a setup would contain the direct reflection from the 3-2 interface; a signal that refracts through the 3-2 interface and is reflected off of the 2-1 interface and again refracted through the 2-3 interface; a signal that refracts through the 3-2 interface, is reflected off of the 2-1 interface, is reflected off of the 2-3 interface, is again reflected off the 2-1 interface and is again refracted through the 2-3 interface. This can continue for an arbitrary number of internal reflections in the middle layer. The first several scenarios are shown in Fig. 2.4 and may be expressed symbolically as:

i. R_{32}

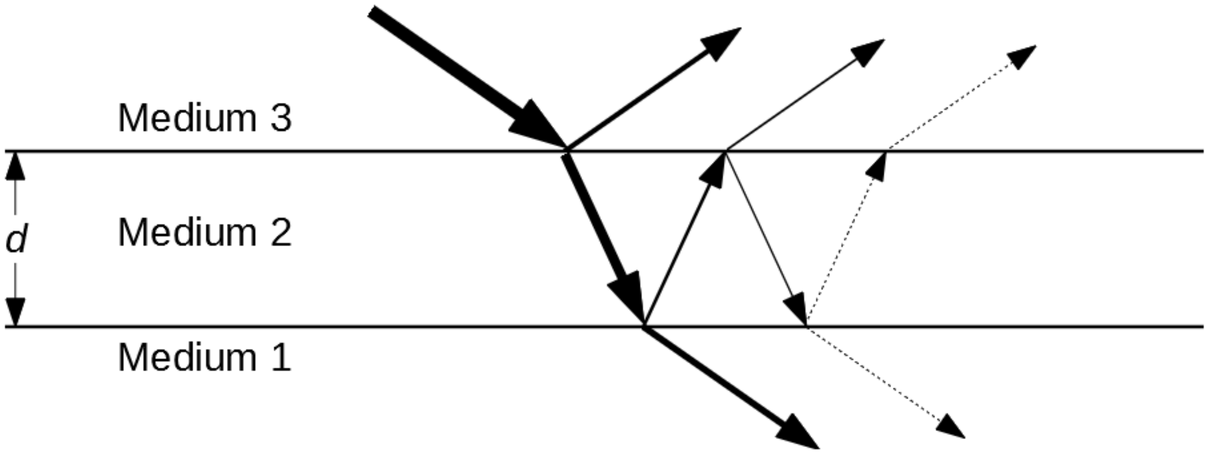

Figure 2.4: Direct and reflected signal paths in three layers.

ii. $T_{32}R_{21}T_{23}\exp(2ik_{2z}d)$

iii. $T_{32}R_{21}R_{32}R_{21}T_{23}\exp(4ik_{2z}d)$

where R_{ij} is the reflection coefficient of the *i-j* boundary, T_{ij} is the transmission coefficient of the *i-j* boundary, and the exponential term represents the accumulation of phase through the 2$^{\text{nd}}$ layer of thickness d and having vertical wavenumber in the second medium k_{2z}. Assuming that the amplitude of the initial wave is unity, then the value for the total reflected wave - and thus the total reflection coefficient [31] - is then given by

$$R = R_{32} + T_{32}R_{21}T_{23}\exp(2ik_{2z}d) + T_{32}R_{21}R_{23}R_{21}T_{23}\exp(4ik_{2z}d) + T_{32}R_{21}R_{23}R_{21}R_{23}R_{21}T_{23}\exp(6ik_{2z}d). \tag{2.7}$$

Expanding this to account for infinite internal reflections in the middle layer the following is obtained

$$R = R_{32} + T_{32}R_{21}T_{23}\exp(2ik_{2z}d)\sum_{n=0}^{\infty}\left[R_{23}R_{21}\exp(2ik_{2z}d)\right]^n, \tag{2.8}$$

which can be simplified using the sum of an infinite geometric series to give

$$R = R_{32} + \frac{T_{32}R_{21}T_{23}\exp(2ik_{2z}d)}{1 - R_{23}R_{21}\exp(2ik_{2z}d)}. \tag{2.9}$$

Using the definitions $R_{ij} = \frac{Z_j - Z_i}{Z_j + Z_i}$ (where Z_i is the impedance of the i$^{\text{th}}$ layer), $R_{ji} = -R_{ij}$, and $T_{ij} = 1 + R_{ij}$ (2.9) can be expressed in the form [31]

$$R = \frac{R_{32} + R_{21}\exp(2ik_{2z}d)}{1 + R_{32}R_{21}\exp(2ik_{2z}d)}. \tag{2.10}$$

The 3 layers can be considered to be a single layer of different ice in an otherwise homogeneous bulk of ice. This would mean layer 1 and 3 have the same properties and that $R_{32} = R_{12}$. Let the second layer be similar so that it has index of refraction $n_2 = n_1 + \Delta n$. The reflection coefficient at boundary *i-j* is equal to $\frac{n_i - n_j}{n_i + n_j}$. Then the reflection coefficient at boundary 1-2 (or boundary 3-2) can be written as

$$R_{12} = \frac{n_1 - n_2}{n_1 + n_2} = \frac{n_1 - (n_1 + \Delta n)}{n_1 + (n_1 + \Delta n)} = \frac{\Delta n}{2n_1 + \Delta n} \approx \frac{\Delta n}{2n_1}. \tag{2.11}$$

The $R_{32}R_{21}$ term in (2.10) is $\mathscr{O}((\Delta n)^2)$ and can be ignored. The term $exp(2ik_{2z}d)$ simplifies to $1 + 2ik_{2z}d$ in the case that $d \ll \lambda$ ($kd \ll 1$), representing relatively thin layers compared to the wavelength of the incident signal, giving $R = -R_{32}(2ik_{2z}d)$. Now (2.9) can be further simplified by substituting $R_{32} = R_{12} \approx \frac{\Delta n}{2n_1}$ to give

$$R = -2ik_{2z}d\frac{\Delta n}{2n_1} = -\frac{2i\pi d}{\lambda}\frac{\Delta n}{n_1}. \tag{2.12}$$

As shown in [27], using the empirical relationship between density (ρ) and index of refraction, $n = 1 + 0.85\rho$, several equivalent expressions of the reflection coefficient in terms of different physical properties can be given as

$$|R| = \frac{\pi d}{\lambda}\left(\frac{2\Delta n}{n}\right) = \frac{\pi d}{\lambda}\left(\frac{\Delta \varepsilon}{\varepsilon}\right) \approx \frac{\pi d}{\lambda}(\Delta \rho). \tag{2.13}$$

2.6.2 Multiple Layers

According to Brekhovskikh [31] a large number of layers can be treated as a single layer having an equivalent impedance. This impedance can be solved for iteratively starting at the bottom layer to determine the reflection coefficient at the top by determining the equivalent impedance at each successive top boundary.

The input impedance at the top of a layer, Z_i^t, is expressed in terms of the input impedance, Z_i^b, at the bottom of the same layer as

$$Z_i^t = \frac{Z_i^b - iZ_1 \tan\phi_1}{Z_1 - Z_i^b \tan\phi_1} \tag{2.14}$$

where $\phi_1 = kd\cos\theta$. A starting value of Z must be set, which is given as the intrinsic impedance of the medium $Z = \sqrt{\frac{\mu_0}{\varepsilon\varepsilon_0}}$ ($\approx 212\Omega$ for ice).

Figure 2.5 shows the results of using this iterative approach to determine the reflection coefficients of many layers evenly spaced at 0.01λ over a total thickness of a wavelength. With a quarter wavelength periodicity the reflection coefficient is, at maximum, equal to the half-space reflection coefficient.

Figures 2.6 and 2.7 show the results if the spacing is no longer uniform but uniformly distributed from $0.1 - 10cm$ and at $3cm \pm 1cm$, respectively, and a wavelength of 4m.

These results demonstrate that randomly spaced thin layers that would not necessarily be evident in radar returns individually can interfere in such a way as to produce larger returns (with a maximum reflection of approximately the half space value). Therefore, in our case as in the analysis in Chapter 4 the observed internal reflections are either the result of an intrinsically highly reflection layer or a constructive interference effect of many less reflective layers of the type described above.

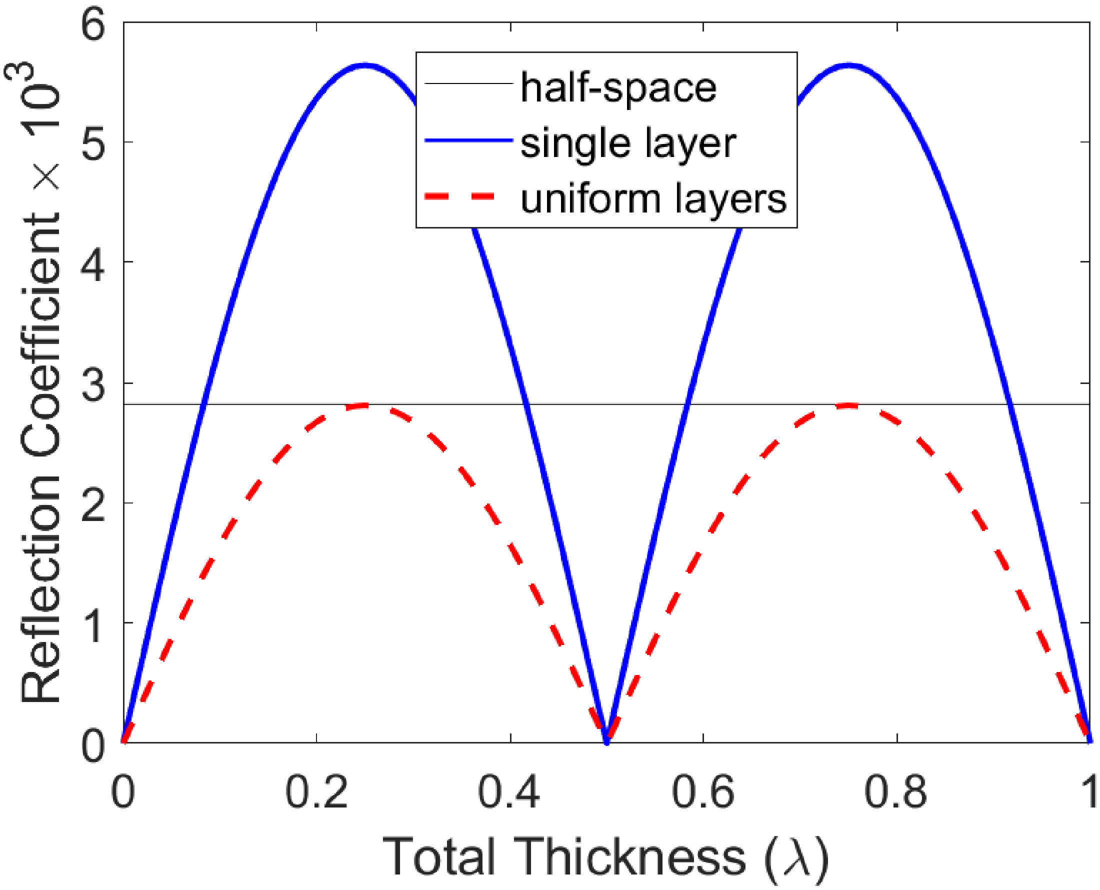

Figure 2.5: Reflection coefficient as a function of depth for a single layer and uniform multiple layers compared to the value from a half-space. Layer thickness and spacing is 0.01λ, Δ n = 0.01. Following from [27].

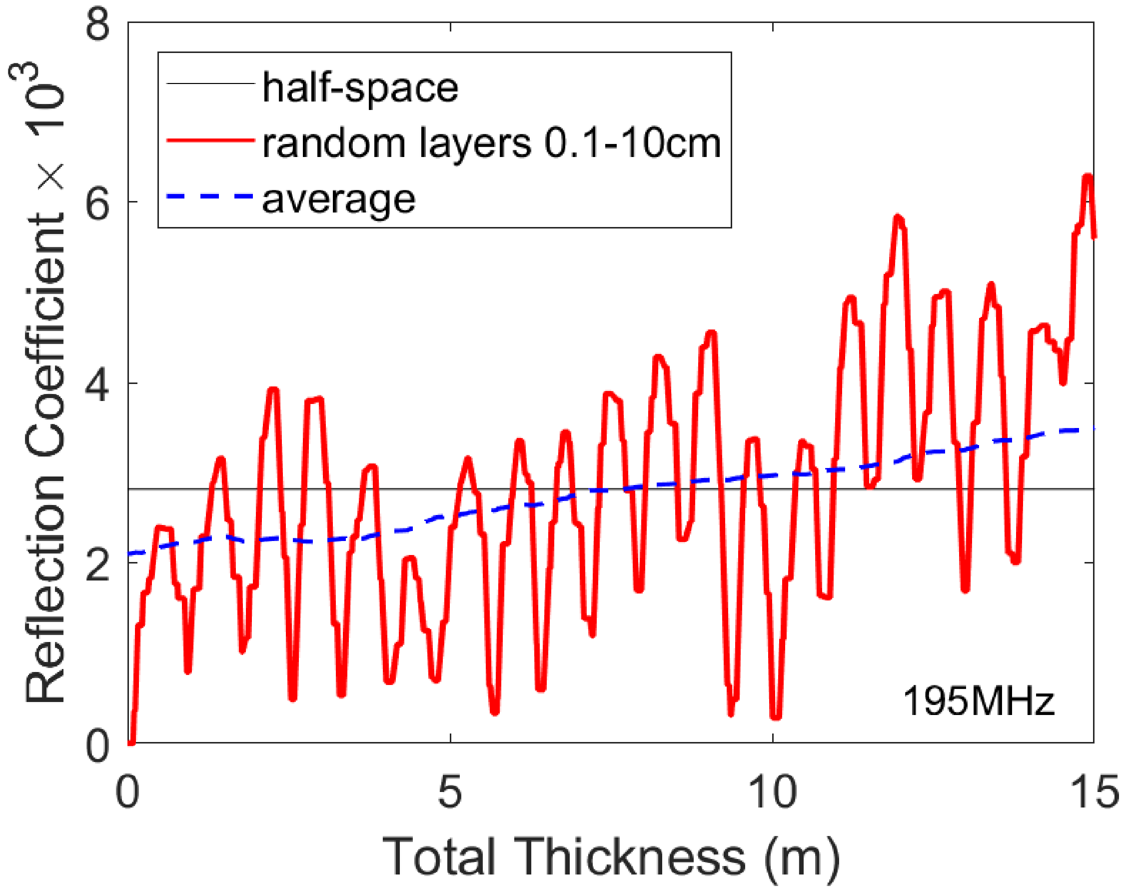

Figure 2.6: Reflection coefficient as a function of depth for many random layers. Layer thickness and spacing is randomly distributed between 0.1 and 10cm. λ=4m, Δ n = 0.01. Following from [27].

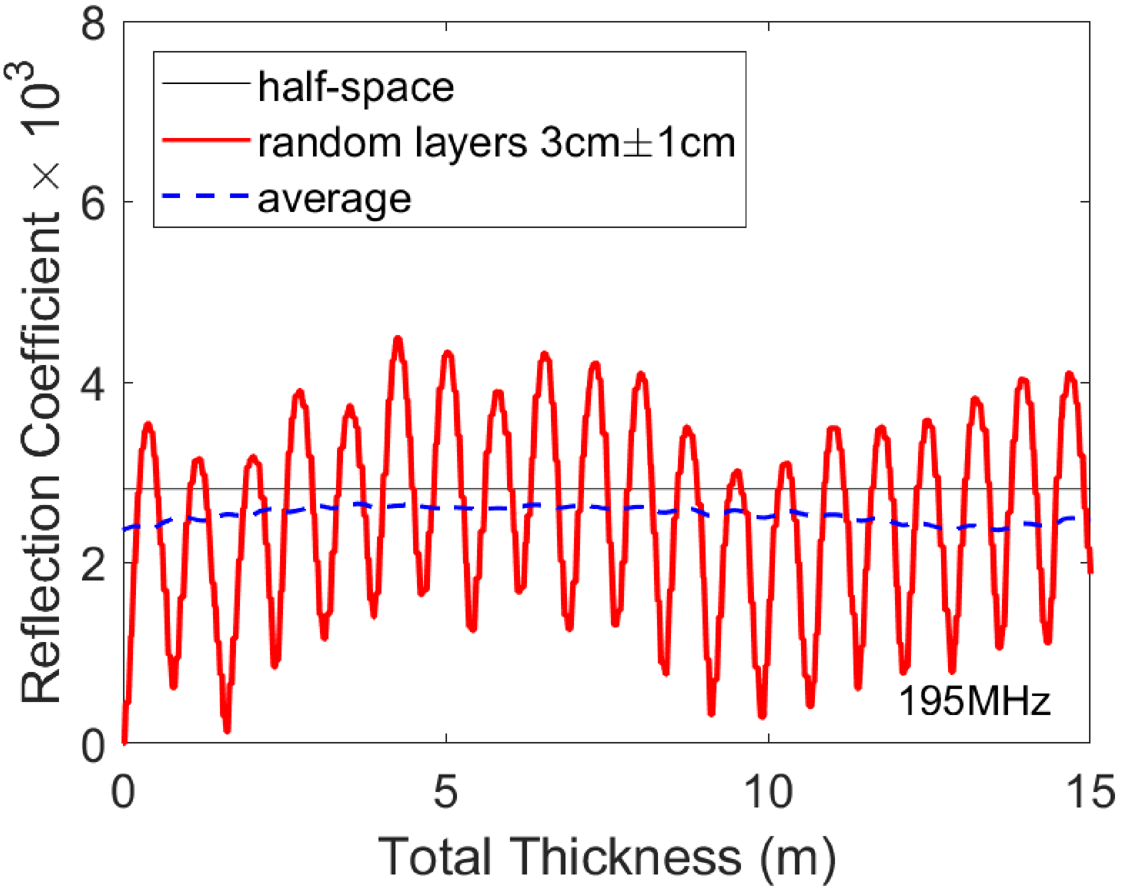

Figure 2.7: Reflection coefficient as a function of depth for many random layers. Layer thickness and spacing is random with a distribution of $3 \pm 1cm$. λ=4m, Δ n = 0.01. Following from [27].

Chapter 3

Surface Reflection

3.1 Introduction

The surface conditions offer another effect on polar radio detection that is challenging to measure and to model. For ANITA specifically, the surface roughness (inasmuch as it manifests itself as a correction to the reflection coefficient) plays a vital role in determining the primary particle energy for cosmic ray events. The location-dependent reflection coefficient is also important for reconstruction of neutrino-produced radio signals as it determines the transmission properties of these signals through the ice-air boundary. For the attenuation analysis in Chapter 4 that relies on comparison of ice surface and bedrock oberved radar reflections it is necessary that there is some minimum level of smoothness to the surface reflection coefficient lest the return signals totally de-cohere.

3.2 HiCal

The High-Altitude Calibration (HiCal) pulser was a balloon flight flown in concert with ANITA-3. Using a piezo-electric device as the signal generator, a broadband signal was transmitted from a horizontally aligned dipole antenna at an altitude of 38km, approximately the same altitude as ANITA-3. Provided that the signal strength was high enough above background levels after

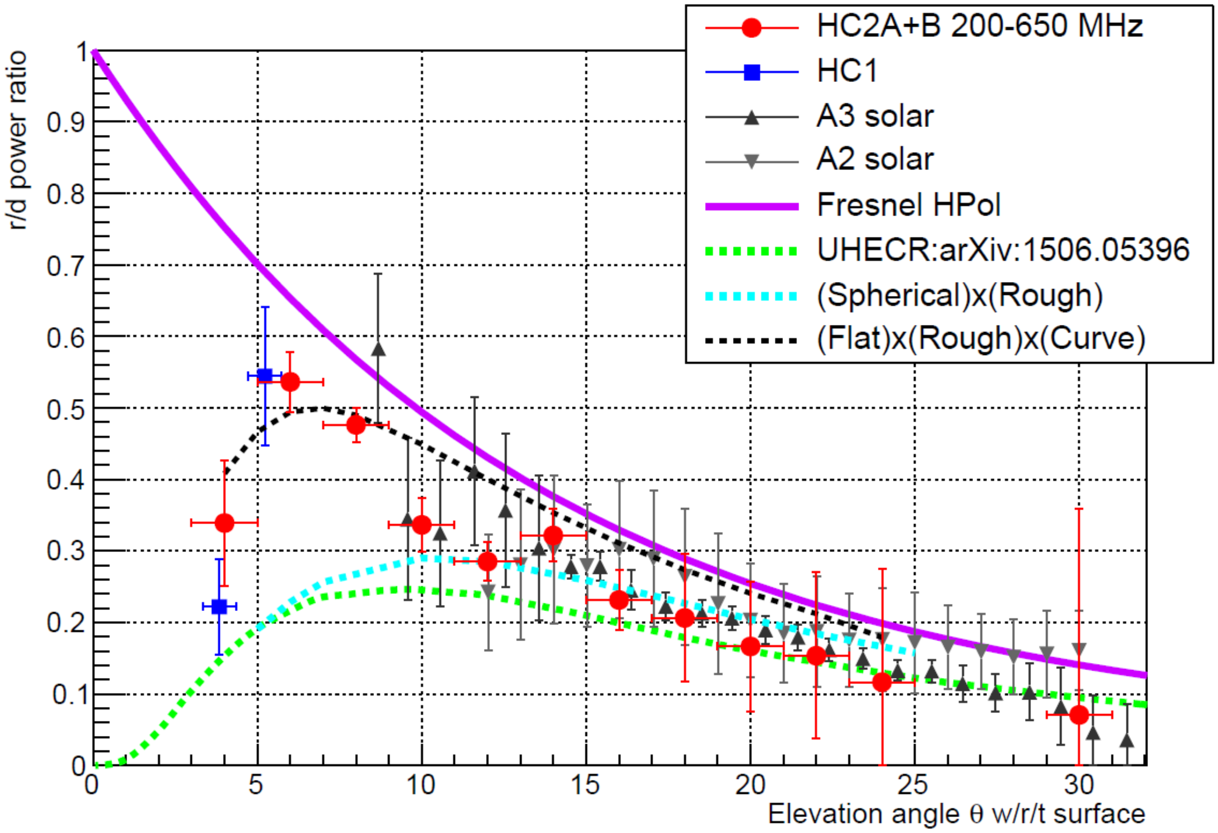

Figure 3.1: Results plot comparing measurements of HiCal1 and HiCal2 as well as the measured reflection coefficients of solar signals by ANITA 2 and 3 as well as the expected theoretical curves (based on Fresnel equations with and without surface effects). Figure from [33].

traveling the inter-balloon distance of up to 800km, ANITA-3 should have h-pol triggers on both the direct path signal from HiCal as well as the surface reflected signal. Comparing the ratios of these signals and accounting for the different path lengths should give the reflection coefficient (even as a function of frequency). Due to the differing inter-balloon spacing, some sampling of the angle-dependence of the reflection coefficients should also be possible. Results of the HiCal analysis can be found in [32].

HiCal-2 was flown in accompaniment with the ANITA-4 flight. Some design improvements were made but the general method was the same [33]. The calculated reflection coefficients from the HiCal-1 and HiCal-2 measurements with comparison to solar-signal-derived and theoretical (Fresnel) values are shown in Fig. 3.1.

3.3 Satellite Experiments

The Envisat and AltiKa satellite experiments use high-frequency RF signals to measure reflected power across Antarctica. Envisat hosts both S- and Ku-band channels, corresponding to bands of 2-4 GHz and 12-16 GHz, respectively. AltiKa is a radar altimeter that measures the backscatter in the Ka-band, 26.5-40 GHz. The reflected power between the S-, Ka-, and Ku-bands are correlated with each other. Using wind data from stations located throughout Antarctica, negative correlation can be shown between windspeed and backscatter strength in all three bands (Fig. 3.2). By scrambling which backscattered value gets paired with which wind station, this correlation is broken (Fig. 3.3). This is the first step toward developing a model of location and frequency dependent reflection/transmission properties. The developed model would also need some method of extrapolating to the frequency band that ANITA is sensitive to.

3.4 Reflectivity as a Function of Time

A more natural band to compare with the band ANITA is sensitive to (200-1200MHz) is the L-band (1-2GHz) (Normalized Radar Cross-Section [NRCS] for H-pol–to–H-pol shown in Fig. 3.4). The Aquarius satellite experiment [23] took scatterometer data at 1.26GHz for approximately 4 years and published weekly average data of the NRCS in 6 different spatial configurations and 3 different polarity modes. The satellite took data both on ascending and descending orbit and at three different incident angles, $29.36°, 38.49°$, and $46.29°$. All of the figures in this work come from Beam 1 ($29.36°$) unless otherwise noted. The measurements for each of these configurations are in V-pol transmit and receive, H-pol in transmit and receive, and cross-pol (assumed to be independent of order). The values are gridded into 36km x 36km squares. Normalized radar cross section is defined as $\sigma^0 = \left\langle \frac{\sigma_i}{A_i} \right\rangle$ where σ_i is an objects' radar cross section and A_i is the ground area over which the cross-section for that object is being averaged. The radar cross section itself, σ, depends on many factors, including reflectivity, orientation, material, angles of incidence and reflection, and size. It can be thought of as a comparison to the returned signal from a perfectly

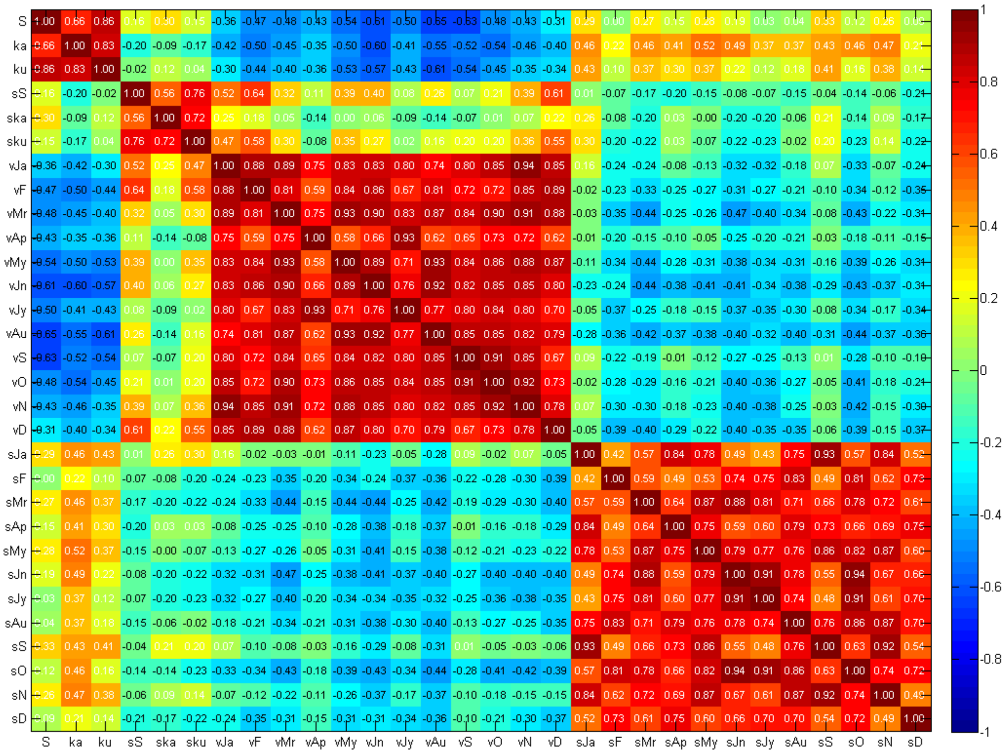

	S	ka	ku	sS	ska	sku	vJa	vF	vMr	vAp	vMy	vJn	vJy	vAu	vS	vO	vN	vD	sJa	sF	sMr	sAp	sMy	sJn	sJy	sAu	sS	sO	sN	sD
S	1.00	0.66	0.86	0.16	0.30	0.15	-0.36	-0.47	-0.48	-0.43	-0.54	-0.61	-0.50	-0.65	-0.63	-0.48	-0.43	-0.31	0.29	0.00	0.27	0.15	0.28	0.19	0.03	0.04	0.33	0.12	0.26	0.09
ka	0.66	1.00	0.83	-0.20	-0.09	-0.17	-0.42	-0.50	-0.45	-0.35	-0.50	-0.60	-0.41	-0.55	-0.52	-0.54	-0.46	-0.40	0.46	0.22	0.46	0.41	0.52	0.49	0.37	0.37	0.43	0.46	0.47	0.21
ku	0.86	0.83	1.00	-0.02	0.12	0.04	-0.30	-0.44	-0.40	-0.36	-0.53	-0.57	-0.43	-0.61	-0.54	-0.45	-0.35	-0.34	0.43	0.10	0.37	0.30	0.37	0.22	0.12	0.18	0.41	0.16	0.38	0.14
sS	0.16	-0.20	-0.02	1.00	0.56	0.76	0.52	0.64	0.32	0.11	0.39	0.40	0.08	0.26	0.07	0.21	0.39	0.61	0.01	-0.07	-0.17	-0.20	-0.15	-0.08	-0.07	-0.15	-0.04	-0.14	-0.06	-0.21
ska	0.30	-0.09	0.12	0.56	1.00	0.72	0.25	0.18	0.05	-0.14	0.00	0.06	-0.09	-0.14	-0.07	0.01	0.07	0.22	0.26	-0.08	-0.20	0.03	-0.00	-0.20	-0.20	-0.06	0.21	-0.14	0.09	-0.17
sku	0.15	-0.17	0.04	0.76	0.72	1.00	0.47	0.58	0.30	-0.08	0.35	0.27	0.02	0.16	0.20	0.20	0.36	0.55	0.30	-0.20	-0.22	0.03	-0.07	-0.22	-0.23	-0.02	0.20	-0.23	0.14	-0.22
vJa	-0.36	-0.42	-0.30	0.52	0.25	0.47	1.00	0.88	0.89	0.75	0.83	0.83	0.80	0.74	0.80	0.85	0.94	0.85	0.16	-0.24	-0.24	-0.08	-0.13	-0.32	-0.32	-0.18	0.07	-0.33	-0.07	-0.24
vF	-0.47	-0.50	-0.44	0.64	0.18	0.58	0.88	1.00	0.81	0.59	0.84	0.86	0.67	0.81	0.72	0.72	0.85	0.89	-0.02	-0.23	-0.33	-0.25	-0.27	-0.31	-0.27	-0.21	-0.10	-0.34	-0.12	-0.35
vMr	-0.48	-0.45	-0.40	0.32	0.05	0.30	0.89	0.81	1.00	0.75	0.93	0.90	0.83	0.87	0.84	0.90	0.91	0.88	-0.03	-0.35	-0.44	-0.25	-0.26	-0.47	-0.40	-0.34	-0.08	-0.43	-0.22	-0.31
vAp	-0.43	-0.35	-0.36	0.11	-0.14	-0.08	0.75	0.59	0.75	1.00	0.58	0.66	0.93	0.62	0.65	0.73	0.72	0.62	-0.01	-0.20	-0.15	-0.10	-0.05	-0.25	-0.20	-0.21	-0.03	-0.18	-0.11	-0.15
vMy	-0.54	-0.50	-0.53	0.39	0.00	0.35	0.83	0.84	0.93	0.58	1.00	0.89	0.71	0.93	0.84	0.86	0.88	0.87	-0.11	-0.34	-0.44	-0.28	-0.31	-0.38	-0.34	-0.31	-0.16	-0.39	-0.26	-0.31
vJn	-0.61	-0.60	-0.57	0.40	0.06	0.27	0.83	0.86	0.90	0.66	0.89	1.00	0.76	0.92	0.82	0.85	0.85	0.80	-0.23	-0.24	-0.44	-0.38	-0.41	-0.41	-0.34	-0.38	-0.29	-0.43	-0.37	-0.31
vJy	-0.50	-0.41	-0.43	0.08	-0.09	0.02	0.80	0.67	0.83	0.93	0.71	0.76	1.00	0.77	0.80	0.84	0.80	0.70	-0.05	-0.37	-0.25	-0.18	-0.15	-0.37	-0.35	-0.30	-0.08	-0.34	-0.17	-0.34
vAu	-0.65	-0.55	-0.61	0.26	-0.14	0.16	0.74	0.81	0.87	0.62	0.93	0.92	0.77	1.00	0.85	0.85	0.82	0.79	-0.28	-0.36	-0.42	-0.37	-0.38	-0.40	-0.32	-0.40	-0.31	-0.44	-0.37	-0.36
vS	-0.63	-0.52	-0.54	0.07	-0.07	0.20	0.80	0.72	0.84	0.65	0.84	0.82	0.80	0.85	1.00	0.91	0.85	0.67	0.09	-0.22	-0.19	-0.01	-0.12	-0.27	-0.25	-0.13	0.01	-0.28	-0.10	-0.10
vO	-0.48	-0.54	-0.45	0.21	0.01	0.20	0.85	0.72	0.90	0.73	0.86	0.85	0.84	0.85	0.91	1.00	0.92	0.73	-0.02	-0.28	-0.29	-0.16	-0.21	-0.40	-0.36	-0.27	-0.05	-0.41	-0.18	-0.21
vN	-0.43	-0.46	-0.35	0.39	0.07	0.36	0.94	0.85	0.91	0.72	0.88	0.85	0.80	0.82	0.85	0.92	1.00	0.78	0.07	-0.30	-0.30	-0.18	-0.23	-0.40	-0.38	-0.25	-0.03	-0.42	-0.15	-0.30
vD	-0.31	-0.40	-0.34	0.61	0.22	0.55	0.85	0.89	0.88	0.62	0.87	0.80	0.70	0.79	0.67	0.73	0.78	1.00	-0.05	-0.39	-0.40	-0.29	-0.22	-0.40	-0.35	-0.35	-0.06	-0.39	-0.15	-0.37
sJa	0.29	0.46	0.43	0.01	0.26	0.30	0.16	-0.02	-0.03	-0.01	-0.11	-0.23	-0.05	-0.28	0.09	-0.02	0.07	-0.05	1.00	0.42	0.57	0.84	0.78	0.49	0.43	0.75	0.93	0.57	0.84	0.52
sF	0.00	0.22	0.10	-0.07	-0.08	-0.20	-0.24	-0.23	-0.35	-0.20	-0.34	-0.24	-0.37	-0.36	-0.22	-0.28	-0.30	-0.39	0.42	1.00	0.59	0.49	0.53	0.74	0.75	0.83	0.49	0.81	0.62	0.73
sMr	0.27	0.46	0.37	-0.17	-0.20	-0.22	-0.24	-0.33	-0.44	-0.15	-0.44	-0.44	-0.25	-0.42	-0.19	-0.29	-0.30	-0.40	0.57	0.59	1.00	0.64	0.87	0.88	0.81	0.71	0.66	0.78	0.72	0.61
sAp	0.15	0.41	0.30	-0.20	0.03	0.03	-0.08	-0.25	-0.25	-0.10	-0.28	-0.38	-0.18	-0.37	-0.01	-0.16	-0.18	-0.29	0.84	0.49	0.64	1.00	0.75	0.59	0.60	0.79	0.73	0.66	0.69	0.75
sMy	0.28	0.52	0.37	-0.15	-0.00	-0.07	-0.13	-0.27	-0.26	-0.05	-0.31	-0.41	-0.15	-0.38	-0.12	-0.21	-0.23	-0.22	0.78	0.53	0.87	0.75	1.00	0.79	0.77	0.76	0.86	0.82	0.87	0.60
sJn	0.19	0.49	0.22	-0.08	-0.20	-0.22	-0.32	-0.31	-0.47	-0.25	-0.38	-0.41	-0.37	-0.40	-0.27	-0.40	-0.40	-0.40	0.49	0.74	0.88	0.59	0.79	1.00	0.91	0.78	0.55	0.94	0.67	0.66
sJy	0.03	0.37	0.12	-0.07	-0.20	-0.23	-0.32	-0.27	-0.40	-0.20	-0.34	-0.34	-0.35	-0.32	-0.25	-0.36	-0.38	-0.35	0.43	0.75	0.81	0.60	0.77	0.91	1.00	0.74	0.48	0.91	0.61	0.70
sAu	0.04	0.37	0.18	-0.15	-0.06	-0.02	-0.18	-0.21	-0.34	-0.21	-0.31	-0.38	-0.30	-0.40	-0.13	-0.27	-0.25	-0.35	0.75	0.83	0.71	0.79	0.76	0.78	0.74	1.00	0.76	0.86	0.87	0.70
sS	0.33	0.43	0.41	-0.04	0.21	0.20	0.07	-0.10	-0.08	-0.03	-0.16	-0.29	-0.08	-0.31	0.01	-0.05	-0.03	-0.06	0.93	0.49	0.66	0.73	0.86	0.55	0.48	0.76	1.00	0.63	0.92	0.54
sO	0.12	0.46	0.16	-0.14	-0.14	-0.23	-0.33	-0.34	-0.43	-0.18	-0.39	-0.43	-0.34	-0.44	-0.28	-0.41	-0.42	-0.39	0.57	0.81	0.78	0.66	0.82	0.94	0.91	0.86	0.63	1.00	0.74	0.72
sN	0.26	0.47	0.38	-0.06	0.09	0.14	-0.07	-0.12	-0.22	-0.11	-0.26	-0.37	-0.17	-0.37	-0.10	-0.18	-0.15	-0.15	0.84	0.62	0.72	0.69	0.87	0.67	0.61	0.87	0.92	0.74	1.00	0.49
sD	0.09	0.21	0.14	-0.21	-0.17	-0.22	-0.24	-0.35	-0.31	-0.15	-0.31	-0.31	-0.34	-0.36	-0.10	-0.21	-0.30	-0.37	0.52	0.73	0.61	0.75	0.60	0.66	0.70	0.70	0.54	0.72	0.49	1.00

Figure 3.2: Correlation matrix for monthly windspeed data and surface reflections at same locations. The first 3 columns/rows are correlations with S-, ka-, and ku-band backscatter measurements averaged within 5km of a windstation. The next 3 columns/rows are correlations with the standard deviations of S-, ka-, and ku-band backscatter measurements within 5km of a windstation. The next 12 columns/rows are correlations with average monthly windspeeds. The last 12 columns/rows are correlations with the monthly standard deviations of windspeeds. There is a meaningful negative correlation between the mean backscatter around windstations and the average monthly windspeed for all 3 radio bands.

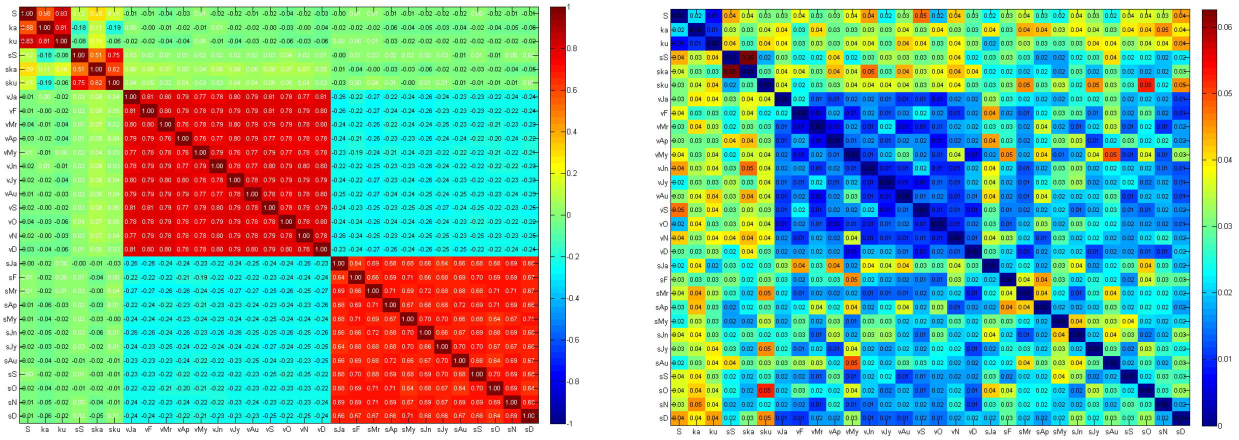

Figure 3.3: Left side: same respective columns/rows as in Fig. 3.2, but the backscatter measurements no longer come from within 5km of a windstation but instead are from a random 5km radius area in Antarctica. Right side: The standard deviation of the correlation matrix values when the location shuffling correlation is repeated 100 times. The areas of correlation coefficient near zero on the left side show that by shuffling the location of the backscatter measurement the negative correlation of windspeed and backscatter amplitude is broken. Note the different scales.

reflecting sphere of cross section $1m^2$. This can be expressed mathematically by the radar equation $P_r = \frac{P_t G_T}{4\pi r^2}\sigma\frac{1}{4\pi r^2}A_{eff}$, where P_r is the received power, P_t is the transmitted power, G_T is the system gain, A_{eff} is the effective area of the receiving antenna, and r is the distance from radar to target. It is seen in the form of this equation that σ represents the area at the target that reflects the incident radiation isotropically. It is non-trivial to back the reflectivity alone out of the NRCS, but if a complete reflection model of Antarctica is developed it should give rise to modeled NRCS values that could be directly compared to the Aquarius data.

It is important to know if wind conditions are drivers of surface roughness (and therefore reflectivity) to determine if ANITA must consider time-dependent effects on the surface reflection properties when calculating for corrections to cosmic ray events. In Section 3.3 we demonstrated a correlation between average surface wind velocities and average radar backscatter in 3-bands. In Figure 3.5 we show that the standard deviation among the weekly average NRCS values in the H-pol transmit-receive configuration are low (typically under 1dB) except from data over the ice shelves (Ross and Ronne). This suggests that average windspeed in an area may, in part, determine its surface roughness, but on the timescales of years there is little change in that roughness over

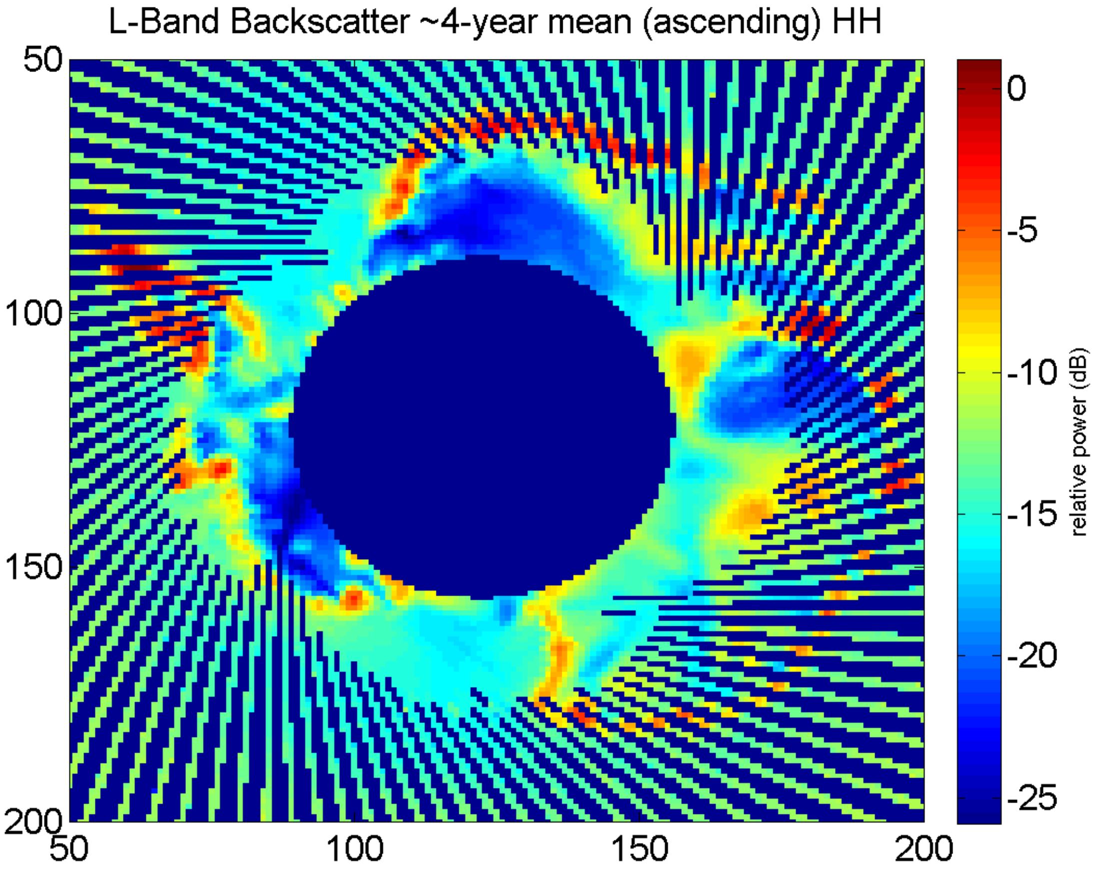

Figure 3.4: The $\sim$ 4 year weekly mean values of NRCS in the H-pol transmit, H-pol receive configuration on ascending orbit. The x- and y-axis values are 36km grid numbers.

much of the ice sheet. Appendix A contains the measurements of the other configurations.

3.5 Correlation Length

Another metric of interest to ANITA or those trying to model the reflectivity of the AIS is a correlation length of the roughness/reflectivity values. This is manifested in a couple of ways. Firstly, what kind of spatial resolution is needed of high-accuracy reflection measurements to be confident that they can reliably be interpolated to other locations, and secondly, to estimate the uncertainty in reflection values due to variance in proximal values. Figure 3.6 shows how far away the nearest grid point with a greater than 3dB difference is from each grid point. There is some unavoidable

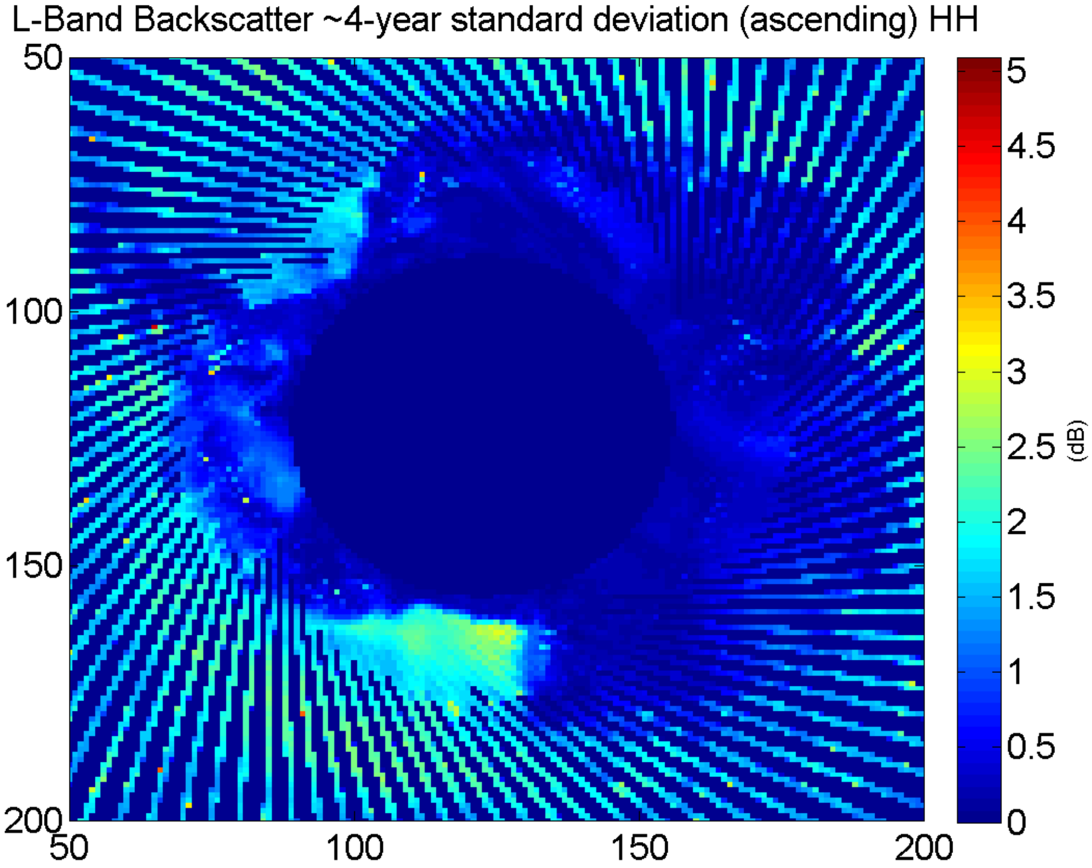

Figure 3.5: The ~ 4 year weekly standard deviation values of NRCS in the H-pol transmit, H-pol receive configuration on ascending orbit. The x- and y-axis values are 36km grid numbers. Areas outside of the Ross and Ronne Ice Shelves exhibit steadiness on the years-long timescale.

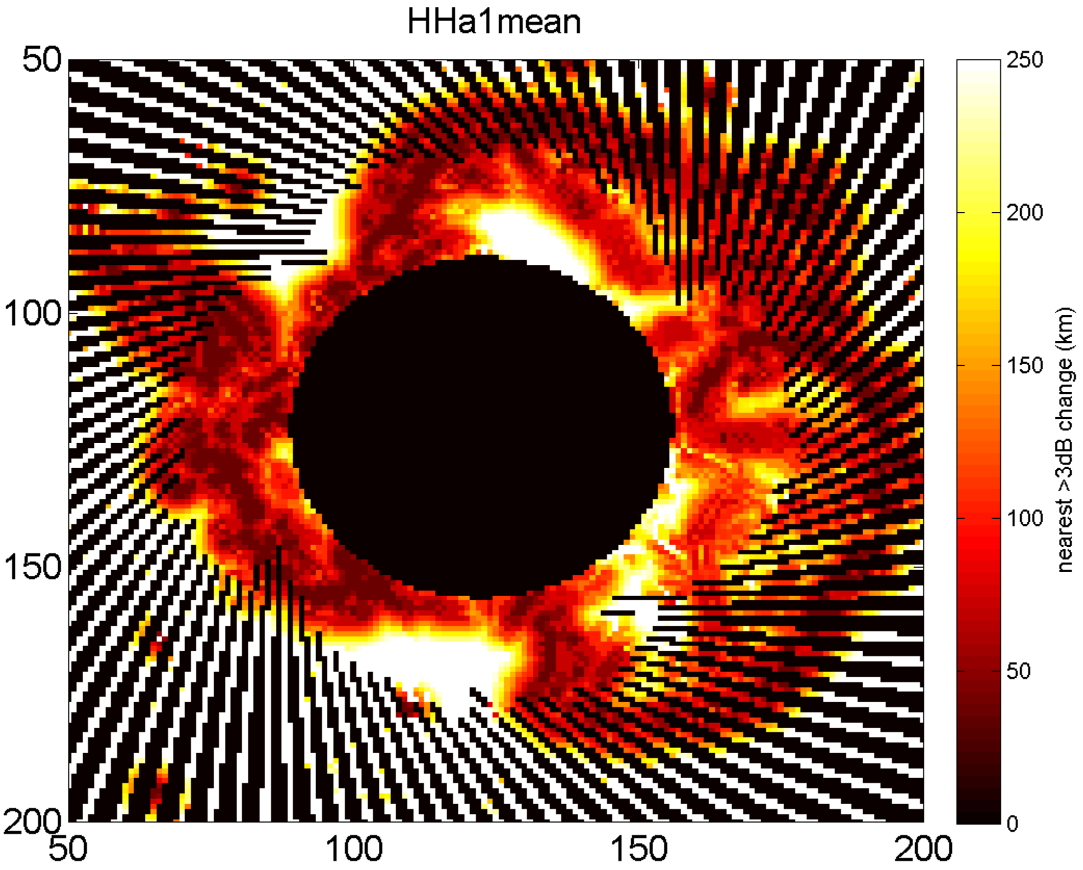

Figure 3.6: Correlation length where the values at each grid point are the number of kilometers away the nearest grid point with a 3dB NRCS value exists. The x- and y-axis values are 36km grid numbers. The data used come from the $\sim$ 4 year mean of H-pol–to–H-pol, ascending orbit, beam 1.

bias to this calculation near the blind spot at high latitudes. There is some stability to the variation over the Ross Sea, in East Antarctica, and in the Queen Maud Land area (grid north). However, the low values near the transantarctic mountains and in West Antarctica suggest needing a fine grid of high accuracy measurements in that area.

Chapter 4

Attenuation Length

In this section two methods of estimating attenuation length are presented. These are previously published in part in [34]. Both methods make use of 150–195 MHz plane-based radar depth sounding (RDS) data accumulated by the Center for Remote Sensing of Ice Sheets group, based at the University of Kansas (KU). In the context of astroparticle physics experiments aimed at understanding radio emissions from cosmic rays and neutrinos interacting in the Earth's polar regions, the methods are meant to directly extract the depth dependence of the radio frequency field attenuation length as well as map out the attenuation over a large area. This is vital for estimating the effective detector volume that Antarctica represents. In the event that a neutrino-produced signal is observed, the estimate for the primary energy is also dependent on tracing the radio signal to its origin while including the effects of attenuation due to travel through the ice. Through analysis of the RDS radar returns the depth-dependence of the field attenuation length can be extracted, which is related to the imaginary part of the permittivity (ε'') by the relationship ($L_\alpha \sim \sqrt{\varepsilon''}$). For ease of comparison to other measurements (based both on ice chemistry and radar interrogation) this method is demonstrated by estimating the depth-averaged radio frequency attenuation length from data taken near the GRIP site located at Summit, Greenland. The value obtained, $< L_\alpha >= 500^{+90}_{-60}$ meters, is based on calculated values in the 1000–2000 meter ice depth interval to which the method can be applied and extrapolated to the full depth, where the errors shown reflect the uncertainty in the extrapolation. It is widely assumed that the attenuation length should decrease with increasing depth/temperature, which is borne out by this method. A depth-averaged attenuation length is also extracted directly from the relative strengths of the observed bedrock vs. surface returns over large regions of both Greenland and Antarctica over the majority of CReSIS flight paths from 2010-2014. Assumptions about systematic effects are made in order to estimate attenuation in this manner, these will be detailed in Section 4.6.2.

4.1 Introduction

To date, much of the information about the interior of the polar ice sheets has been derived from extensive compilations of radar survey data such as those of BEDMAP [35] and CReSIS [36], in which a radar transmitter "shoots" a pulse of radio-frequency signal to the ice surface from an altitude of order 1 km and records the returned signal from the ice layers and bedrock below. These data have been used to map out ice sheet internal layers and bedrock topography [37], which can then inform models of ice flow [38, 39] and mass balance. Some of the information inferred from these returns, along with data collected by examining ice cores, has been very successful in recreating the historical timeline of the ice sheets. For example, the depth and characteristics of certain returns have shown consistency with acid layers deposited following volcanic eruptions and can therefore provide information on the Earth's geological past [40]. Ideally the internal structure of the ice sheets could be studied with a large number of full-depth ice cores, which can provide direct ice chemistry data, but the harsh conditions, expense, and lack of specialized equipment make this unrealistic. Similarly, it is not practical to make an ice sheet in a lab on the scale that would be required to be analogous to the ice studied at the poles. In addition to the ice core recently extracted at South Pole, multi-km Antarctic core data taken from Law Dome (1200 m), Vostok (3623 m), Siple Dome (1003 m), Dome C (3270 m), Dome Fuji (3035 m), Wais Divide (3435 m), and Byrd Station (2164 m) are all available for analysis from the National Ice Core Lab (NICL; www.icecores.org), with the Byrd Station core being the only full-depth sample.

The nature and characteristics of the observed radar returns are directly related to the complex dielectric permittivity $\varepsilon = \varepsilon' - j\varepsilon''$. In general, the "loss tangent", defined as the ratio of the imaginary to the real components of the permittivity ($\tan\delta = \varepsilon''/\varepsilon'$), related to the attenuation coefficient α (dB/km) by $\alpha = 8.686(2\pi f/c_0)\sqrt{\varepsilon'}\tan\delta$ (with f frequency, and c_0 the vacuum velocity of light) and the field attenuation length $L_\alpha = 1/\log\left(10^{\alpha/20}\right)$), of both the firn and the deeper ice are not well-known in the transition region from Ultra-High Frequency (UHF) to microwave, since it is the overlap of the Debye resonance at kHz frequencies and the infra-red peak that defines the minimum loss tangent at $\sim$ 300 GHz [41].

The radio regime of hundreds of MHz, where the ice response is relatively flat, is therefore an ideal frequency region to probe a variety of physical mechanisms and improve the precision of the extrapolation from kHz→GHz.

4.2 CReSIS Hardware

The CReSIS hardware used to take the data on which these analyses are based is described in detail elsewhere ([42, 43], e.g.). That hardware has undergone continuous evolution over the last two decades. The data samples used for our analysis are primarily based on the MCRDS and MCoRDS hardware; specifications for the instrumentation used in their 2009 Antarctica data collection are presented in Table 4.1. Greenlandic data collection employs very similar hardware, sometimes with small changes in operation configuration, power transmission, and center frequency used. Measurements of the imaginary (attenuating) component of the permittivity are based on CReSIS data collected from 2010–2014.

4.3 CReSIS Data Set

The large sample of CReSIS data is used to probe radio frequency attenuation. CReSIS data were collected with an array of above-surface transmitter antennas, hanging beneath a Twin Otter, P3, or DC8 aircraft, and operating at center frequencies from 150 MHz – 195 MHz; linear 'tone'

Table 4.1: CReSIS Multi-Channel Coherent Radar Depth Sounder (MCoRDS; using Monostatic Rx/Tx)

Bandwidth	180-210 MHz
Tx power	550 W
Waveform	Eight channel chirp generation
Acquisition	Eight channels, 14 bit ADC
Rx Aperture	1.5 wavelength aperture
Tx Aperture	1.5 wavelength aperture; fully programmable
Data rate	30 MB/sec total

durations were typically 3–10μs, at ~kHz repetition rates. The transmitted signals are a chirp of approximately 5% bandwidth, this is to help subtract unwanted sidebands from the signal [21]. Before 2014, received signals are read out through two channels, a low-gain channel with tunable amplification matched to the approximate amplitude of the bright initial ice surface reflection, and a high-gain channel with higher amplification matched to the much weaker bedrock reflection [44]. Post-processing matches the gains of the two systems at a common intermediate point so that a single, constant-gain data product can be further analyzed.

All returns within an approximately ten degree vertical beamwidth are coherently summed via standard "synthetic aperture" (SAR) techniques, accounting for transit time delays as a function of depth and lateral displacement from the beam center, into a single "echogram", allowing an estimated range accuracy of approximately 4.2 m (~50 ns in two-way travel time). Successive depth measurements are made approximately every 10 meters along the plane's track. These are all stacked into the final echogram data product that generally represents travel along approximately 50 km of a flight path. More details of the procedure for synthesizing a single image via SAR can be found in the literature [45].

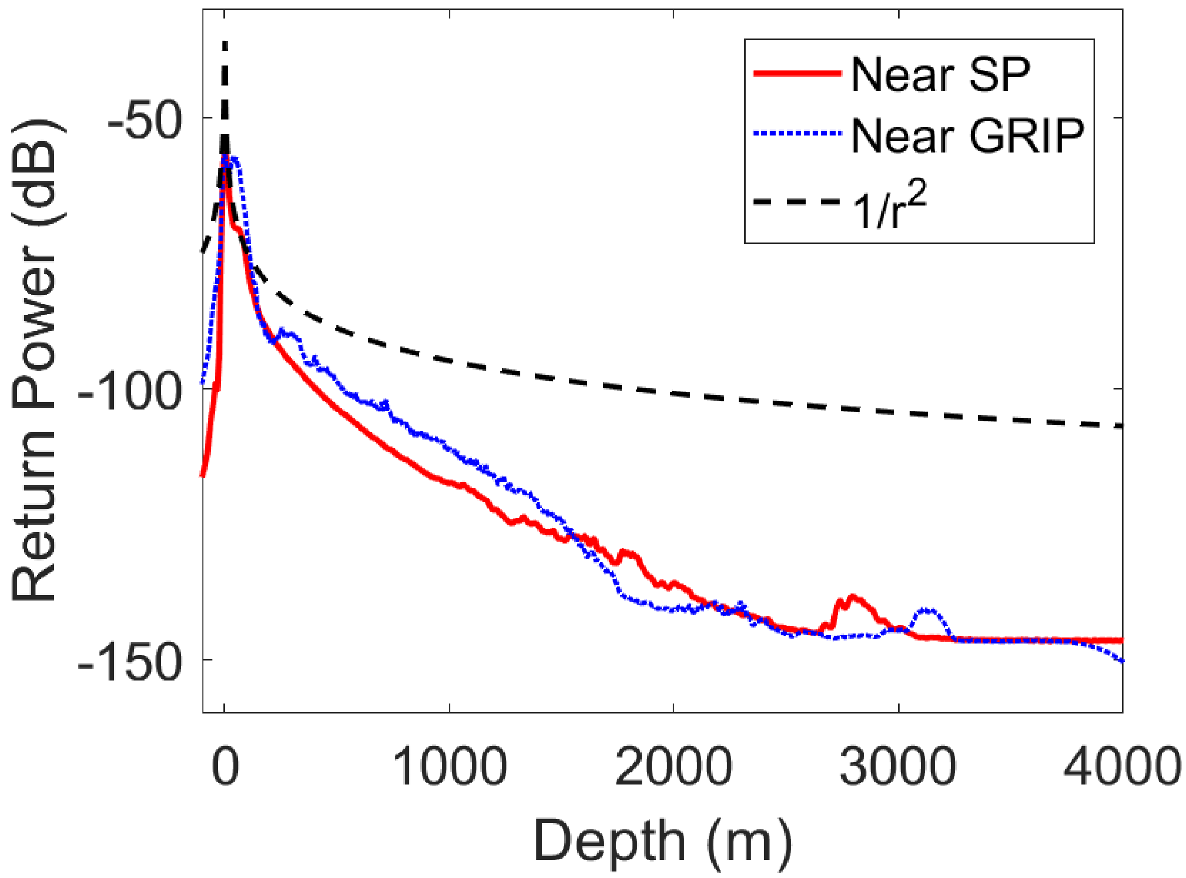

Figure 4.1: Radar traces averaged over a “frame” from near the South Pole and near the GRIP borehole in Greenland. The layering effects at shallower depths are generally more evident in the Greenland data.

4.4 Depth-Dependent Attenuation

Though the goal is to create an attenuation model for the Antarctic ice sheet, most of the methods were developed with the CReSIS data based in Greenland. Not only is the sampling rate higher (which is advantageous in this method), but the ice composition of Greenlandic ice lends itself to this method in a way that Antarctic ice does not. It should also be noted that there are proposed neutrino detectors to be based in Greenland [46], in which case the analysis is still directly applicable. In Greenlandic ice there exist biannual ice layers. In the Summer months, precipitation is "wetter" while in the Winter months it is "drier." These slight dielectric contrasts persist as the biannual layers are buried. There are of course bright contrast layers – jumps of several dB or more along a slowly varying but continuous depth value – present in both Greenlandic and Antarctic ice as the consequence of major events (e.g. volcanoes), however the biannual layers present in Greenlandic ice act to produce a "continuum" in the radar return that is not as obviously present in Antarctic data. Figure 4.1 shows an example of this. It is these sufficiently bright biannual layers (or zones of them, as discussed in Section 2.6) that has allowed for the development of a method to attempt to estimate the depth-dependent attenuation length, which is vital for reconstruction of in-ice neutrino events.

The CReSIS time series show these stacked biannual layers as a noisy continuum of reflectors. This depth-dependent continuum can be modeled as a product of a power law (representing the geometric spreading of the interrogating radar signal and its return as it travels from the plane to the bedrock and back) and an exponential decay (to account for the attenuation due to the ice). This simple model leads to a received amplitude of the form

$$A \propto A_0 \frac{1}{(2a+2r)^{\gamma_0}} \exp\left(\frac{-2r}{L_\alpha}\right), \tag{4.1}$$

where A_0 is the initial transmitted amplitude, a is the altitude of the plane on which the transmitter is mounted, r is the distance in ice to the reflecting layer, γ_0 is the geometric spreading power (to be determined separately), and L_α is the attenuation length. The strongest assumptions are that the intrinsic difference in reflectance of the internal layers is small and that they are each $\ll 1$, so that the transmitted power from layer to layer is ≈ 1. Clough gives typical values of $\frac{\Delta\varepsilon}{\varepsilon}$ for these layers as $\approx 0.001 - 0.002$ [47]. Using the relationship for the reflection coefficient, $|R| = \frac{\pi d}{\lambda}\left(\frac{\Delta\varepsilon}{\varepsilon}\right)$, the given $\frac{\Delta\varepsilon}{\varepsilon}$ values would lead to R values of ≈ 0.0004 for CReSIS wavelengths due to the interference between multiple layers as described in Section 2.6.2. Near the surface, where the ice is assumed to be the coldest, the attenuation length is generally estimated to be more than a kilometer for non-coastal regions. The power law exponent can be determined by limiting the range of the data to be only reflections by layers near the surface, allowing for the exponential term to be set to unity

($\exp\left(\frac{-10m}{1000m}\right) \approx 1$). It is shown below that when this constraint is applied to the data the reflected power falls off as $\frac{1}{r^2}$, or spherical spreading. Setting the power law to $\frac{1}{r^2}$ allows for solving for the attenuation length at any depth. This is done by taking the difference of the power at two depths that are near each other (so that they have approximately the same attenuation length) and calculating how much attenuation there must be to make up the difference between the observed power loss and what is expected just from spherical spreading. By rearranging (4.1) the attenuation (in dB/km when r and a are in meters) between two points with reflected power P_1 and P_2 is given by

$$N_a = \frac{1000}{2(r_2 - r_1)} \left(P_1 - P_2 + 20\log_{10}\left(\frac{r_1 + a_1}{r_2 + a_2}\right)\right). \tag{4.2}$$

Repeating this calculation at many depths (see Fig. 4.2 for example) with varying depth differences per pair to build statistics for a fit allows for an estimate of the attenuation length profile in depth. For a synthetic attenuation length profile, this method can recover the input profile in the middle ice, but is susceptible to large fractional errors in the very low attenuation values at the surface end of the profile which leads to large error bars (Fig. 4.3). This is a consequence of the local extrema of the signal having a larger effect when the underlying attenuation is a low value.

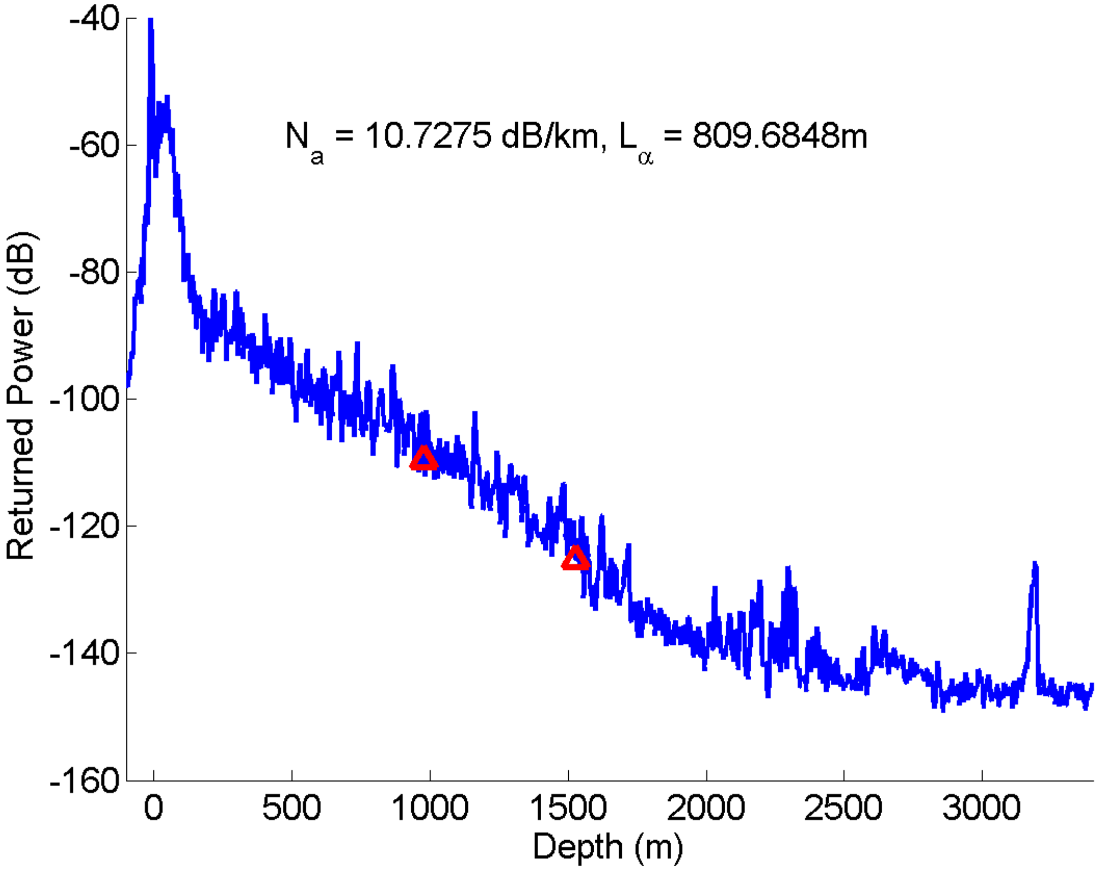

Figure 4.2: The attenuation is estimated between the pair of points at the red triangles. Attenuation is calculated for many such pairs at varying depths to estimate an attenuation length profile in depth.

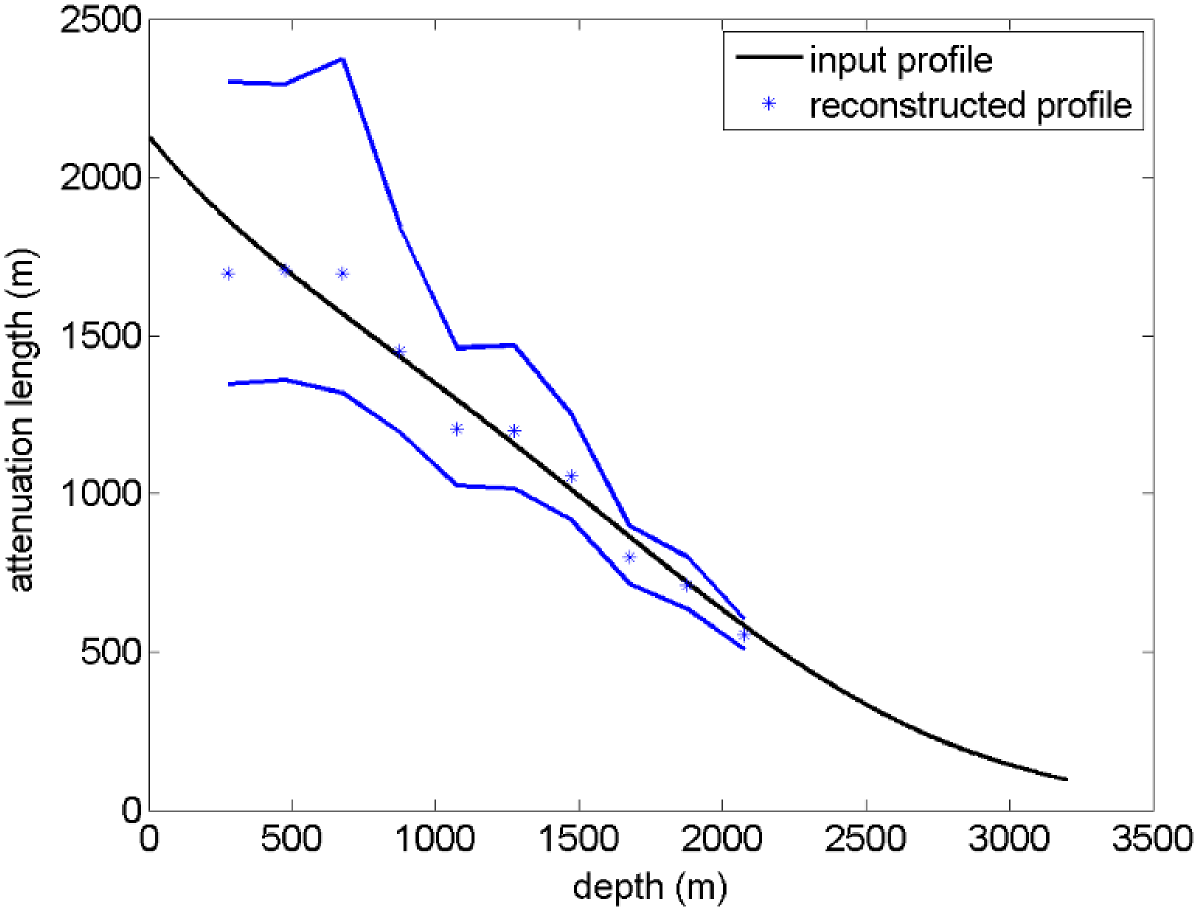

Figure 4.3: The reconstructed attenuation length profile based on modeled radar return with 10dB noise. The solid fit lines represent the 68% confidence levels.

This method fails when there is enough attenuation (deep, warmer ice) that the internal layers can no longer be distinguished from the background noise level, as seen in Figure 4.2 at depths greater than 2500m, for example. This method gives values near the GReenland Icecore Project (GRIP) borehole that are reasonable compared with other modeled profiles. Based on temperature alone, an attenuation length profile can be constructed using the known dependence of ice attenuation length on temperature [19]. Comparing this temperature-driven method using the GRIP temperature profile to the above-detailed method shows disagreement in the upper half of the ice, but similar depth-averaged attenuation values. It is possible that the temperature profile has large errors, as the published GRIP data has a disclaimer that the profile has not been calibrated, however, there is no updated profile, to our knowledge. Other temperature profiles obtained from ice cores in Greenland show a generally similar shape [48].

Another area to be studied with CReSIS data is the birefringence of ice. Birefringence occurs when the propagation speed in a medium is polarization-dependent. Ice has this property due to the fabric crystalline-structure that is a product of the accumulation of snow and the packing due to overburden. Ice flow can then act to align the c-axes of the crystals. While CReSIS does not have multiple polarizations, the incident pulse will likely be off-axis compared to the internal structure of the ice, being split into the two inherent polarizations of the ice. This will produce a double reflection from the bedrock, as the portion of the incident wave that is projected into the "faster" polarization of the ice will arrive before the "slower" projection. Initial results show this to be a several tenths of a percent effect on arrival times [49, 34].

4.5 Estimating Radio-Frequency Attenuation Length from CReSIS Data

There have been many previous measurements of the RF attenuation length of cold polar ice [50, 51, 52, 53, 54, 55, 26, 56, 18]; these typically are measures of the depth-averaged ice sheet attenuation length and do not actually unfold the depth-dependence. Such a dependence can be modeled using lab- and ice core-derived data on the behavior of ice crystals as a function of temperature and impurity [20, 57]. Unfortunately, ice core data do not readily lend themselves to direct *in situ* RF attenuation length measurements, which ideally are made over continuous ice volumes comparable in scale to the attenuation length itself.

Here, we present two estimates of attenuation length. First, we have attempted to estimate the depth-dependence of the RF attenuation length under the assumption that the underlying shape of the CReSIS radar return strength variation with depth, below the surface and to a depth of $\sim$2000 m, is the result of some form of coherent scattering (return power $\sim 1/r^2$), corresponding to discrete layer scattering with no loss of phase coherence across a wavefront. Defining the total distance r from transmitter to reflecting point as the sum of the height of the plane h and the ice depth of the reflector z, we characterize the measured returned power $P(z)$ in terms of a depth-dependent power law exponent $\gamma(z)$:

$$P(z) \sim z^{-\gamma(z)}. \tag{4.3}$$

Thus, γ represents the combined effect of flux-spreading plus ice absorption of RF, with large absorption corresponding to high values of γ. If we assume the flux spreading varies with a constant power law exponent γ_0, then we can write the ratio of the measured returned power from a shallow depth z_s ($P(z_s)$) relative to the power measured from a greater depth z_d ($P(z_d)$), taking into account both flux spreading and also absorption, as

$$P(z_d)/P(z_s) = (z_s^{-\gamma_0}/z_d^{-\gamma_0})exp(-2|z_d - z_s|/L_\alpha(\bar{z})), \tag{4.4}$$

where $L_\alpha(\bar{z})$ is the average radio-frequency field attenuation length over the interval between z_d and z_s. By taking ratios of signal strengths, as a function of depth into the echogram, we can solve for L_α once γ_0 is known. If the two points z_d and z_s are separated by a length somewhat smaller/larger than one RF attenuation length, then we expect flux spreading/attenuation to dominate the relative power. For data taken by CReSIS, the distance dependence of the returned power is additionally complicated by the beam pattern of the transmitter and receiver as well as the focusing expected as the signal penetrates across the dielectric discontinuity of the ice surface, for which we must apply explicit corrections. The values $\gamma_0 = 2$ and $\gamma_0 = 4$ correspond to spherical spreading with either coherent, or incoherent scattering, respectively

We use RDS data taken near the GRIP borehole site in Summit, Greenland for this analysis.

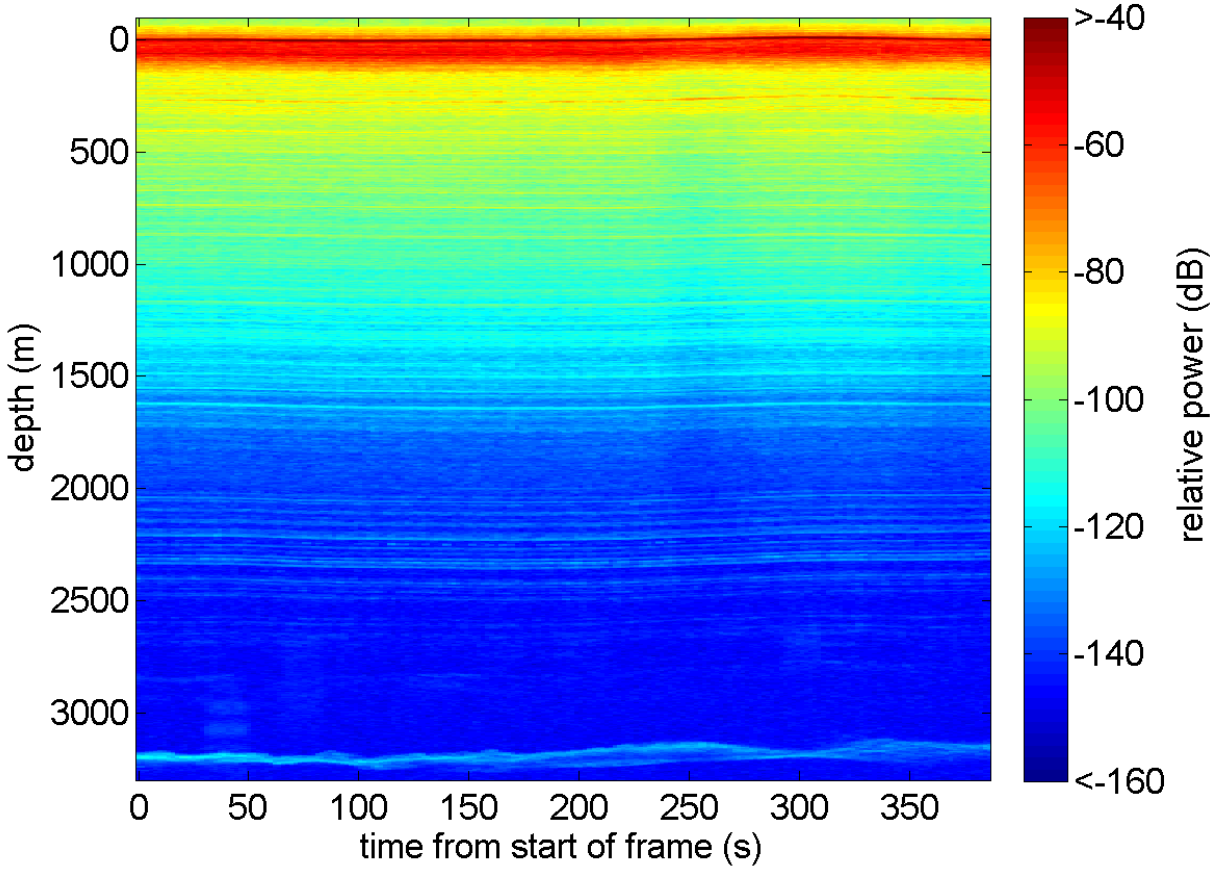

Figure 4.4: CReSIS echogram from near the GRIP borehole site in Summit, Greenland. Both the surface and the bedrock returns (at ≈3200m) are apparent in the Figure.

A sample CReSIS echogram drawn from those data is shown in Figure 4.4. Clearly visible is the relatively flat surface return across the echogram, as well as the relatively flat bedrock return near the bottom of the image, and below the "echo-free zone" from ∼2400-3200 m in depth.

4.5.1 Calculations

Based on the temperature profile, the near-surface, colder ice should have longer attenuation lengths than the deeper ice (particularly close to the bed) and therefore provides a good estimate for the minimum γ ("γ_0"), from which we can bootstrap and extrapolate into deeper layers, where the effect of attenuation/absorption will become increasingly noticeable. First, we estimate γ_0 from the observed returned power just below the firn. We then hold γ_0 fixed and calculate the attenu-

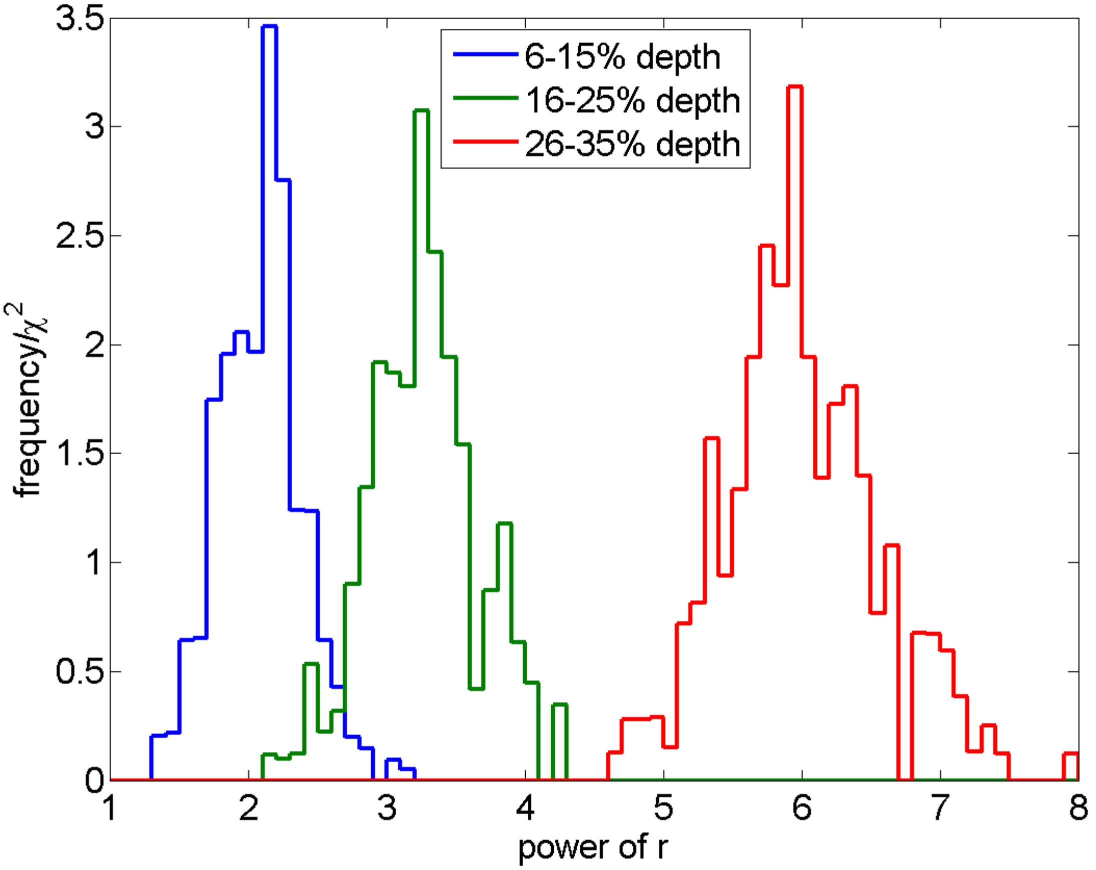

Figure 4.5: Best-fit power γ for various depths into GRIP echogram. Consistent with increasing absorption of radio frequency signal with depth, power exponent monotonically increases with depth.

ation length for random segments of length 400–550 m (i.e., 400 m$< z_d - z_s <$550 m using the notation above), selected from the depth interval below the surface return and above the "echo-free zone" [58] for the near-GRIP echogram. The varying segment length is chosen to be large enough so as to average over fluctuations, but sufficiently small such that the attenuation value across the segment should be relatively constant. For each segment, the attenuation from the first point to the last point is calculated as the loss beyond $z^{-\gamma_0}$.

To determine the reference power law exponent, and also to qualitatively investigate the depth-dependence of attenuation, we have fit the power γ as a function of depth z. Figure 4.5 shows that the fitted exponent follows the temperature-based expectation of an increasing power law exponent with depth. We find that γ=2 provides a good fit to our data for the shallowest ice, and retain γ_0=2 as our 'reference' for the remainder of the analysis.

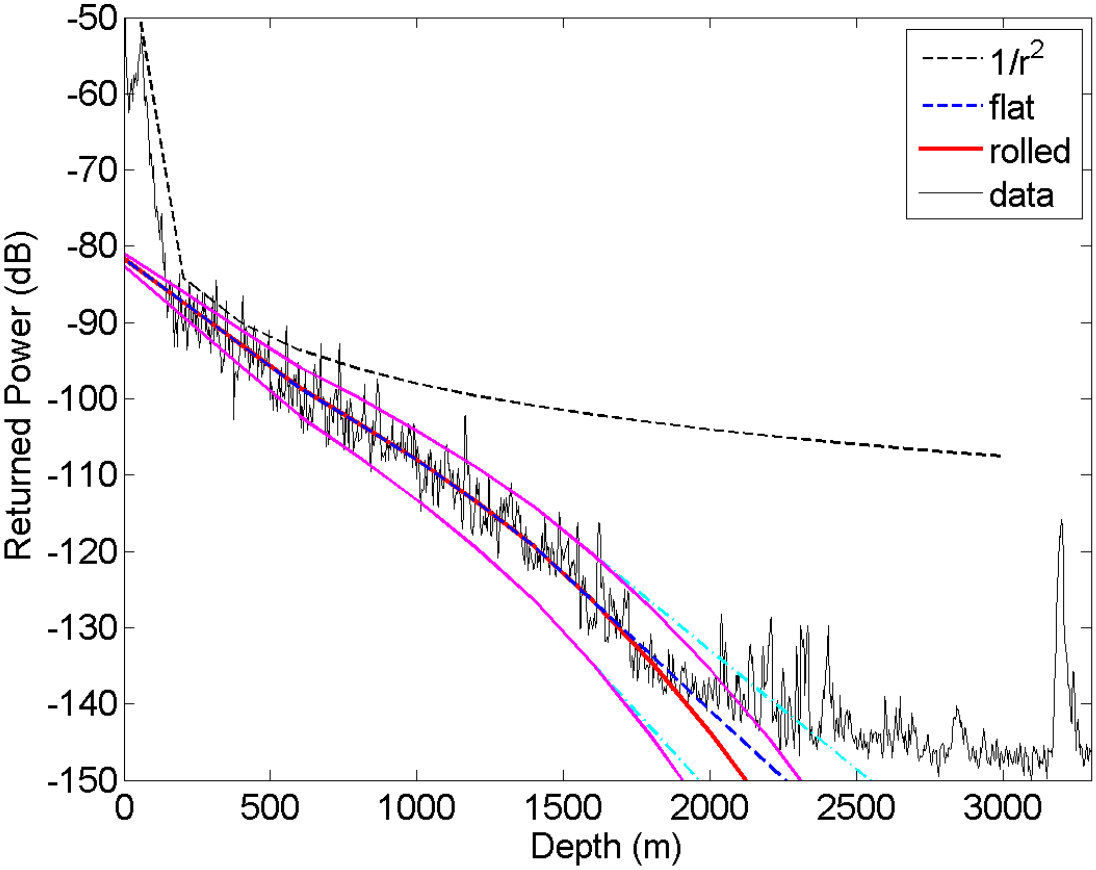

Figure 4.6: Sample CReSIS radar return, with expectation of signal strength as a function of depth from geometric spreading only ($\propto z^{-2}$) overlaid, showing a clear deficit of signal compared to the lossless hypothesis. Also shown is the actual fit resulting from our analysis, with two extrapolations shown into the shallow and deep regions of the echogram for which we have very limited sensitivity, as well as these values varied by ±15% relative to measurement in Figure 4.7, illustrating stability of extracted results. Magenta shows band corresponding to "rolled" extrapolation model; cyan shows band corresponding to "flat" extrapolation model.

The depth-dependent attenuation is similarly illustrated in Figure 4.6, where an extrapolation of the simple-minded, $P(z) \propto z^{-2}$ power flux spreading, from the shallow region of the echogram into the deeper part of the echogram, results in an increasing excess of expected power relative to observation.

The results of our segment-based estimation procedure are displayed in Figure 4.7; we directly measure the attenuation length over the inner half of the ice sheet. The lower part of the ice sheet (other than at the base itself) corresponds to returns that are smaller in amplitude than the threshold of the receiver. In order to obtain an ‘average’ attenuation length over the entire depth of the ice sheet, we must invoke some model describing how the attenuation evolves with depth. We consider two extreme cases: 1) A “flat” model, in which the attenuation length beyond the depth region to which we are sensitive in this analysis is assumed to be constant beyond the measurement region; i.e., we extrapolate our measurement at 1000 m into the interval 0–1000 meters, and extrapolate our measurement at 2000 meters into bedrock, or 2) a “rolled” model, in which the attenuation length is assumed to follow laboratory-based expectations for the dependence of radio frequency ice attenuation length with temperature [59], combined with the measured GRIP temperature profile.

Also shown in Fig. 4.7 are $\pm 1\sigma$ error bands in black, based on the observed statistical variation in the measured attenuation, as a function of depth.

To test the stability of our final result, Figure 4.6 shows the curves which would result by scaling our best-fit attenuation length profile either up or down by $\pm 15\%$. We note that the curve overlay with the data is noticeably poorer after such a scaling, indicating that our best-fit minimum is satisfactorily deep.

4.6 Extraction of Average Attenuation Length from Surface and Bedrock Echoes

Our depth-averaged attenuation length value above can be compared with the value obtained by simply comparing the magnitude of the ice surface vs. bedrock reflection strengths and attributing all losses beyond geometrical spreading to attenuation. In terms of the variables presented above

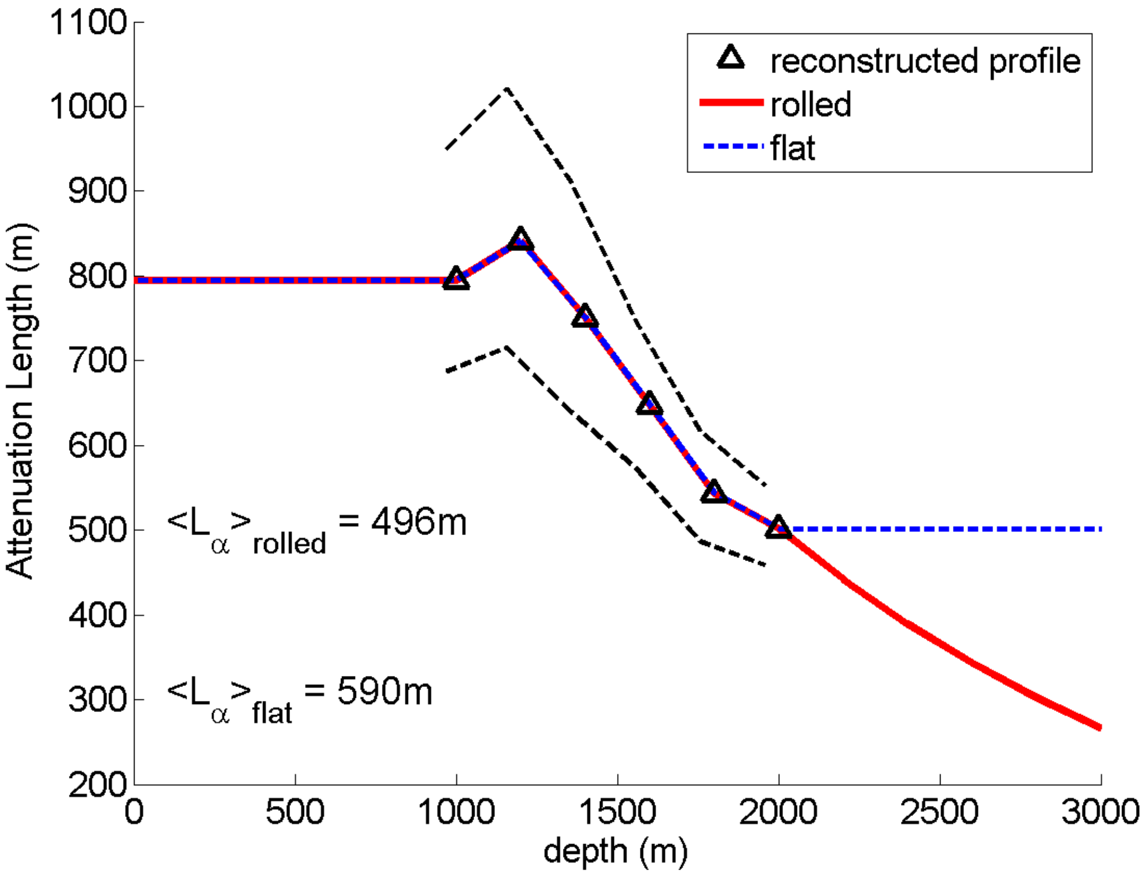

Figure 4.7: Attenuation length, as a function of depth, based on decreasing signal strength with depth, as described in text.

in (4.4) the attenuation length is given as

$$L_\alpha = \frac{-2(z_d - z_s)}{\ln\left(\frac{P(z_d)z_d^{-2}}{P(z_s)z_s^{-2}}\right)}. \tag{4.5}$$

4.6.1 Ice Focusing

Note that there is an additional geometric correction which must be applied to the bedrock reflection owing to the fact that rays ‘focus’ towards the vertical on their downward path; this is only partially compensated for by the ‘de-focusing’ on the reflected, upward path back towards the plane-borne receiver, as shown in Figure 4.8. To estimate this correction, we simply take the ratio of received flux density for a ray cone traced through the air-ice interface with and without refraction effects as a function of the signal transmission/reception geometry. Assuming a small opening angle for this cone, we parametrize this correction with the form:

$$\frac{P_{refracted}}{P_{non-refracted}} = \left(\frac{a+z}{a+\frac{n_{air}}{n_{ice}}z}\right)^2, \tag{4.6}$$

where a is the altitude of the plane at the time of the radar shot, z is the ice thickness, $n_{air} \approx 1$ and $n_{ice} = \sqrt{3.15}$. This is geometrically derived as shown in Fig. 4.9. For a ground-based measurement, this correction would simplify to n_{ice}^2, as shown in Figure 4.10. The amplitude correction is shown in Figure 4.11 as a function of the ice depth at a particular location and the plane altitude; overall, our attenuation length results are approximately 10% larger without this correction applied. However, for estimated attenuation lengths near the high end of our range this value is closer to 20%. For a ground-based measurement near the GRIP site, the change to the estimated attenuation values would scale as shown in Figure 4.12.

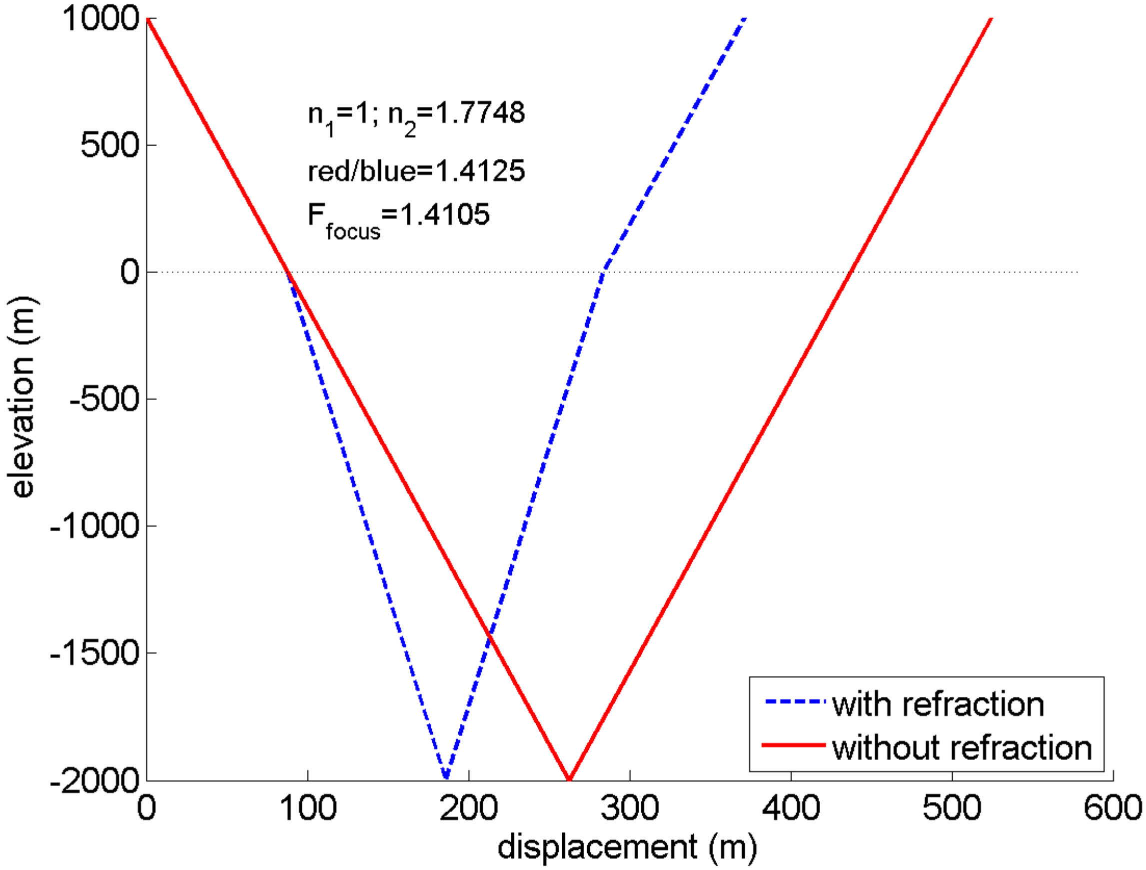

Figure 4.8: Ray cone traced through air-ice transition with and without refraction to determine the focusing correction, at an altitude of 1000m. The opening angle of the cone is 10°(note unequal axis scaling). F_{focus} refers to the factor from (4.6) while red/blue is the calculated ratio of the radii of the non-refracted:refracted cones.

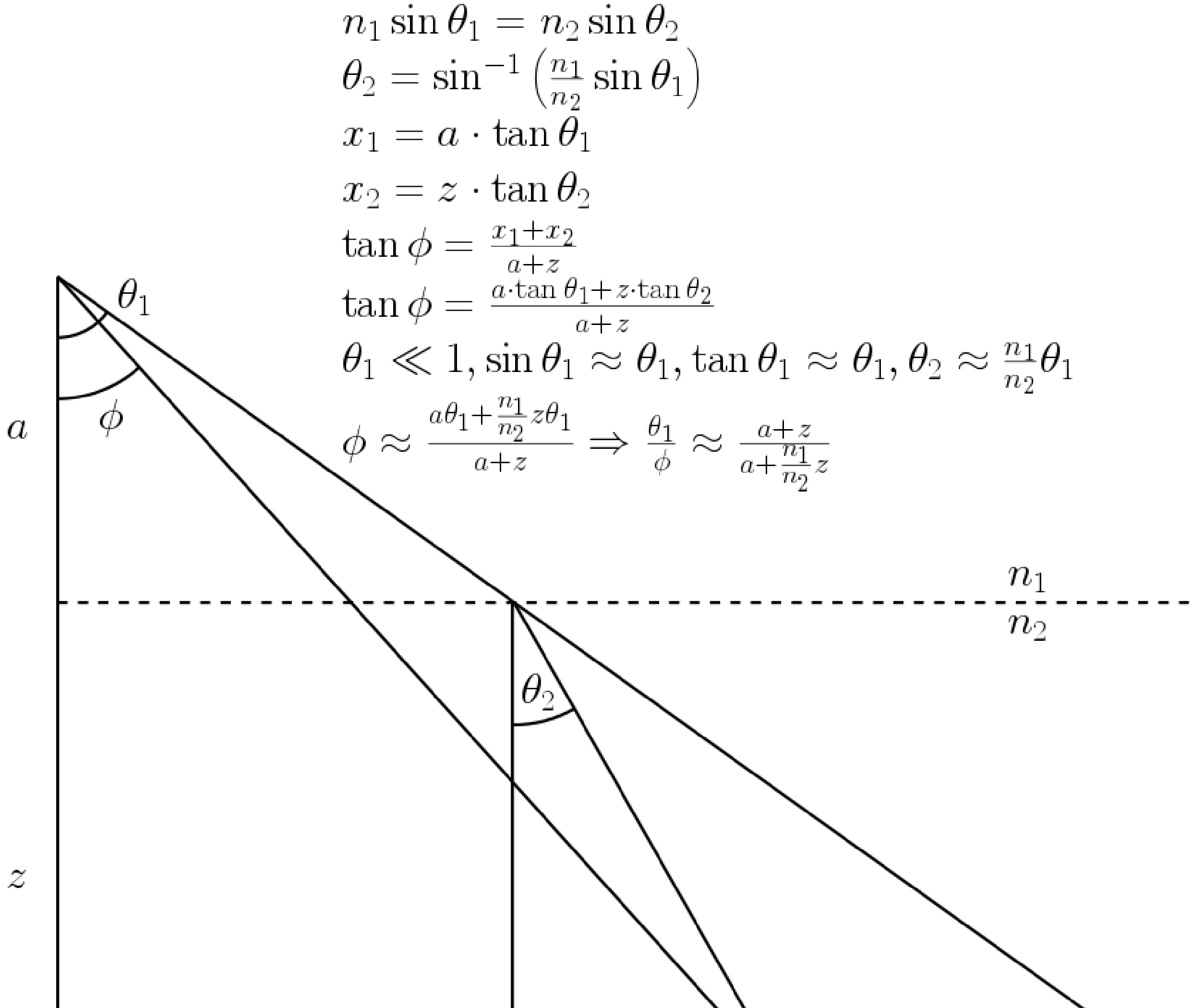

Figure 4.9: Geometric derivation of the focusing correction starting with Snell's Law.

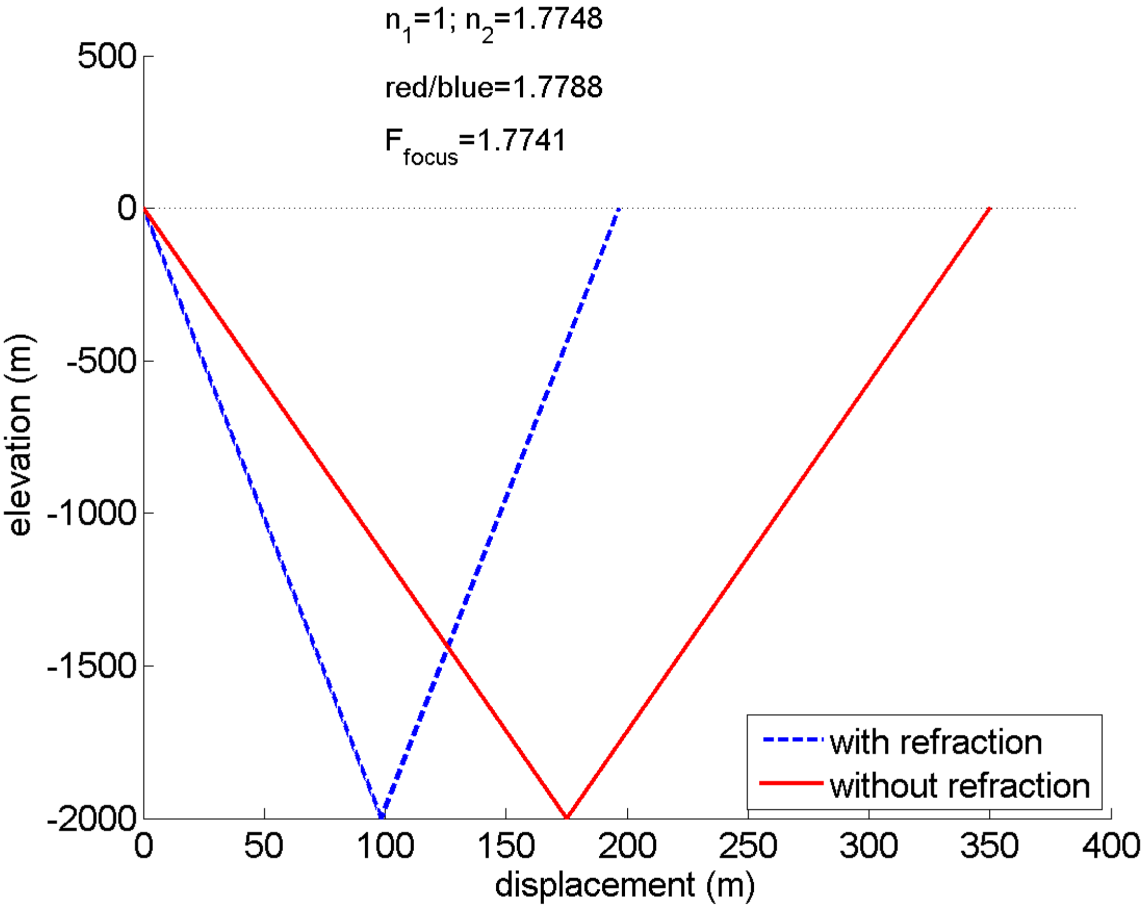

Figure 4.10: Ray cone traced through air-ice transition with and without refraction to determine the focusing correction, at an altitude of 1m. The opening angle of the cone is 10°(note unequal axis scaling). F_{focus} refers to the factor from (4.6) while red/blue is the calculated ratio of the radii of the non-refracted:refracted cones.

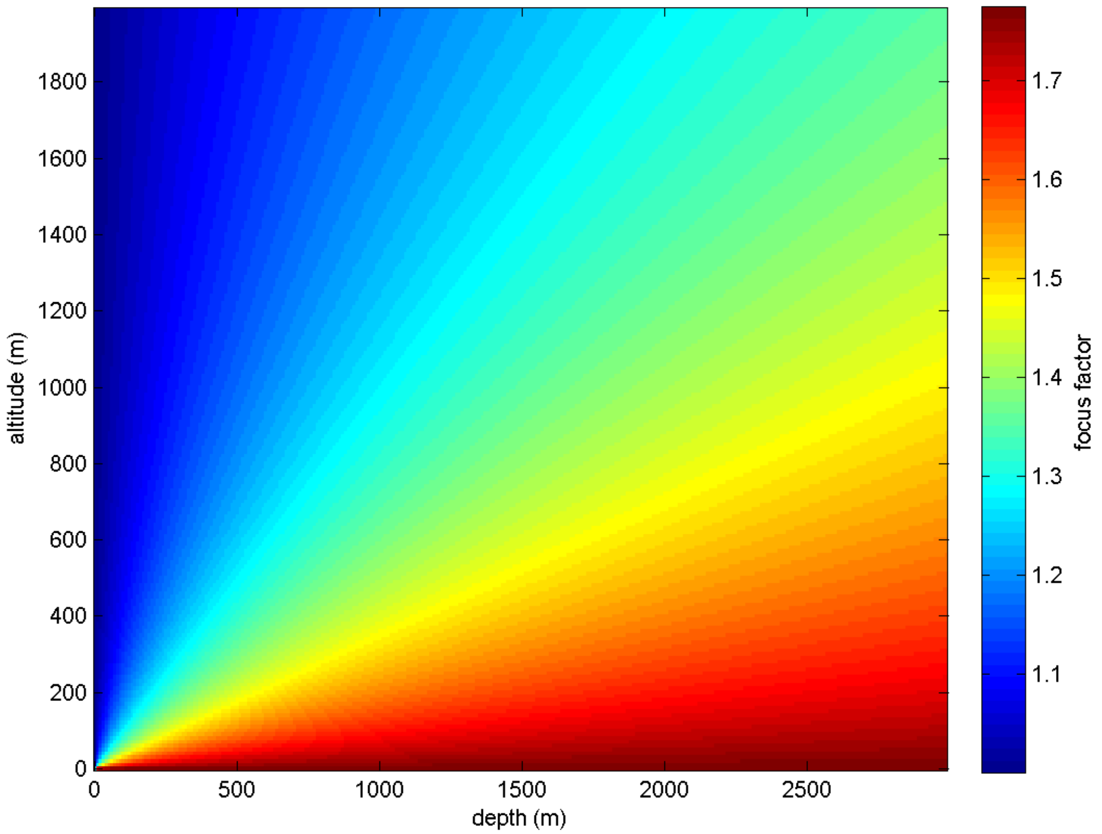

Figure 4.11: Geometric amplitude correction factor, as a function of ice depth and plane altitude, due to ice focusing, as discussed in text.

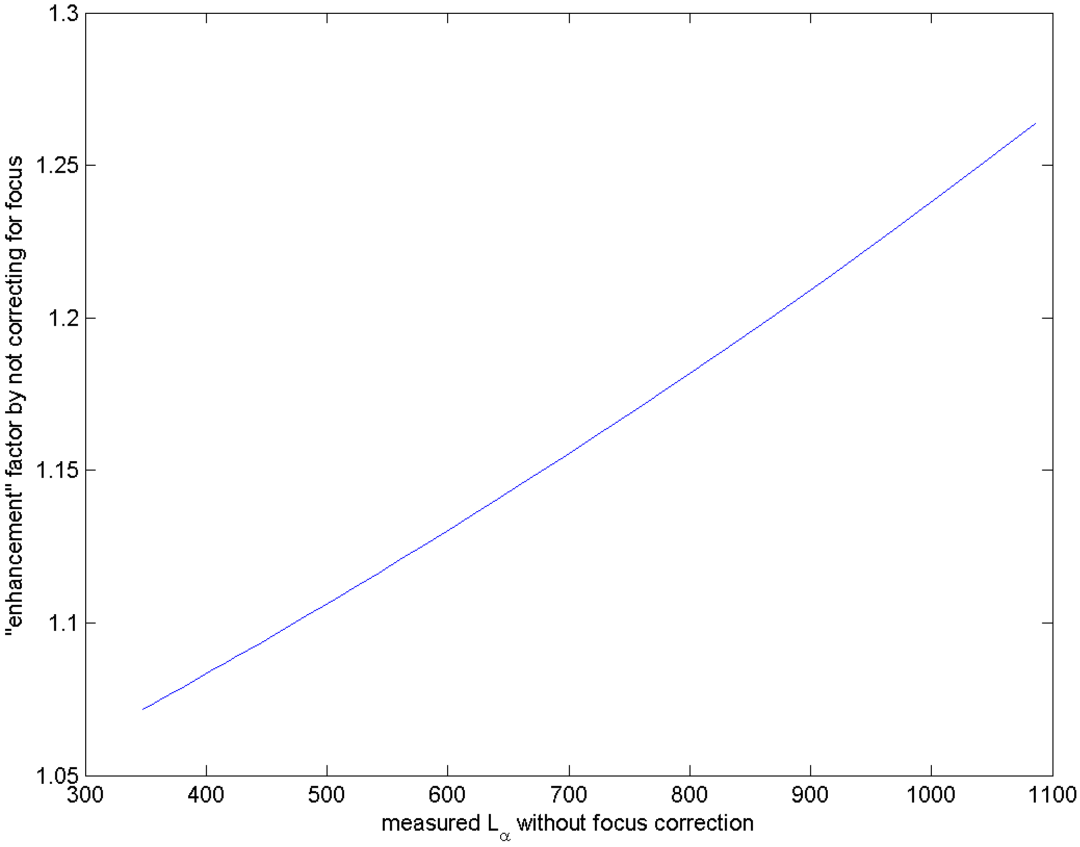

Figure 4.12: For sampling geometry similar to a ground-based measurement near the GRIP site (altitude of 0 m, depth approximately 3000 m), not accounting for the ice focusing would scale the reported attenuation lengths up by a factor depending on the attenuation length.

4.6.2 Systematic Errors

Systematic errors in this second approach, based only on the magnitude of the bedrock:surface echo return (modulo the geometric correction discussed above) include:

1. The several dB uncertainty in the gain of the CReSIS receiver system at the time the two returns are recorded. In particular, the gain of the system at the time the surface return is recorded is smaller than the system gain at the time the bedrock return is recorded, to avoid saturation of the DAQ dynamic range by the bright surface return.

2. Uncertainty in the reflection coefficient of the surface and also bedrock, detailed in Section 4.6.2.1.

3. Uncertainty in the 'smoothness' of the surface and bedrock reflectors, detailed in Section 4.6.2.2

4. The uncertainty in the depth of the ice sheet factors directly into the calculation of the attenuation length. The quoted CReSIS ice depth uncertainty is approximately 5 meters, although we note that, for points where CReSIS data overlaps with BEDMAP2 data (same latitude/-longitude), there are discrepancies in the bottom depth that sometimes exceed hundreds of meters. Assuming an overall uncertainty of order 10 meters has a negligible effect on our quoted attenuation lengths, relative to other systematic errors probed.

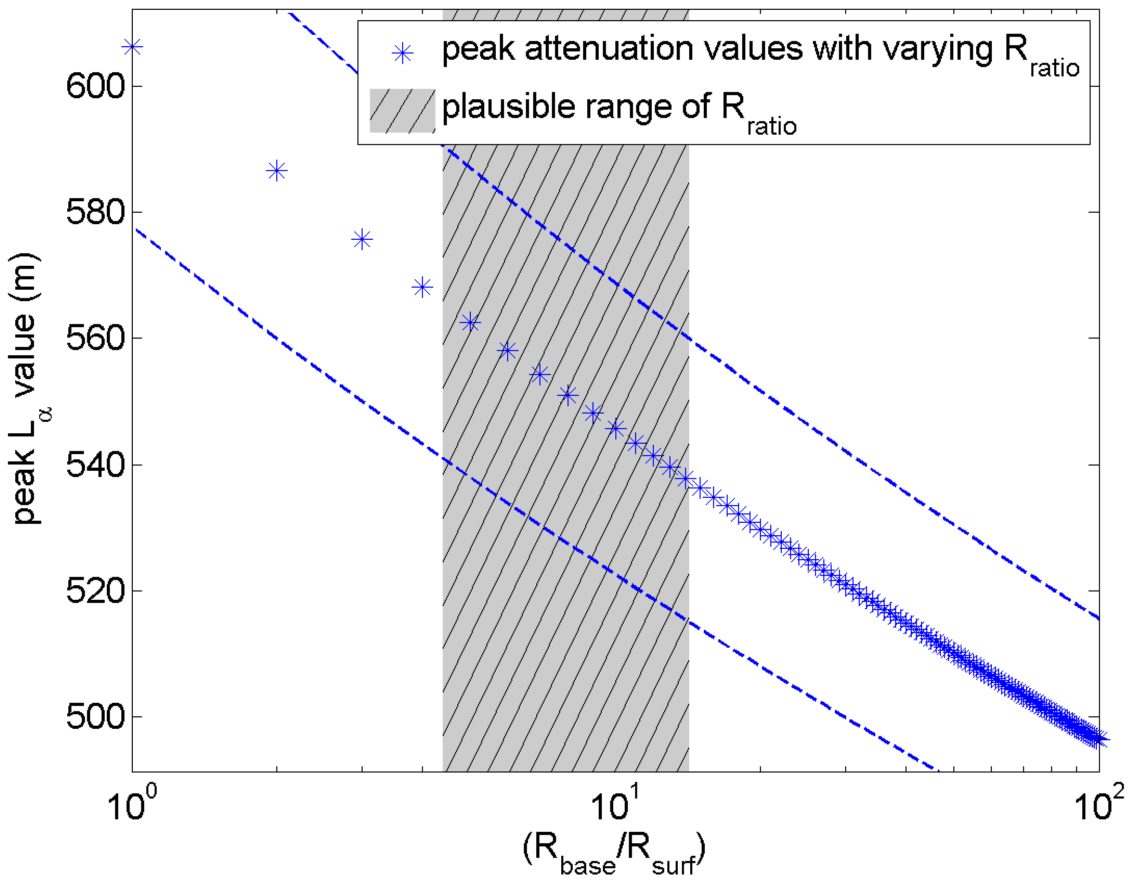

Figure 4.13: Calculated value of field attenuation length as a function of assumed relative bedrock:surface reflectivity. The dashed lines represent the uncertainty in the attenuation length as described in the text. The plausible range comes from $R_{base} \approx 11 \rightarrow 27\%$ and $R_{surf} \approx 2\%$ as outlined in the text.

4.6.2.1 Reflectivity Ratio

There is some uncertainty in the reflection coefficient of the surface and bedrock returns due to uncertainty in the dielectric contrast [60]. For the surface return, the reflected power at normal incidence plausibly varies from 1.9→2.5%, corresponding to surface index-of-refraction values of 1.32→1.38. For bedrock, assuming a dry rock-ice interface, the permittivity may range from 4–5 ($2 < n < 2.23$) for sedimentary rock vs. 6–10 ($2.45 < n < 3.16$) for massive rock, resulting in a possible variation in the reflected power from 11.1→26.9%. If there is a water layer between bedrock and the bottom of the ice sheet, then the reflectivity increases to ∼65%, although this should be clearly evident as a marked geographical discontinuity in the calculated attenuation length, as a function of position, which is not observed in our analysis.

In our analysis, we assume a ratio of 10:1 basal power reflection coefficient:surface power reflection coefficient; ultimately, our results are fairly insensitive to reasonable variations in this assumption. Figure 4.13 shows the dependence of the extracted attenuation length on the assumed value of the relative bedrock:surface reflectivity, with our default value (10) and our estimated error bars indicated on the graph.

4.6.2.2 Smoothness and Possible Depolarization Effects

Here, we assume that the scale of surface inhomogeneities is small relative to one wavelength, corresponding to 2 meters in air and roughly 1.3 meters in ice. Under that assumption, scattering is considered to be specular, corresponding to $1/r^2$ power diminution rather than the $1/r^4$ that would be characteristic of diffuse, incoherent scattering. This is, in fact, borne out in our analysis for γ_0 detailed previously. If there were, in fact, total decoherence at the bedrock, the scattered signal would be unobservably small.

The observed variation in the measured surface return strength over a near-GRIP echogram is shown in Figure 4.14; the width of that distribution corresponds to a variation of order 2 dB, which should bracket the possible effects of surface roughness. This indicates there is are sufficiently small variations to the local reflection coefficient such that surface roughness can be ignored. We note that a balloon-borne survey of Antarctica mapped the solar radio-frequency signal (integrated from 200 MHz – 1200 MHz), as observed in its surface reflection[61]. By comparing the strength of the surface reflection with the direct solar radio-frequency signal strength, the reflectivity of the surface was derived. That study found good agreement with the Fresnel coefficients expected at the snow-air interface, again arguing against significant scattering signal loss over the RF frequency band.

The corresponding distribution for the measured bedrock return strength is shown in Figure 4.15, having a variation approximately 2–3 times as large as that of the surface. In this case,

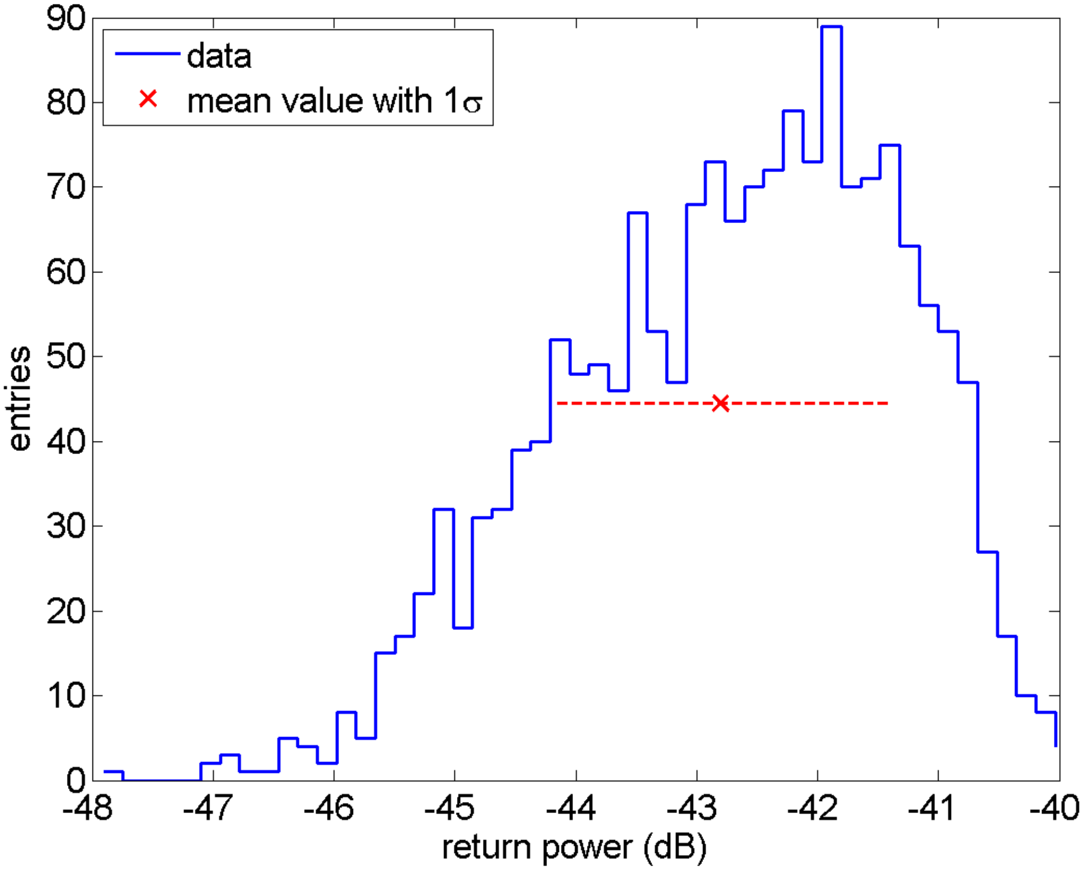

Figure 4.14: Surface return strength (in dB) for all "shots" in echogram taken in vicinity of GRIP. Standard deviation (sigma) of distribution is 1.38 dB.

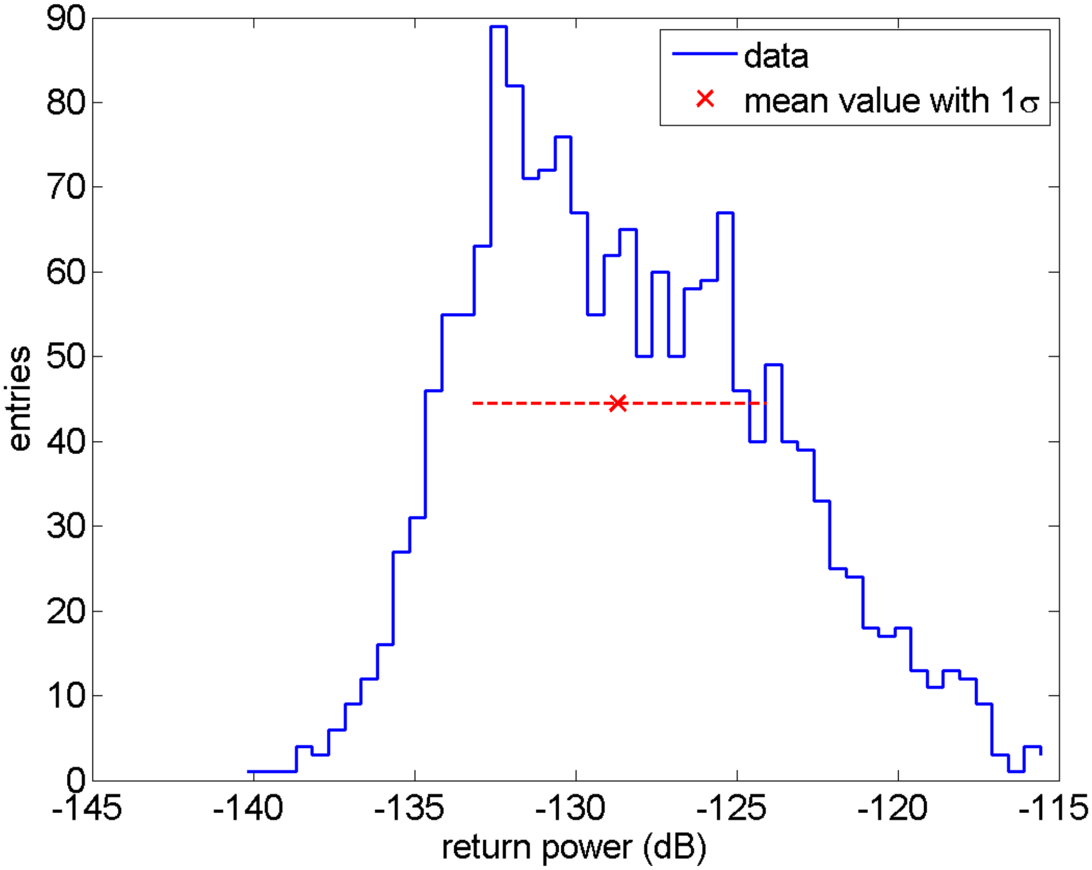

Figure 4.15: Bedrock return strength (in dB) for all “shots” in echogram taken in vicinity of GRIP. Standard deviation (sigma) of distribution is 4.61 dB.

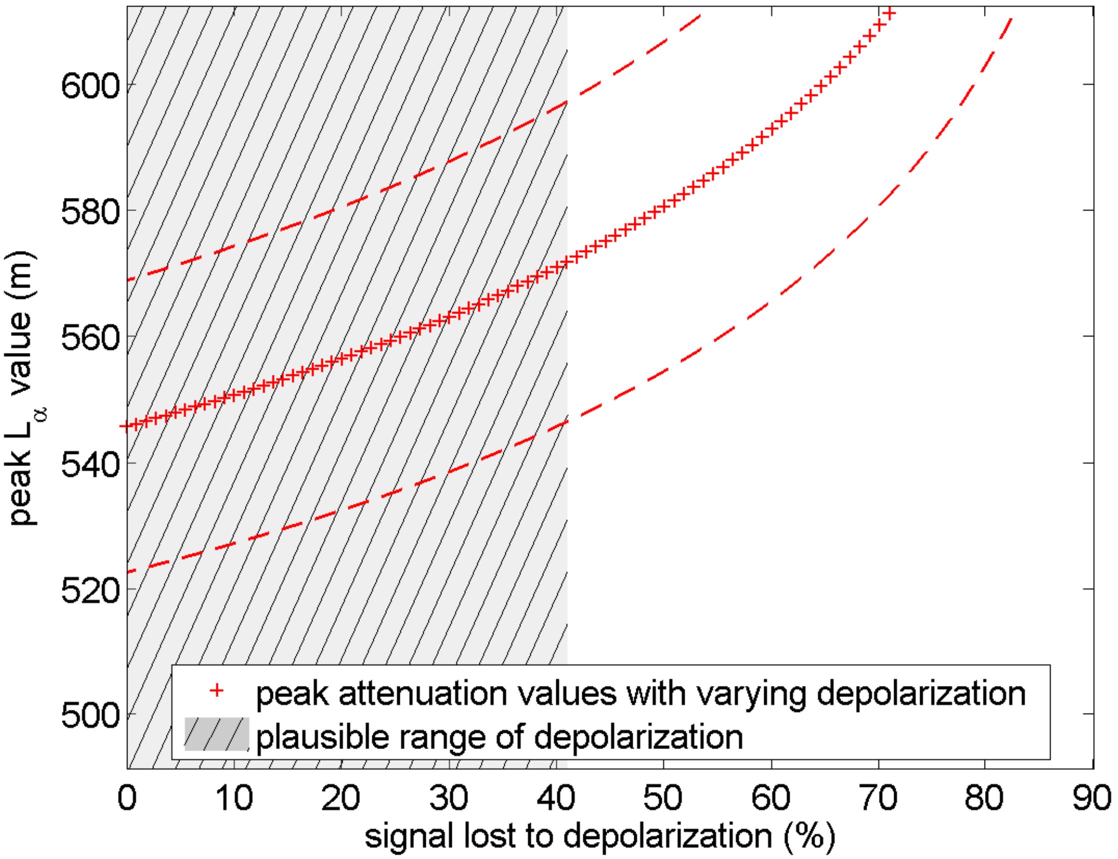

Figure 4.16: Estimated systematic error on GRIP attenuation length due to possible depolarization at bedrock. Vertical dashed curves above and below central curve indicate systematic errors estimated from other effects, as described in text.

depolarization may weaken the return signal strength, as noted above. To quantify the possible effect that a depolarized bedrock echo may have on our calculated value of attenuation length, Fig. 4.16 indicates our default value of calculated attenuation length (zero depolarization), as well as the curve obtained from varying amounts of depolarization. If we attribute the entire width (4.6 dB or $\approx 40\%$ signal loss) of our bedrock echo return distribution to depolarization effects, our calculated near-GRIP attenuation length increases from 546 meters to 572 meters. The plausible range is determined from the argument that the depolarization effect could not be greater than the width of the basal return distribution.

Figure 4.17 illustrates the attenuation length values calculated from the bedrock:surface return

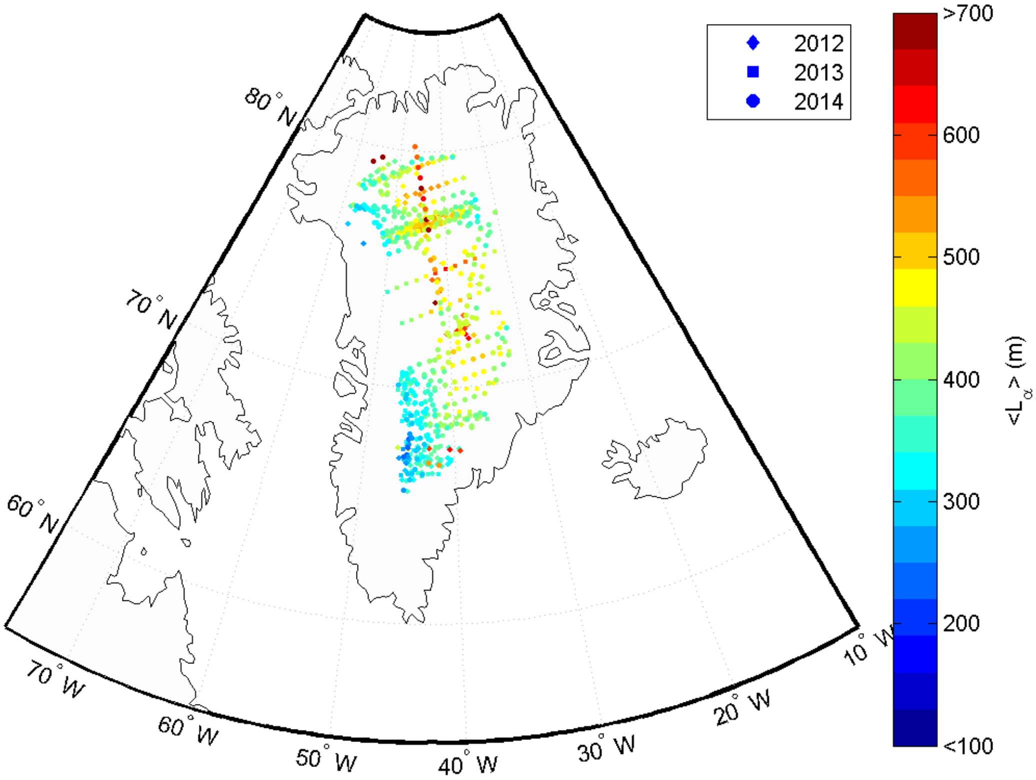

Figure 4.17: Summary of Greenland attenuation lengths derived from direct ratio of measured surface return strength to bedrock return strength.

intensities using the full analyzed CReSIS Greenland data.

4.6.2.3 Other Uncertainties

In addition to the reflectivity uncertainties mentioned above, uncertainties due to roughness, e.g., are estimated from the shape of the derived attenuation length distribution using an ensemble of CReSIS echograms. For every "shot" of the radar, comprising one individual up/down recorded radar return, the attenuation is calculated using the measured values of the surface and basal returns, accounting for geometric spreading, differences in surface and basal reflection coefficients as prescribed above, and ice focusing. For a given echogram (roughly 2000 "shots"), a distribution of these attenuation values is made. For the near-GRIP data, the distribution of attenuation lengths,

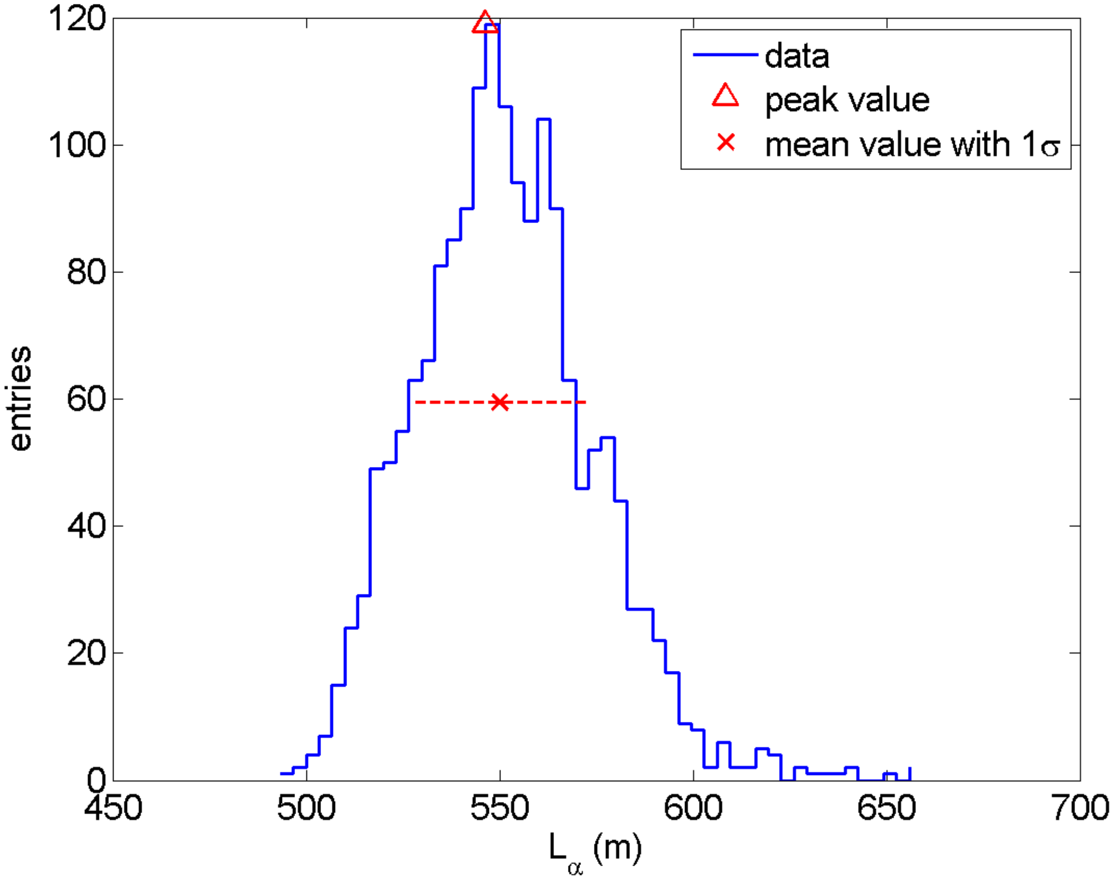

Figure 4.18: Attenuation length distribution for data taken in vicinity of GRIP.

with a single attenuation length derived from a single “shot” is shown in Figure 4.18.

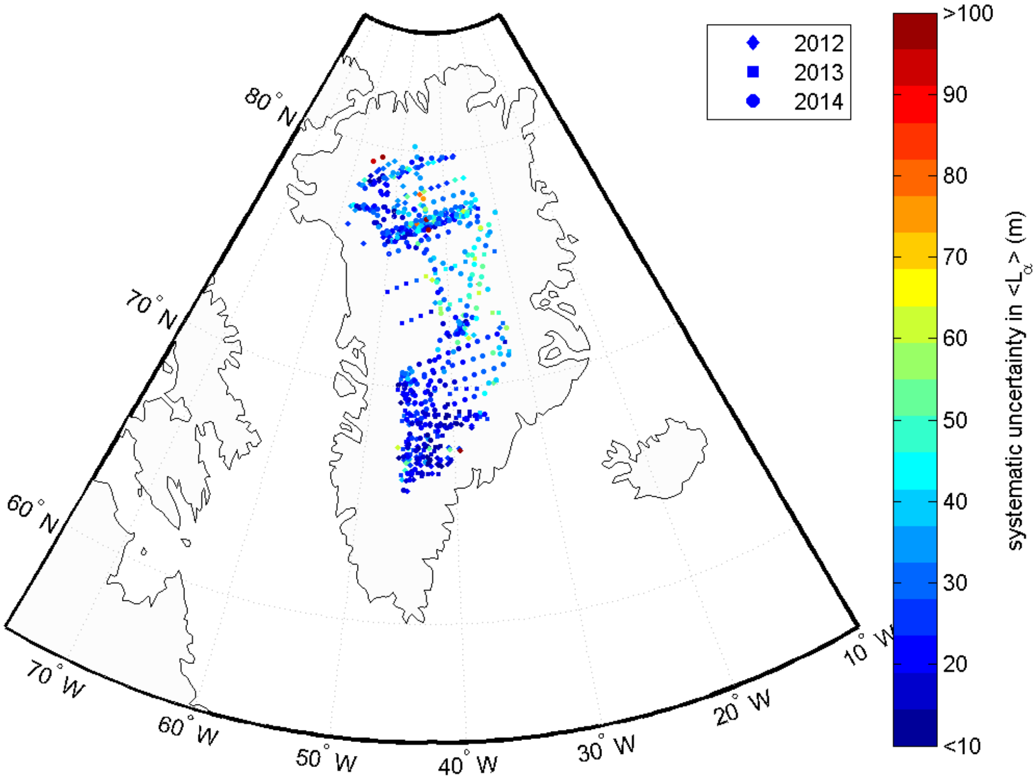

Figure 4.19: Estimated error in Greenland attenuation lengths, as described in text.

We take the deviation between the *peak* x-value x_{max} of that distribution and the *mean* of that distribution $\bar{x}$, added in quadrature with the standard deviation of that distribution σ_x (generally larger than the deviation between peak and mean) as indicative of effects due to surface and basal roughness. Note that the peak value, rather than the mean value, is used as our 'default' estimate, as it is somewhat more immune to tails in the distribution. The overall estimated point-to-point systematic errors, defined, as above as $\sqrt{(x_{max}-\bar{x})^2+\sigma_x^2}$, are presented in Figure 4.19 for the Greenland data set. Attenuation lengths, and corresponding errors, similarly calculated from the 2010–2014 CReSIS Antarctic data sets are shown in Figures 4.20 and 4.21, respectively.

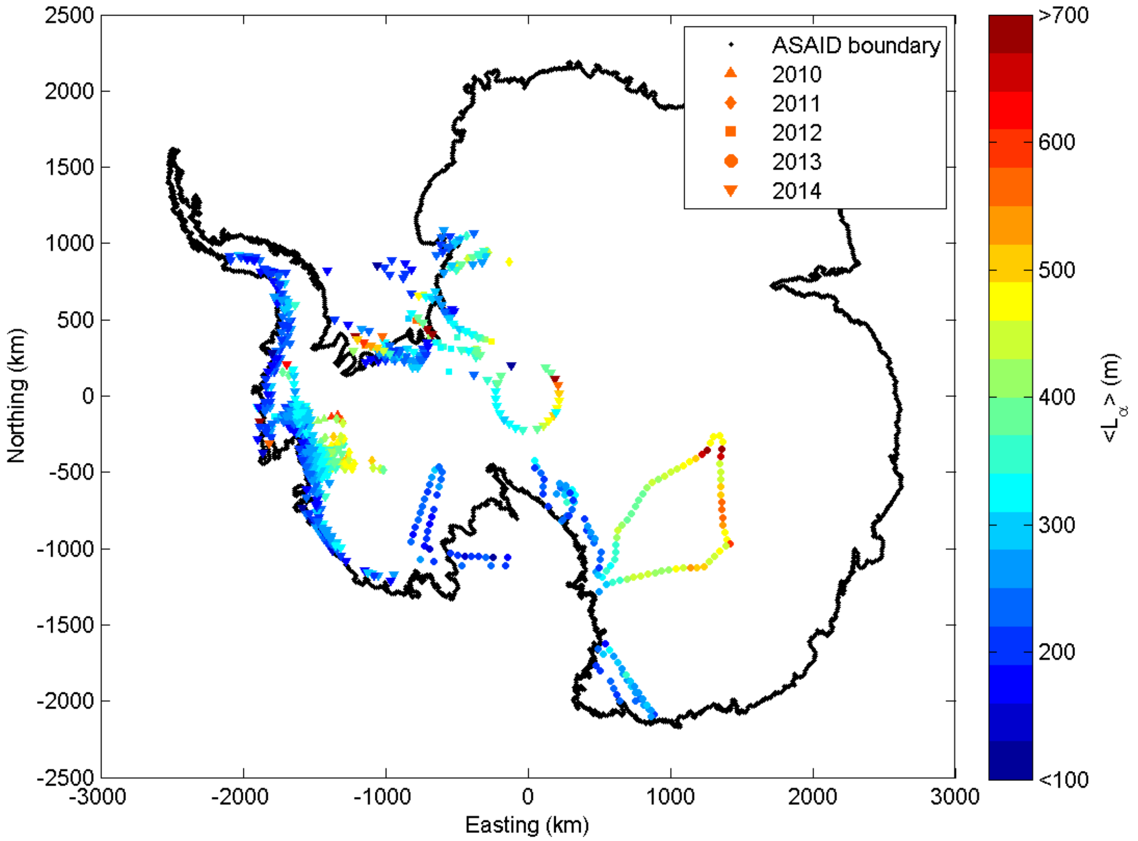

Figure 4.20: Summary of Antarctic attenuation lengths derived from direct ratio of measured surface return strength to bedrock return strength.

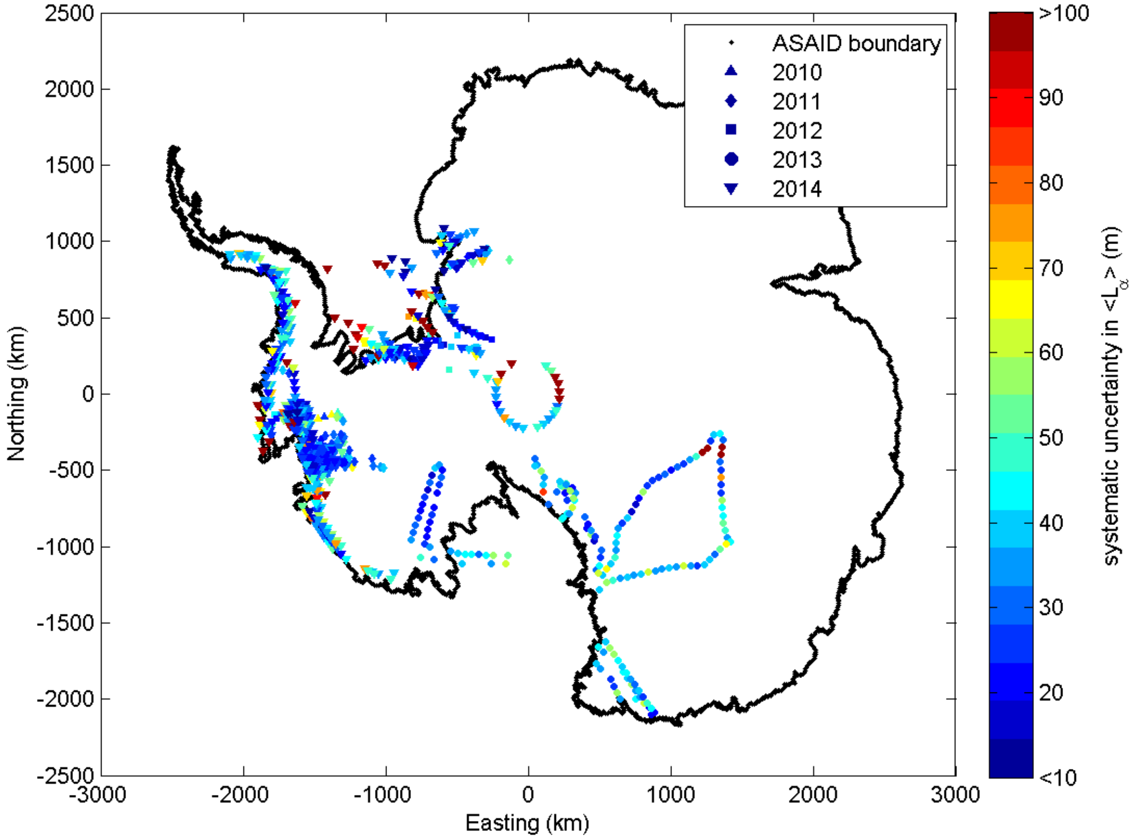

Figure 4.21: Estimated error in Antarctic attenuation lengths, as described in text.

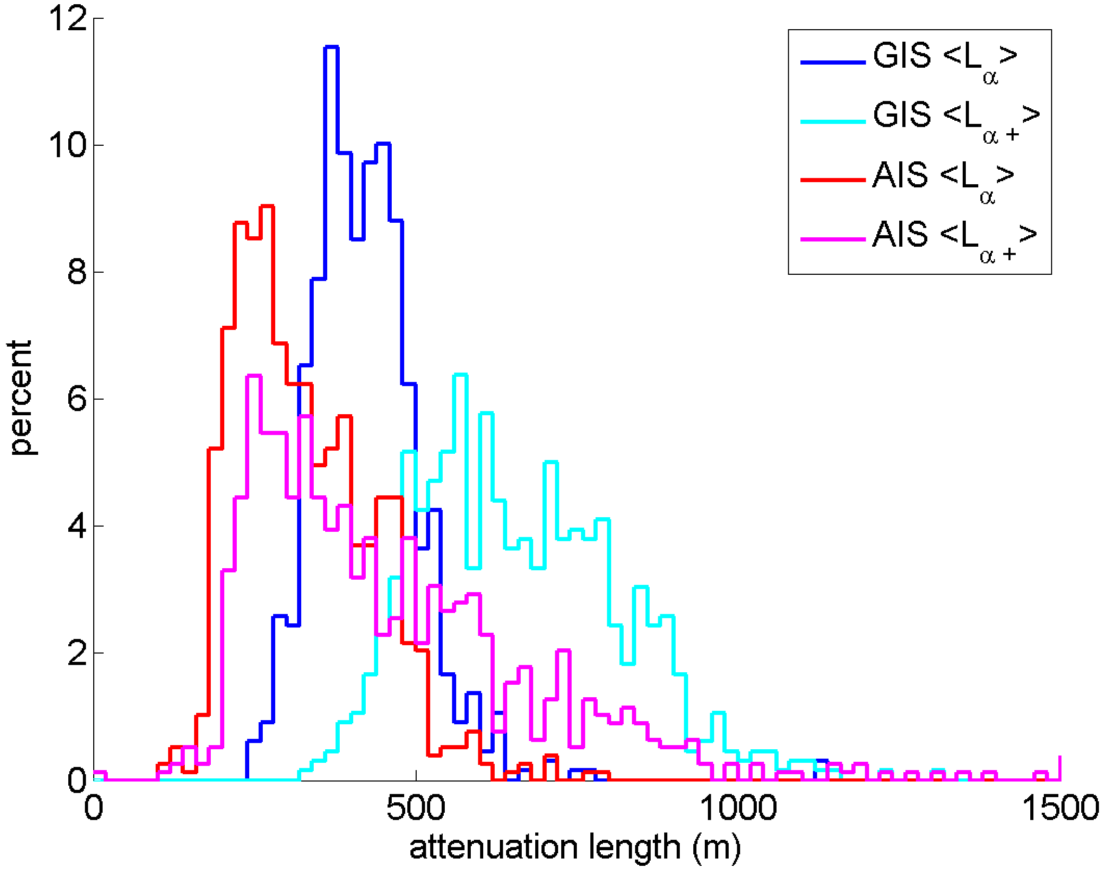

Figure 4.22: Depth-averaged, $< L_\alpha >$, and top-half only, $< L_{\alpha+} >$, average attenuation length values from surface-bottom method for the Greenland and Antarctic Ice Sheets.

4.6.3 AIS and GIS Comparison

It is of interest to directly compare the typical attenuation lengths we determine for Antarctica vs. Greenland. Both follow the trend of longer attenuation lengths for interior rather than coastal ice, as would be expected from the generally warmer ice temperatures toward the coasts. The distribution of these attenuation lengths are shown in Figure 4.22. That the distributions seem to imply Greenland having longer attenuation lengths than Antarctica is somewhat misleading, as Figs. 4.17 and 4.20 show that the majority of the Greenland data comes from the colder interior ice while the majority of the Antarctica data comes from the warmer coastal ice.

It should be noted that of greatest importance to ANITA is the attenuation length of the ice in view of the payload over its flight path, which is mostly the colder interior ice with longer attenuation lengths.

Bottom depth vs. depth-averaged and top-half only average attenuation length values are shown in Figures 4.23 and 4.24, respectively. These figures show the ice in the GIS and AIS give comparable attenuation values with respect to bottom depth.

4.7 Scaling

While the above results show good agreement qualitatively with results from [48] for the GIS, they are systematically about 30% smaller (more pessimistic in the case of neutrino detection). This could possibly be due largely to the correction of ice focusing, if that was not included in the estimates presented in [48]. Similarly, if the difference between correcting for ice focusing is included, there is good agreement between the above results and [46] near Summit, Greenland. Their value of depth averaged attenuation length at 75 MHz is 947^{+92}_{-85} m. If that value is subject to a full focusing correction it would become 802^{+78}_{-72} m (assuming the errors scale linearly). In [46] they use a frequency scaling of the attenuation length equal to -0.55 m/MHz. This would bring their “de-focused” attenuation length value to 736^{+72}_{-66} m at 195 MHz (again, assuming linear scaling of the uncertainty).

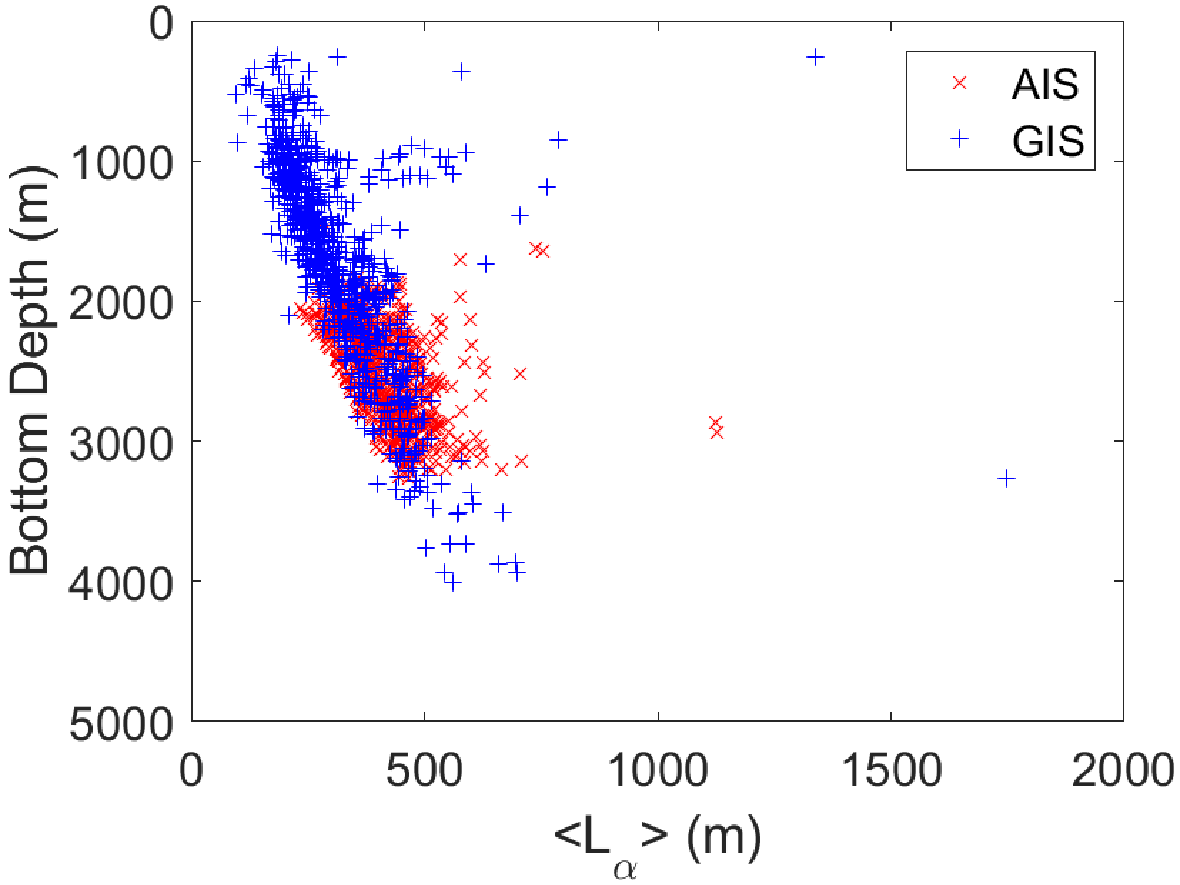

Figure 4.23: Bottom depth versus depth-averaged attenuation length values obtained from the surface-bottom method for the Antarctic and Greenlandic Ice Sheets.

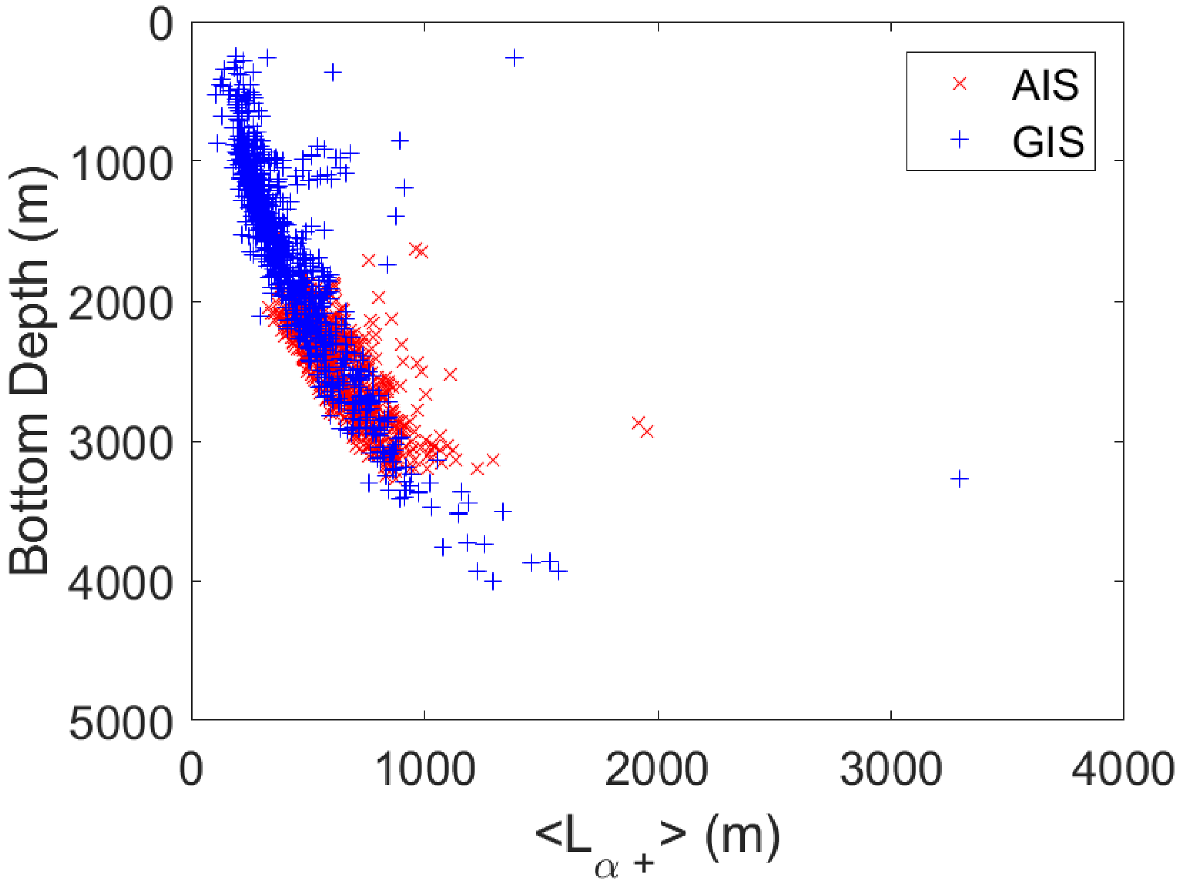

Figure 4.24: Bottom depth versus top-half only average attenuation length values obtained from the surface-bottom method for the Antarctic and Greenlandic Ice Sheets. The scaling for top-half only values has a more pronounced effect on deeper ice.

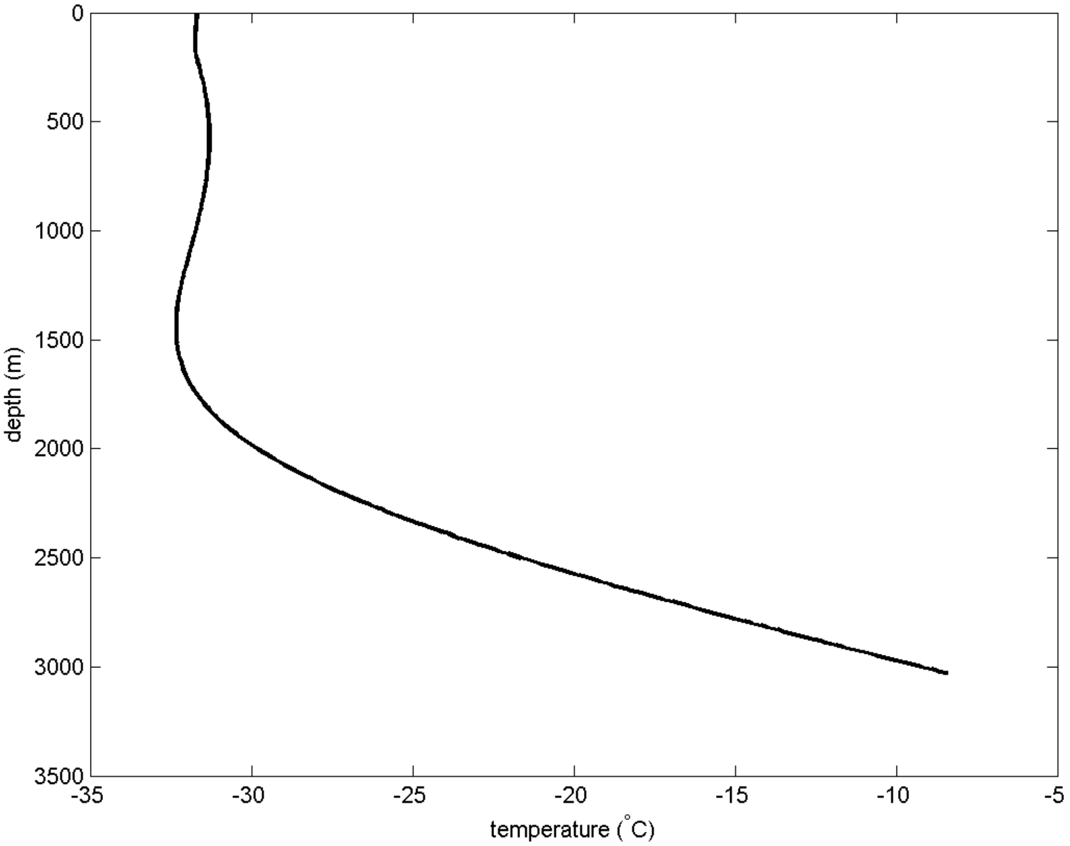

Figure 4.25: Temperature profile as measured by the GReenland Ice-core Project (GRIP) displaying a near-isothermal top-half of the ice. [62]

4.7.1 Upper Half Estimates

A value that is of interest beyond the depth-averaged attenuation length is the average attenuation length in the top-half of the ice only. As this is the volume of ice that has the highest attenuation lengths and is geometrically favorable for the incoming neutrino events, the top-half only estimate may give a better characteristic value to use when determining effective detector volume (and therefore expected detected event rate). To obtain a top-half only estimate, some depth dependence must be invoked. As temperature is the greatest influence on the attenuation, the scaling will be done with respect to temperature. Figure 4.25 shows the temperature profile obtained by the GRIP group, which displays a nearly isothermal temperature profile for approximately the top half of the ice. While this is not a temperature profile characteristic that is common for all polar ice, it is not uncommon for deep ice. Chapter 9 of the text by Cuffey and Paterson demonstrates this [63] for some AIS temperature profiles, MacGregor et al. shows this for a few GIS temperature profiles [48].

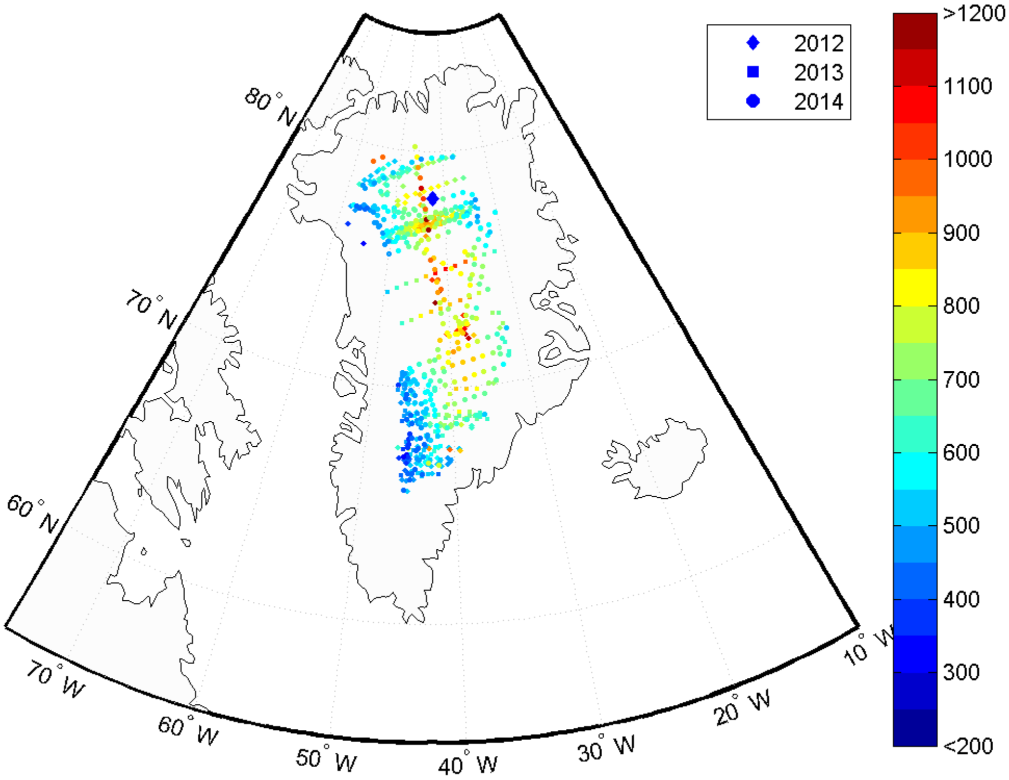

Figure 4.26: Summary of Greenland attenuation lengths derived from direct ratio of measured surface return strength to bedrock return strength (scaled by (4.7)).

If an isothermal top-half with a GRIP-like bottom-half temperature profile is specified and the boundary condition that the attenuation integrated over the profile is equal to the total attenuation estimated by comparing the surface and basal returns is imposed, then the relationship between the full depth-averaged attenuation length, $< L_\alpha >$, and the average attenuation length for the top-half only, $< L_{\alpha+} >$, can be derived to be (by requiring that the integrated total attenuation, using the depth-averaged attenuation length, equals the total attenuation, using the known dependence of attenuation length on temperature):

$$< L_{\alpha+} > = \left(0.0015891c^4 + 0.012571c^3 + 0.074377c^2 + 0.33408c + 1.4198\right) \times < L_\alpha >, \quad (4.7)$$

where $c = \frac{d-2050}{1130.2}$ and d is the bottom depth in meters. For typical interior ice depths (3000m) $< L_{\alpha+} > \approx 1.7 < L_{\alpha} >$. Figures 4.26 and 4.27 show the previous results scaled by (4.7).

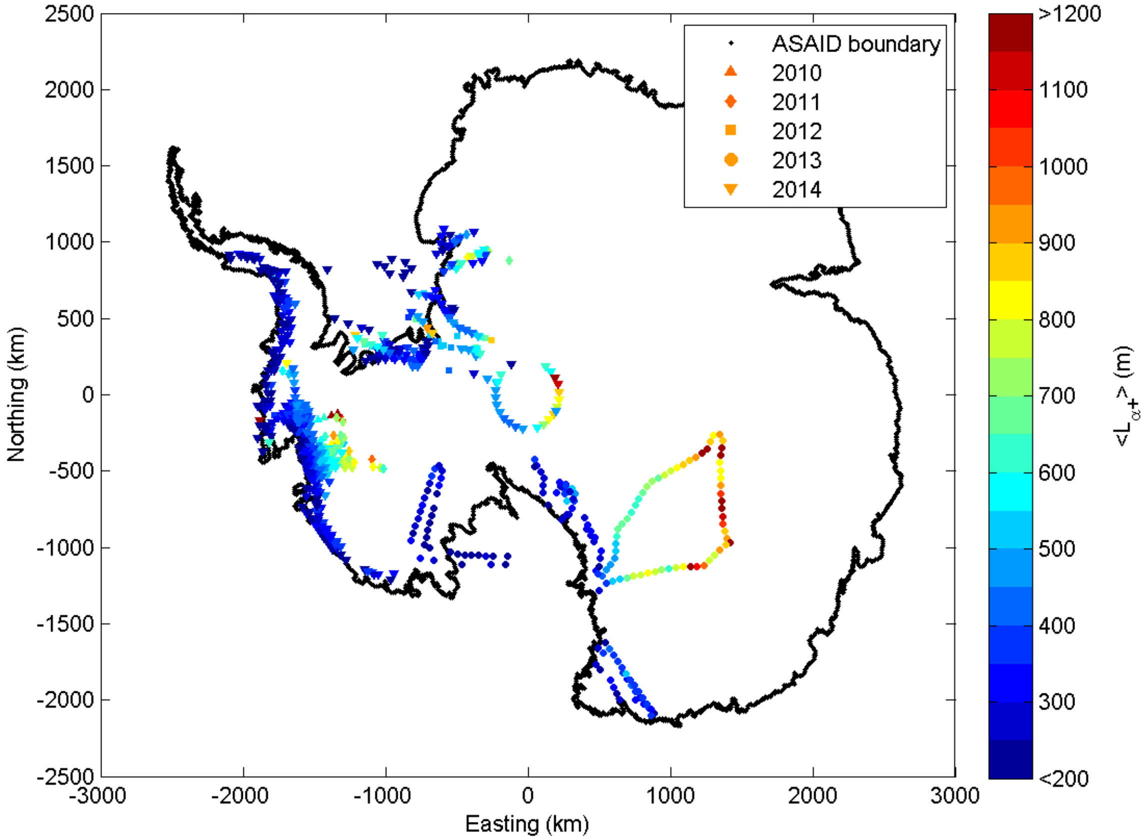

Figure 4.27: Summary of Antarctic attenuation lengths derived from direct ratio of measured surface return strength to bedrock return strength (scaled by (4.7)).

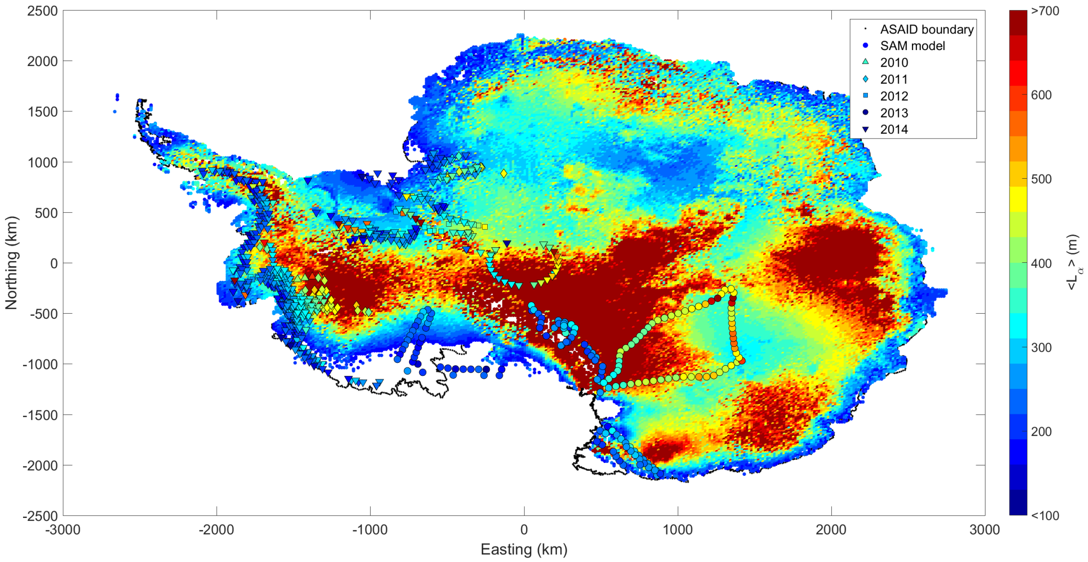

Figure 4.28: Summary of Antarctic attenuation lengths derived from direct ratio of measured surface return strength to bedrock return strength (in black outlines) and values predicted by the SAM model (scaled by $\frac{1}{1.38}$).

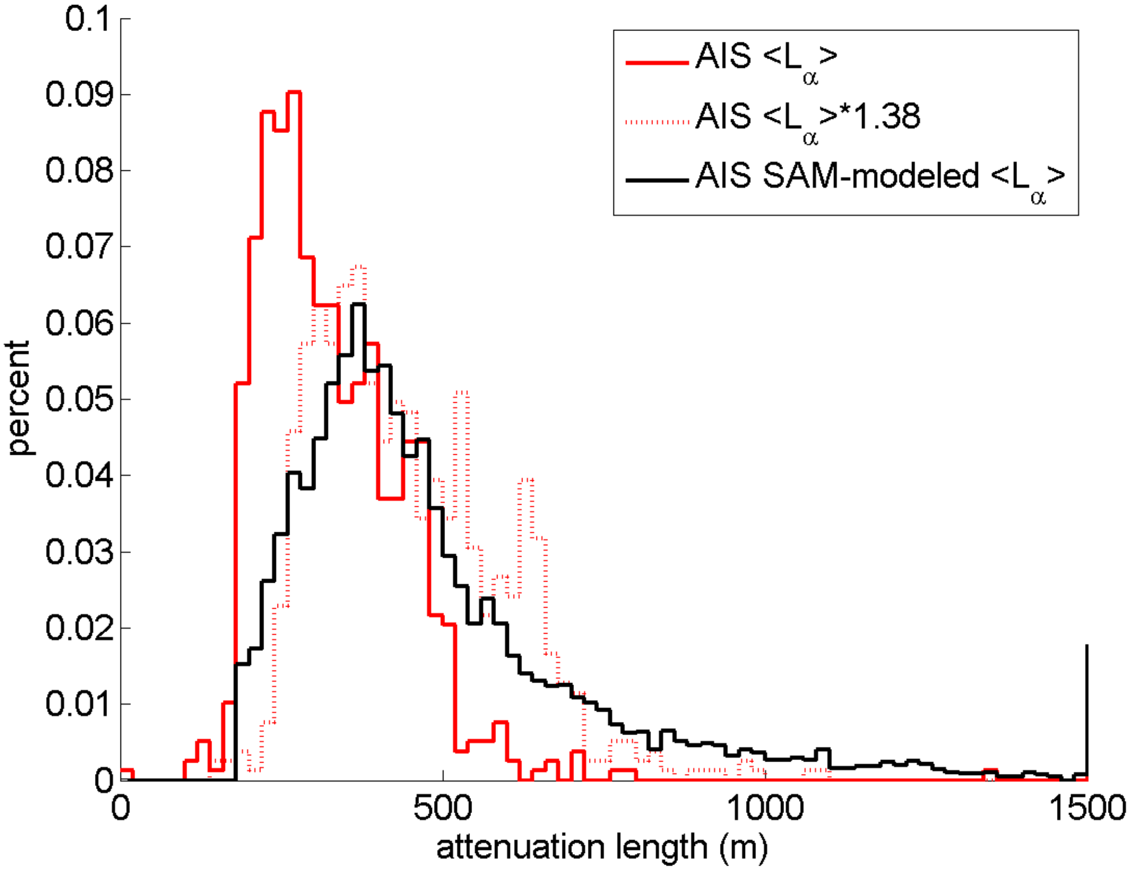

Figure 4.29: Attenuation length values from surface-bottom method and SAM model.

4.7.2 Scaling for SAM Agreement

The SADE ANITA Monte Carlo (SAM), developed by Amir Javaid and detailed in [20], is the most complete ice model available for ANITA to use in Monte Carlo simulations. The values obtained for SAM come from kriging (weighted interpolation) temperature and ice chemistry values from tens of measurements to the whole continent. Figure 4.29 shows the distribution of the attenuation length values from SAM and those from the surface-bottom method detailed above.

If one assumes that, despite differences in location, both of these distributions are meant to represent the same parent distribution a scaling factor can be introduced to compare spatial agreement. Scaling the surface-bottom attenuation length by a factor of 1.38 brings the peaks of the two distributions into better overlap. Scaling the SAM attenuation length values down by the same factor results in the map shown in Figure 4.28.

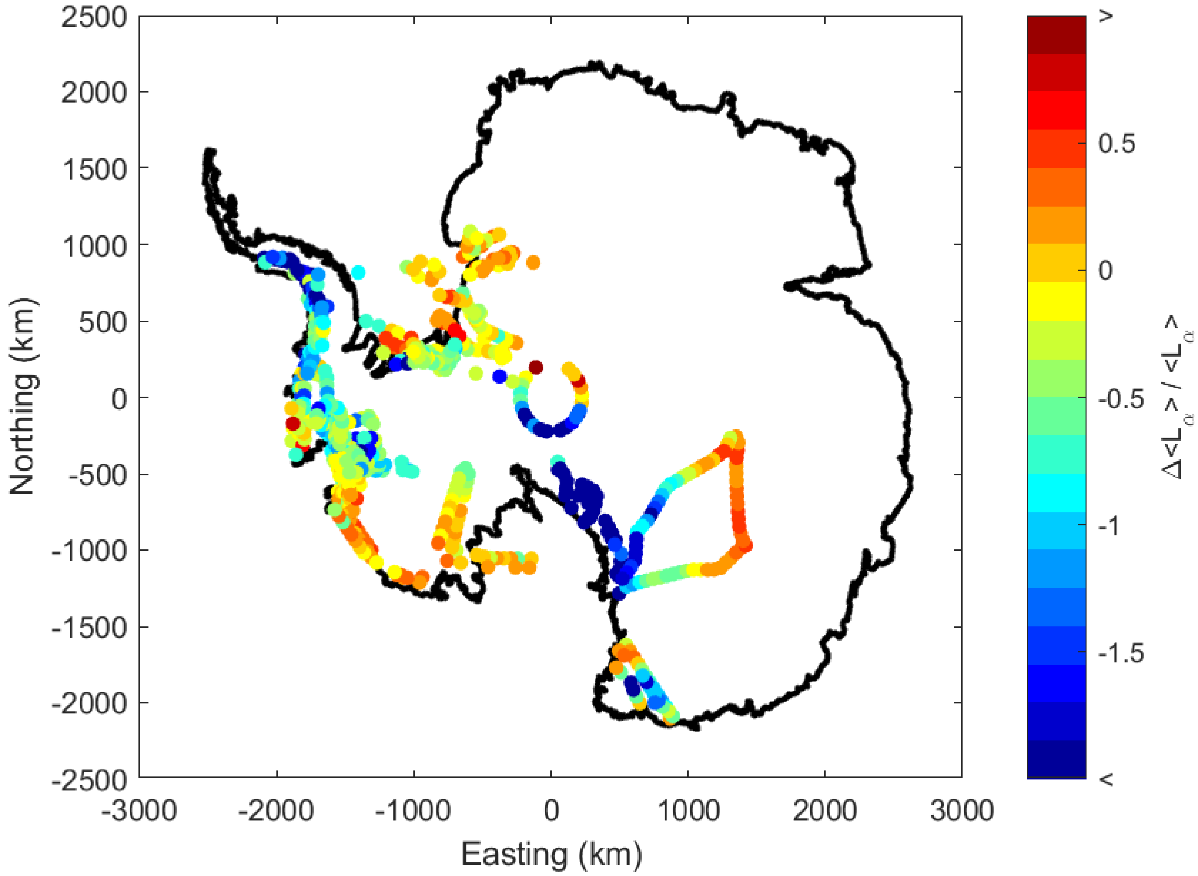

Figure 4.30: Fractional differences of SAM model and surface-bottom method depth-averaged attenuation length by location.

There are several areas with varying attenuation values that are in agreement, but the area between the Ross Sea and the South Pole is noticeably dissonant. Some of this area is within the Transantarctic Mountain Range, which may cause problems for both the surface-bottom method and kriging. The areas in East Antarctica near Terre Adelie (grid Southeast) and Wilhelm II Land (grid East) where there are rapidly changing SAM-predicted values would be ideal places to compare values if/when CReSIS takes data in those areas. Each location that has an estimated depth-averaged attenuation length obtained from the surface-bottom method can be directly compared to the SAM attenuation length value at the nearest gridpoint. The fractional differences of the SAM model and the surface-bottom attenuation length values are shown in Figure 4.30, with a histogram of these differences shown in Figure 4.31. It is worth noting that this is an asymmetric distribution and the surface-bottom attenuation length values are smaller than the SAM values more often than the reverse.

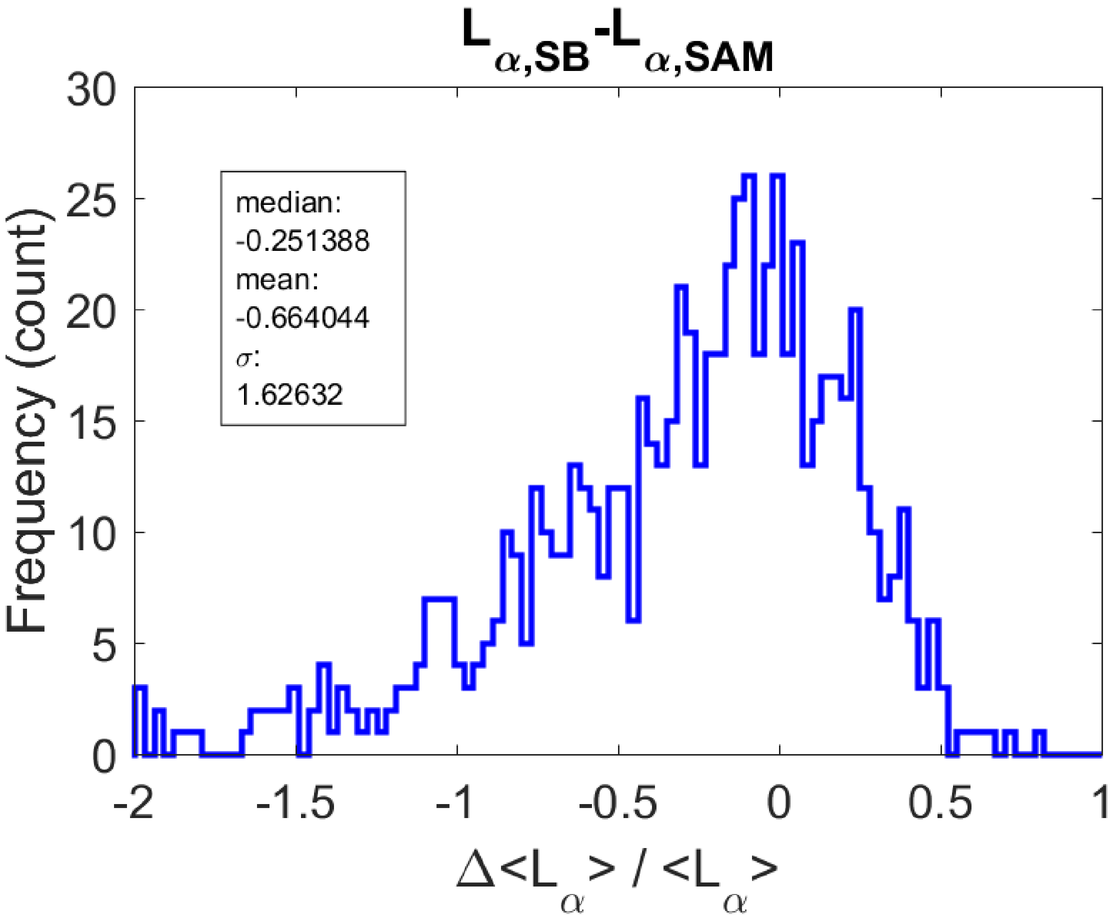

Figure 4.31: Histogram of the fractional differences of SAM model and surface-bottom method depth-averaged attenuation length. The SAM model gives longer attenuation length values than the surface-bottom method in most cases.

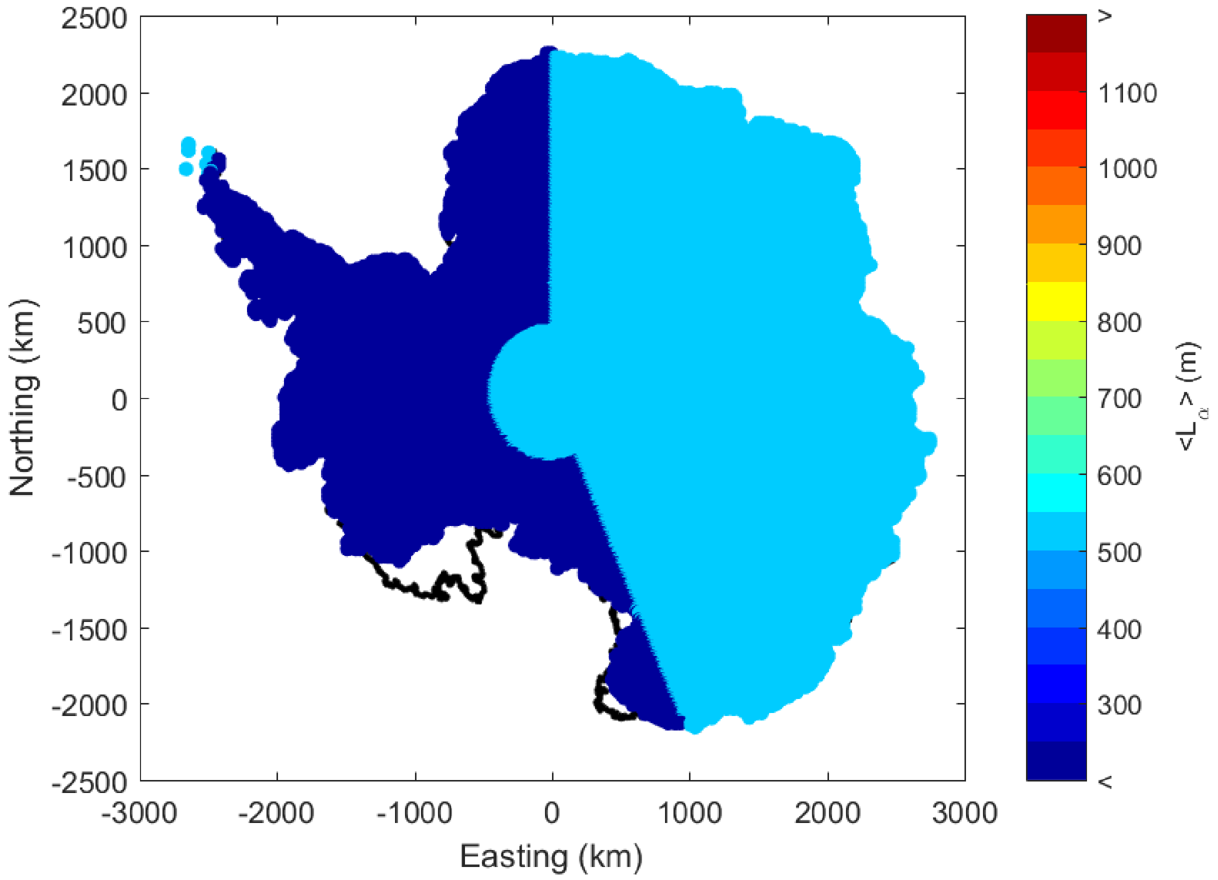

Figure 4.32: The depth-averaged attenuation values used by the ANITA monte carlo, IceMC. The full monte carlo uses 3 different profiles (the small difference between profiles over the Ross and Ronne ice shelves and West Antarctica is ignored here) and scales them to the local depth.

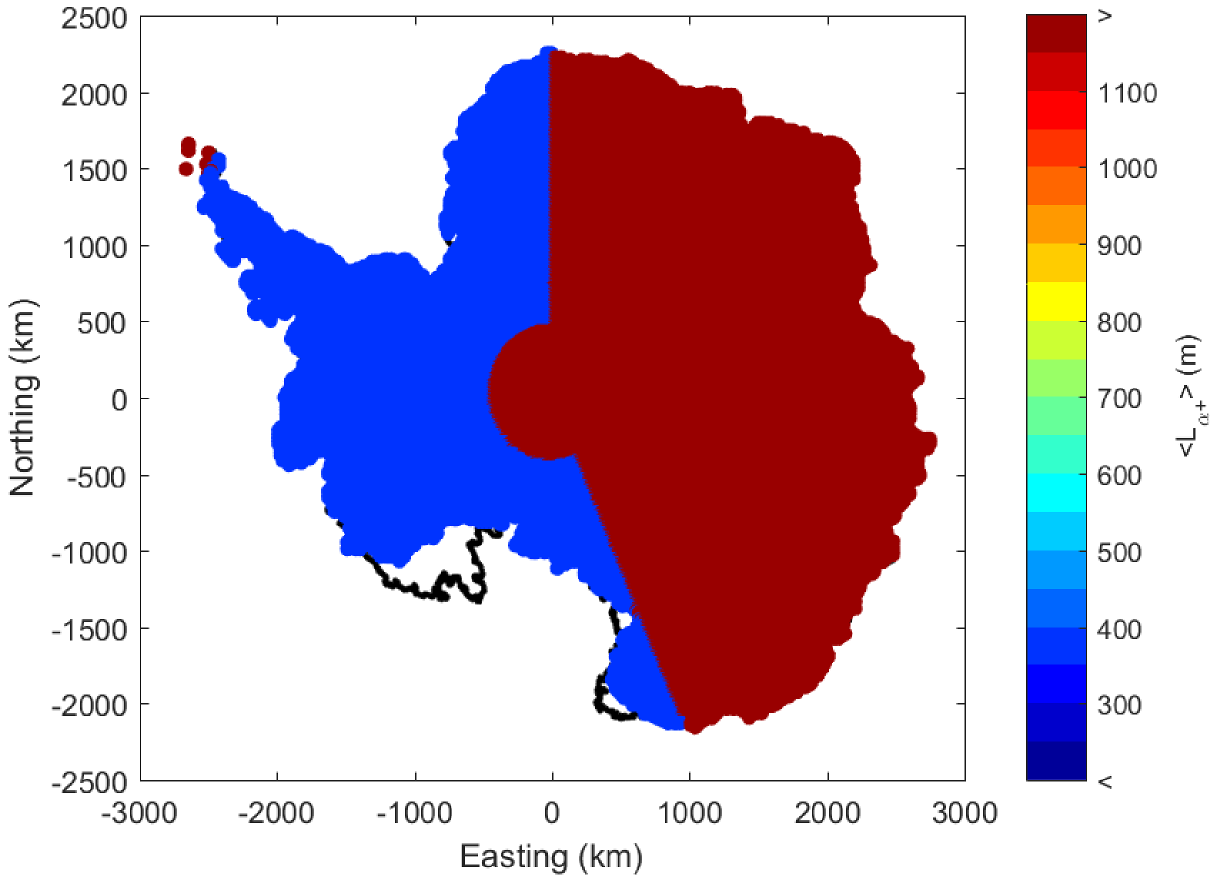

Figure 4.33: The top-half only attenuation values used by the ANITA monte carlo, IceMC. The full monte carlo uses 3 different profiles (the small difference between profiles over the Ross and Ronne ice shelves and West Antarctica is ignored here).

4.7.3 Comparison with IceMC

The monte carlo that ANITA uses to model its effectiveness is called IceMC. Currently IceMC uses an East Antarctica attenuation profile based on measurements from the South Pole and a West Antarctica attenuation profile based on measurements from the Ross Ice Shelf (scaled slightly between shelf ice and West Antarctic sheet ice, but treated as equal in this work). The profiles are stretched or shrunk to accomodate for differing bottom depths but they have equal depth-averaged values across the areas shown in Figure 4.32. The top-half only values produced by these profiles are likewise uniform and shown in Figure 4.33. These values can be compared in the same way as the surface-bottom values were compared to the SAM values in Section 4.7.2. A map of the fractional differences in attenuation length and a histogram of those values are shown in Figures 4.34 and 4.35.

The apparent trends are that the coastal, and especially the Western Antarctic coast, have the largest disparity with IceMC consistently using values of attenuation length shorter than what are supported by the surface-bottom method measurements. Near the pole and in East Antarctica the attenuation lengths used by IceMC are typically longer than those derived from the surface-bottom measurements. Overall, most of the fractional differences are within a factor of 2 one way or the other ($\sigma \approx .34$[unitless]) and, on average, IceMC is 5-10% pessimistic (in terms of favorable attenuation for a large detector volume) compared to the surface-bottom method measurements.

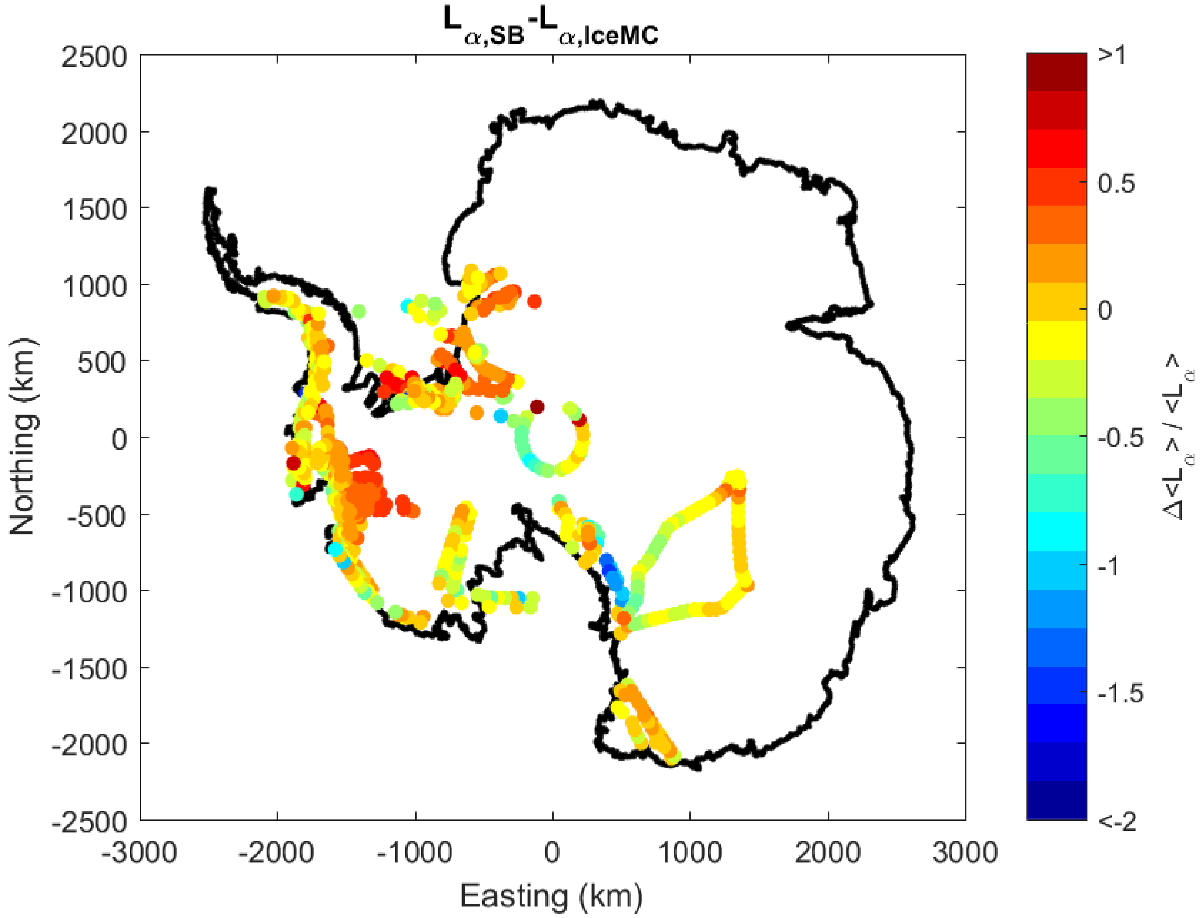

Figure 4.34: Map of the fractional differences in depth-averaged attenuation length between surface-bottom method measurements and values from IceMC.

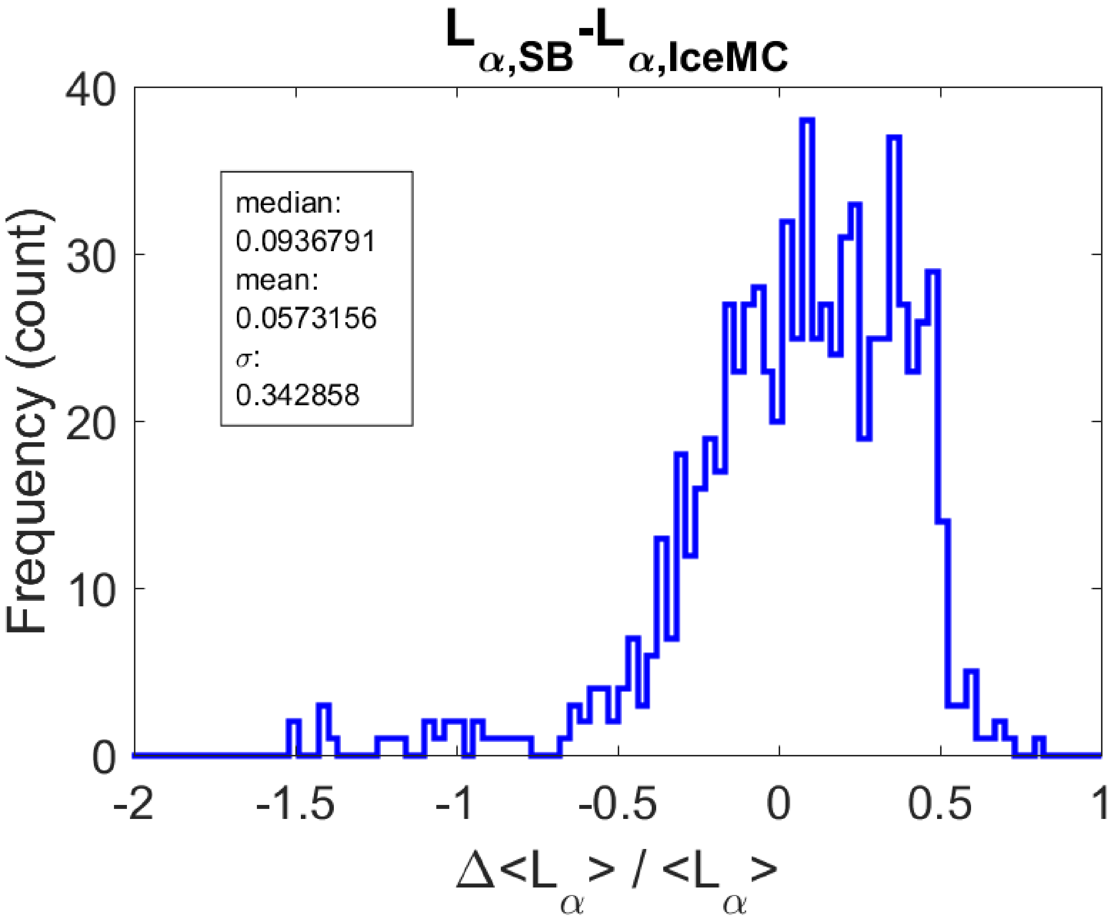

Figure 4.35: Histogram of the fractional differences in depth-averaged attenuation length between surface-bottom method measurements and values from IceMC.

4.7.3.1 Effective Volume Estimate

The ultimate goal is to develop a more nuanced, location-dependent attenuation model of the AIS for use by IceMC (and other radio experiments). However it is important to test the accuracy of the current ANITA model as well. One metric to test is the effective volume, which would directly impact the expected flux estimates of neutrinos and the corresponding limits when there are no observations.

A full attenuation model would have to be implemented into IceMC itself and run with all of the physics simulations to determine the exact effect that different attenuation values would have on the effective volume. However, a simpler test can be made to see how large of an effect this is expected to be. A signal of unit amplitude is allowed to originate anywhere in the AIS volume. For the first case, it travels to the surface at the Cherenkov angle ($\sin^{-1}\left(\frac{1}{n}\right) = \sin^{-1}\left(\frac{1}{\sqrt{3.15}}\right) = 55.7^\circ$) through the IceMC attenuation length profile. For the second case, it travels to the surface at a 55.7° angle through a comparison profile. The power of the received signal at the surface can be compared for these two cases to see what effect the attenuation length profile has on detector volume compared to the IceMC attenuation length profile.

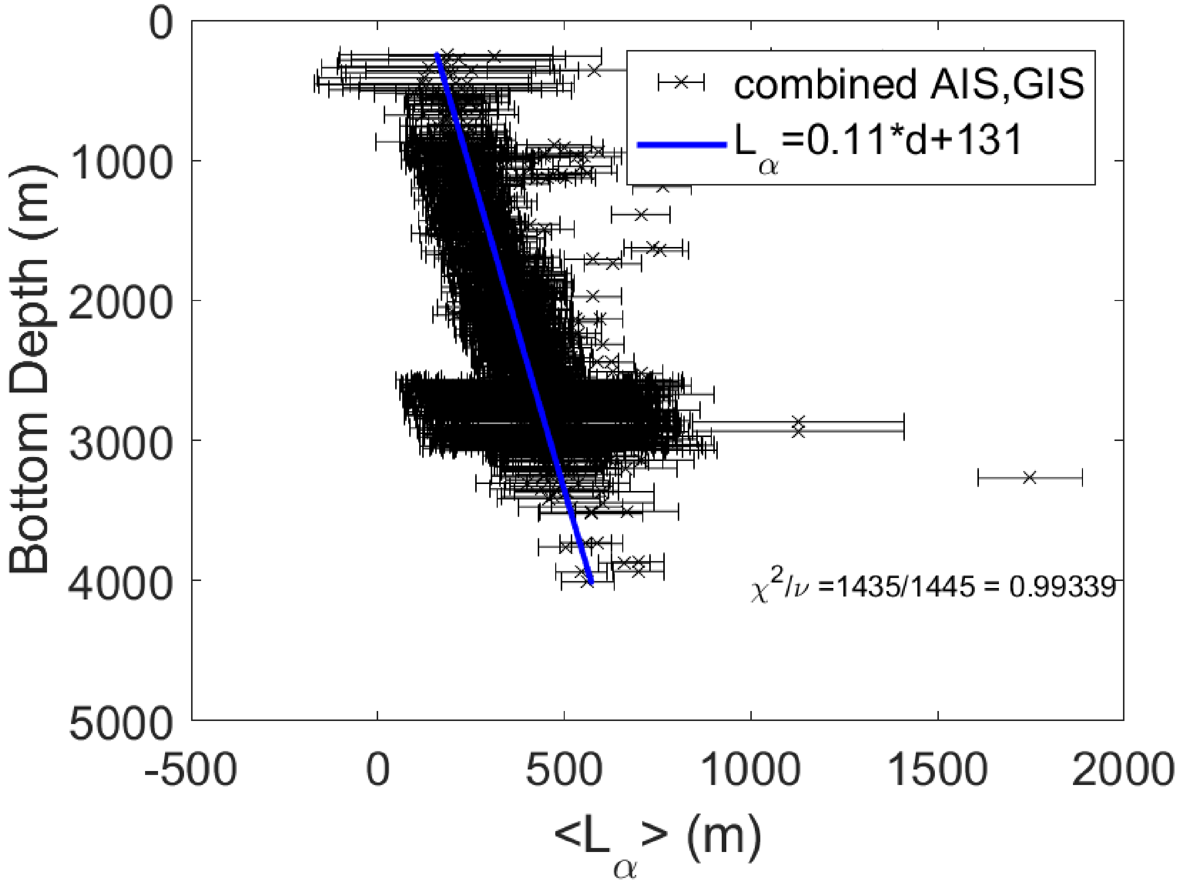

Figure 4.36: Depth-averaged attenuation length values for the GIS and AIS vs. bottom depth. Error bars are the combined systematic errors discussed in Section 4.6.2 and the statistical error present in 500m interval bins in bottom depth. Fit is the minimized χ^2 fit.

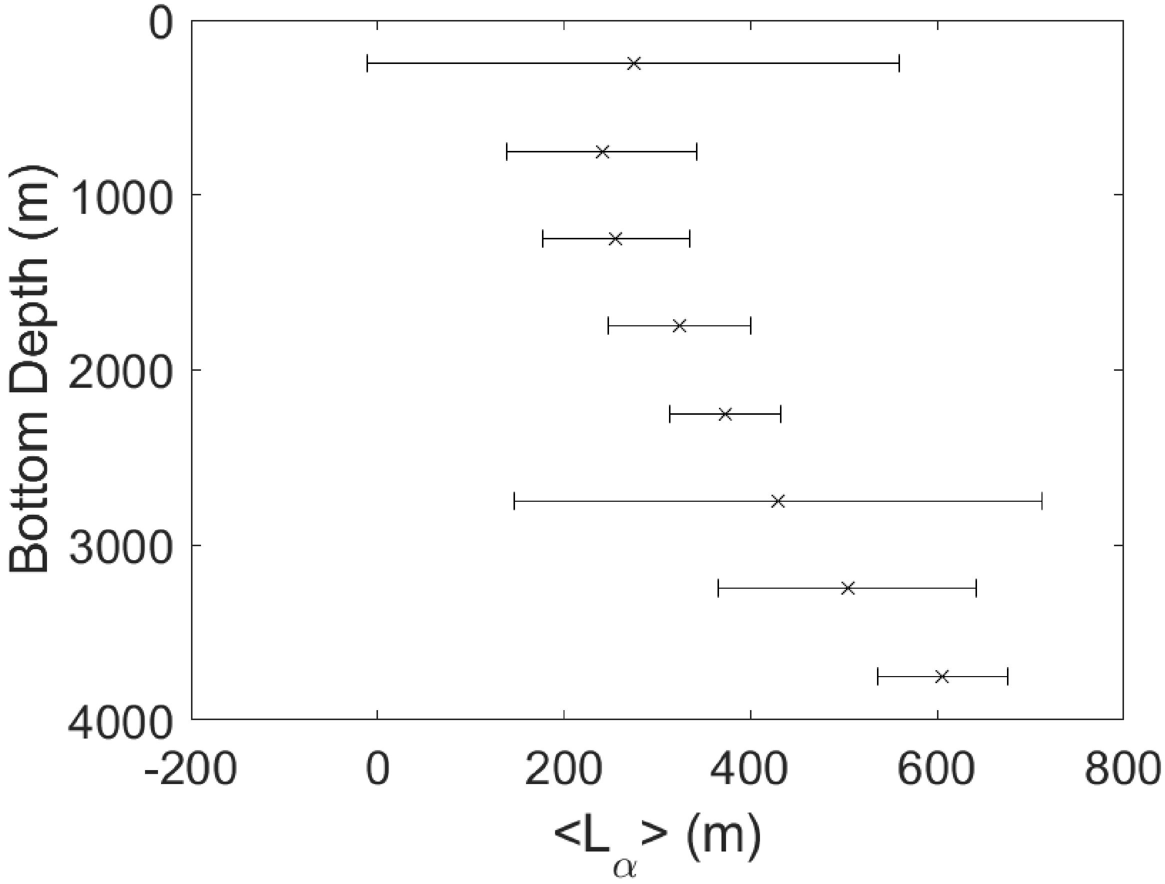

Figure 4.37: Vertically binned average depth-averaged attenuation length values for the GIS and AIS versus bottom depth. Error bars are the combined systematic errors discussed in Section 4.6.2 and the statistical error present in 500m interval bins in bottom depth.

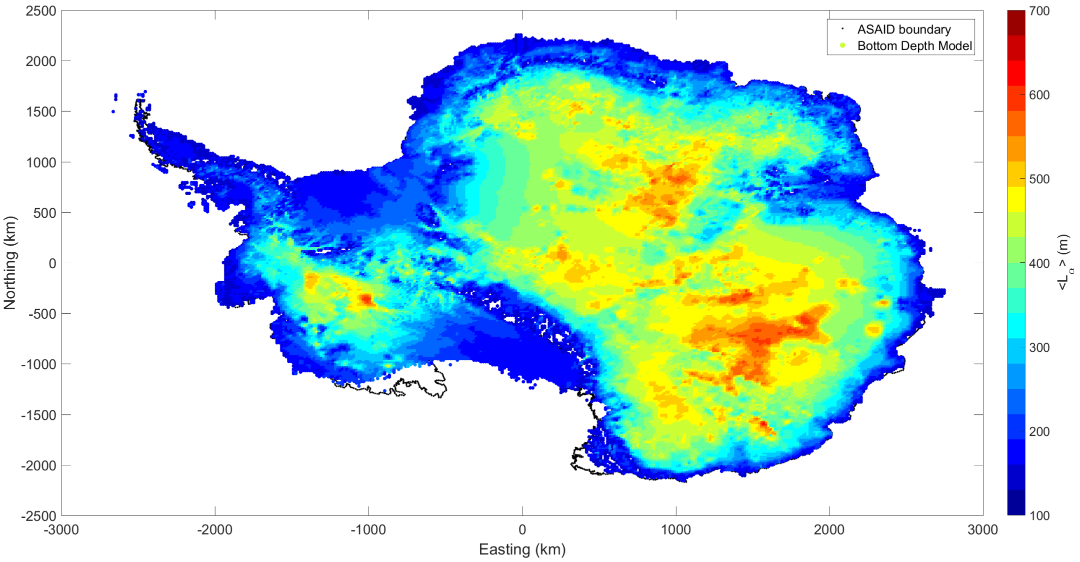

Figure 4.38: Surface-Bottom Model. The values of attenuation length are a function of local bottom depth only, using the empirical equation $< L_\alpha >= 0.11 d_{bottom} + 131$ from the fit in Fig. 4.36.

This, of course, requires new modeled values for all of the AIS. By fitting a line to the scatter plot of $< L_\alpha >$ versus bottom depth we obtained a model informed by the surface-bottom method measurements that can be extended to the entire AIS (see Figures 4.36 and 4.38). The error in each attenuation length value is a quadratic sum of the error determined in Section 4.6.2.3 with a statistical error calculated on groupings of the attenuation length binned in 500m increments of bottom depth values, as shown in Figure 4.37. The linear fit to the data with these errors gives a $\frac{\chi^2}{\nu}$ value of $\frac{1435}{1445} \approx 1$, indicating a good fit. Figures 4.39 and 4.40 show what the top-half only values would be based on a GRIP-like temperature profile and a South Pole-like temperature profile, respectively.

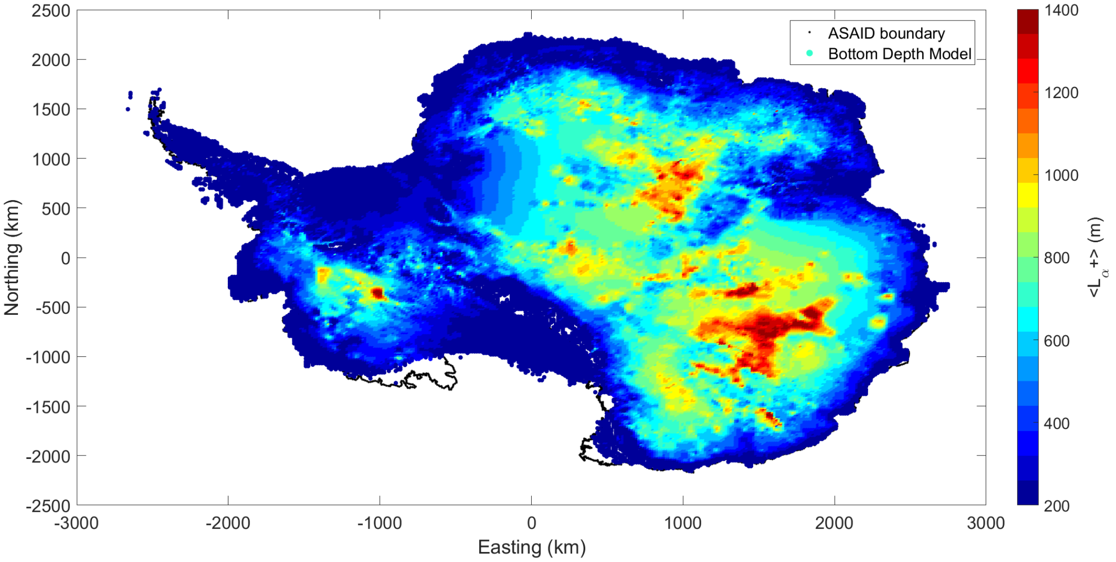

Figure 4.39: Surface-Bottom Model. The values of upper-half attenuation length are a function of local bottom depth only, using the empirical equation $< L_\alpha >= 0.11 d_{bottom} + 131$ from the fit in Fig. 4.36. This value is then put in equation 4.7 to obtain a top-half only attenuation length (assuming a GRIP-like temperature profile).

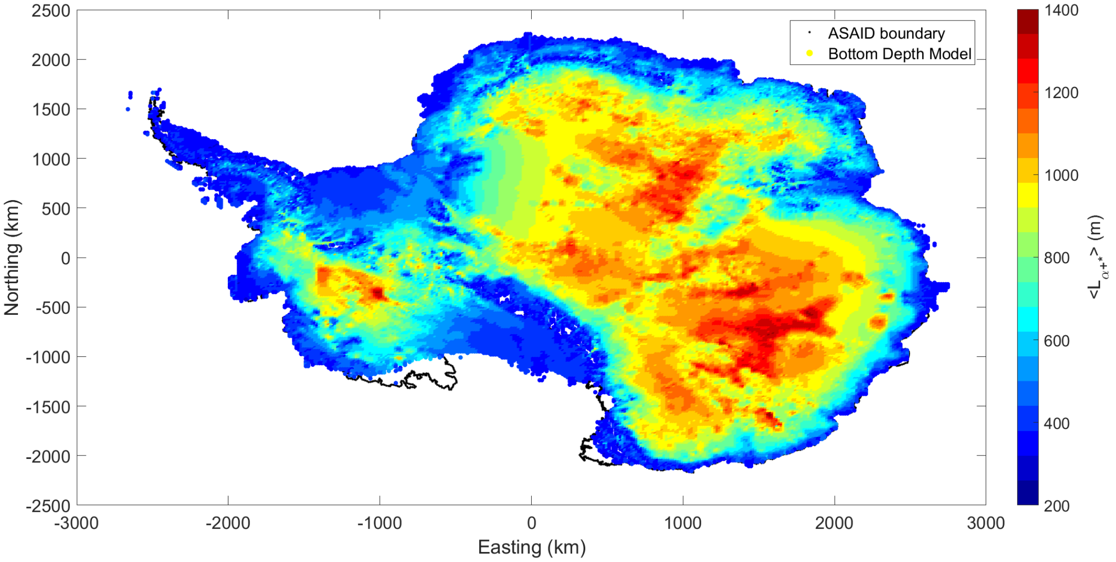

Figure 4.40: Surface-Bottom Model. The values of upper-half attenuation length are a function of local bottom depth only, using the empirical equation $< L_\alpha >= 0.11 d_{bottom} + 131$ from the fit in Fig. 4.36. This value is then scaled by a factor of 2.25 to obtain a top-half only attenuation length (assuming a South-Pole-like temperature profile).

As before, the values can be compared between the two models as in Section 4.7.2. This

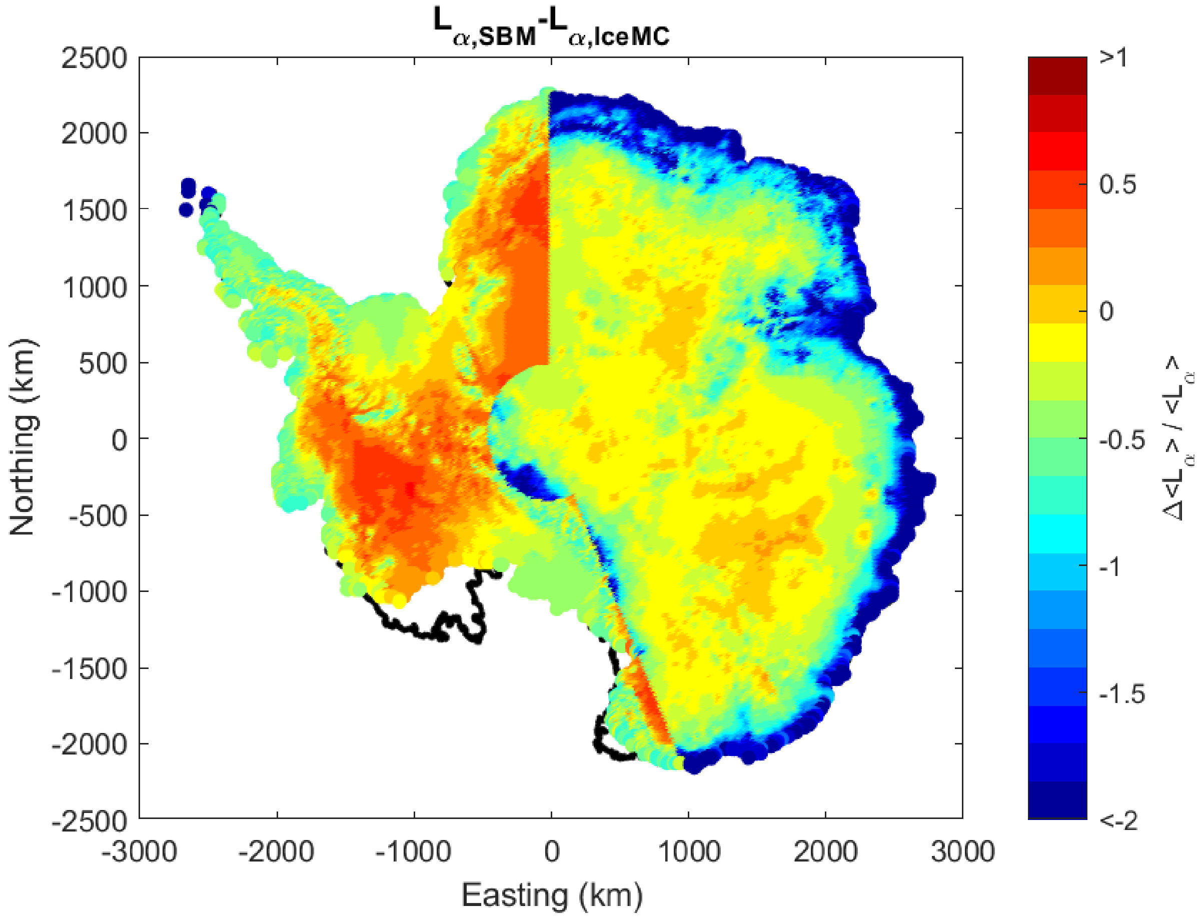

Figure 4.41: Map of the fractional differences in depth-averaged attenuation length between Surface-Bottom Model values and values from IceMC.

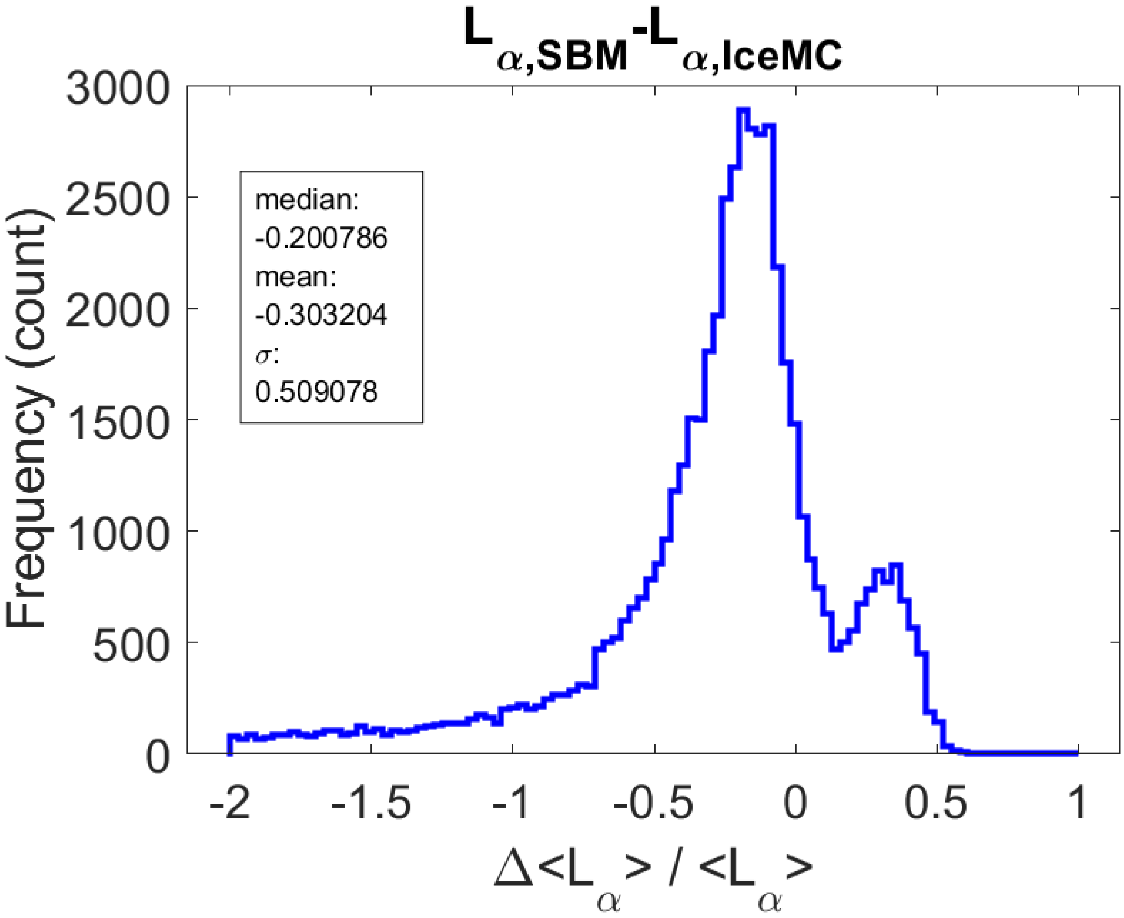

Figure 4.42: Histogram of the fractional differences in depth-averaged attenuation length between Surface-Bottom Model values and values from IceMC.

comparison is illustrated by the map of franctional differences in Figure 4.41 and a histogram of those values in Figure 4.42, respectively. It can be seen in the histogram that there are two strong populations of values present representing the two attenuation profiles that IceMC implements. The larger peak at ~ -0.2 is due to the IceMC values accross East Antarctica being relatively optimistic compared to the Surface-Bottom Model values, while the smaller peak at ~ 0.3 is due to the IceMC values across West Antarctica being relatively pessimistic compared to the Surface-Bottom Model values.

If the shape of the IceMC attenuation length profile is preserved but it is constrained to have the depth-averaged attenuation length value determined by the Surface-Bottom Model a direct comparison of the relative power at the ice surface from a signal originating in the surface can

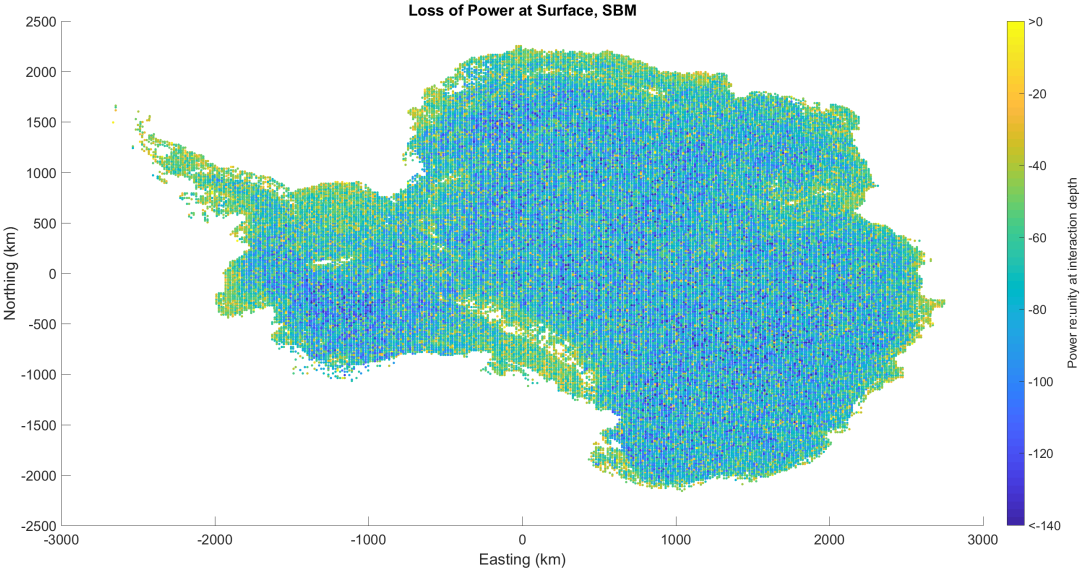

Figure 4.43: Map of the monte carlo results of the power loss from a unit signal generated within the ice to the surface propagated through a scaled IceMC attenuation length profile constrained to have a depth-averaged attenuation length equal to the value derived by the Surface-Bottom Model.

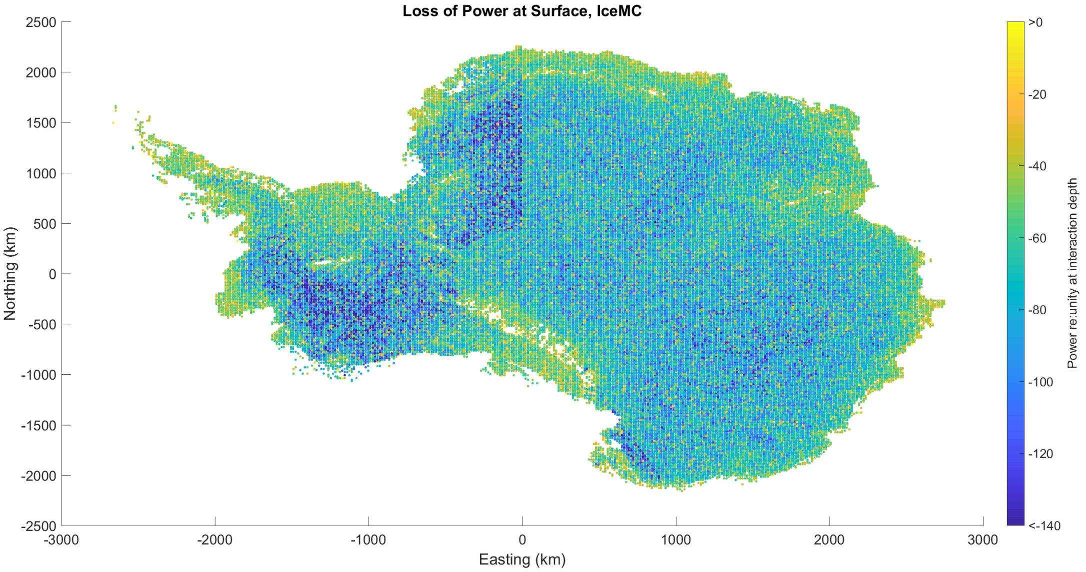

Figure 4.44: Map of the monte carlo results of the power loss from a unit signal generated within the ice to the surface propagated through the IceMC attenuation length profile.

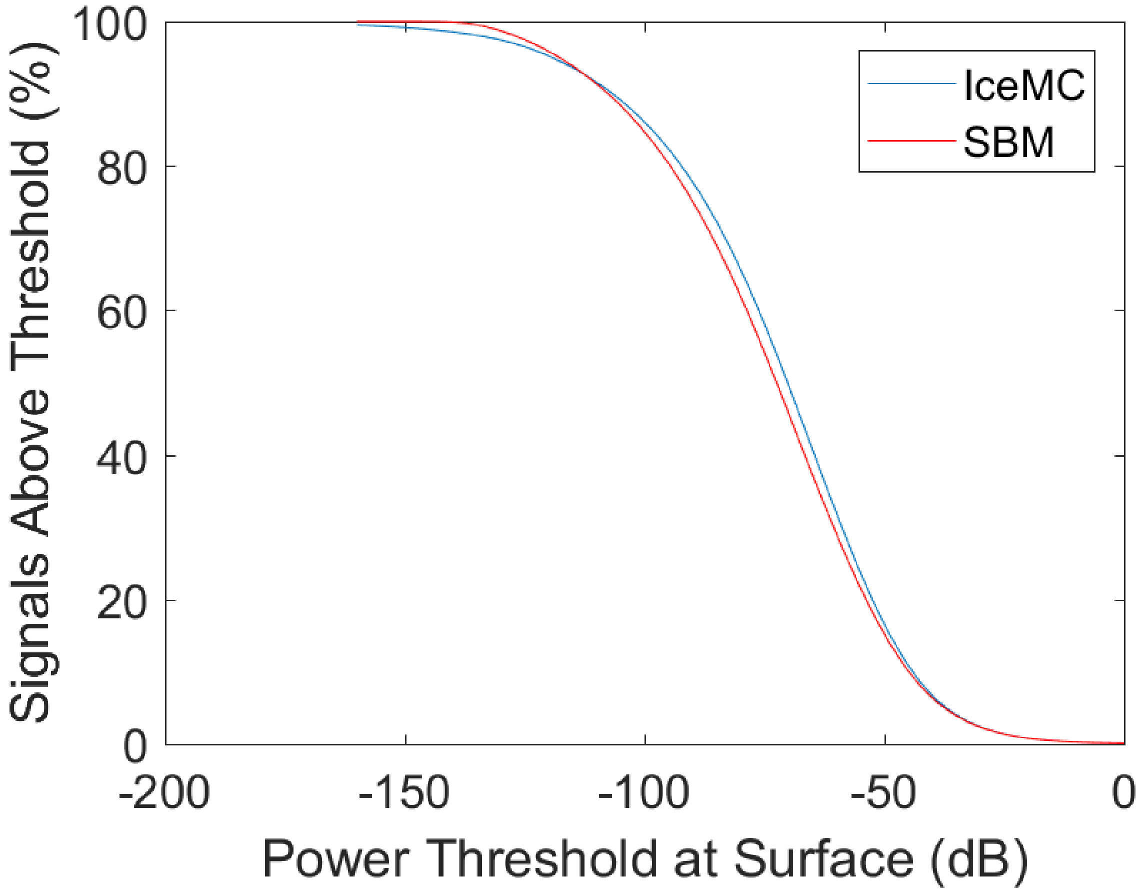

Figure 4.45: Percentage of monte carlo generated signals above a given threshold at the surface after propagating through the IceMC attenuation length profile (blue) and the Surface-Bottom Model-scaled attenuation length profile (red). On average, assuming a propagation distance to ANITA of 200km, both of these signals would be further reduced by 43dB before entering the ANITA DAQ.

be made. Figures 4.43 and 4.44 show this for the Surface-Bottom Model scaled profiles and the IceMC profiles for one million events, respectively. Figure 4.45 shows the percentage of events above a given threshold at the surface for the two attenuation length models and Figure 4.46 is the histogram of all of these values.

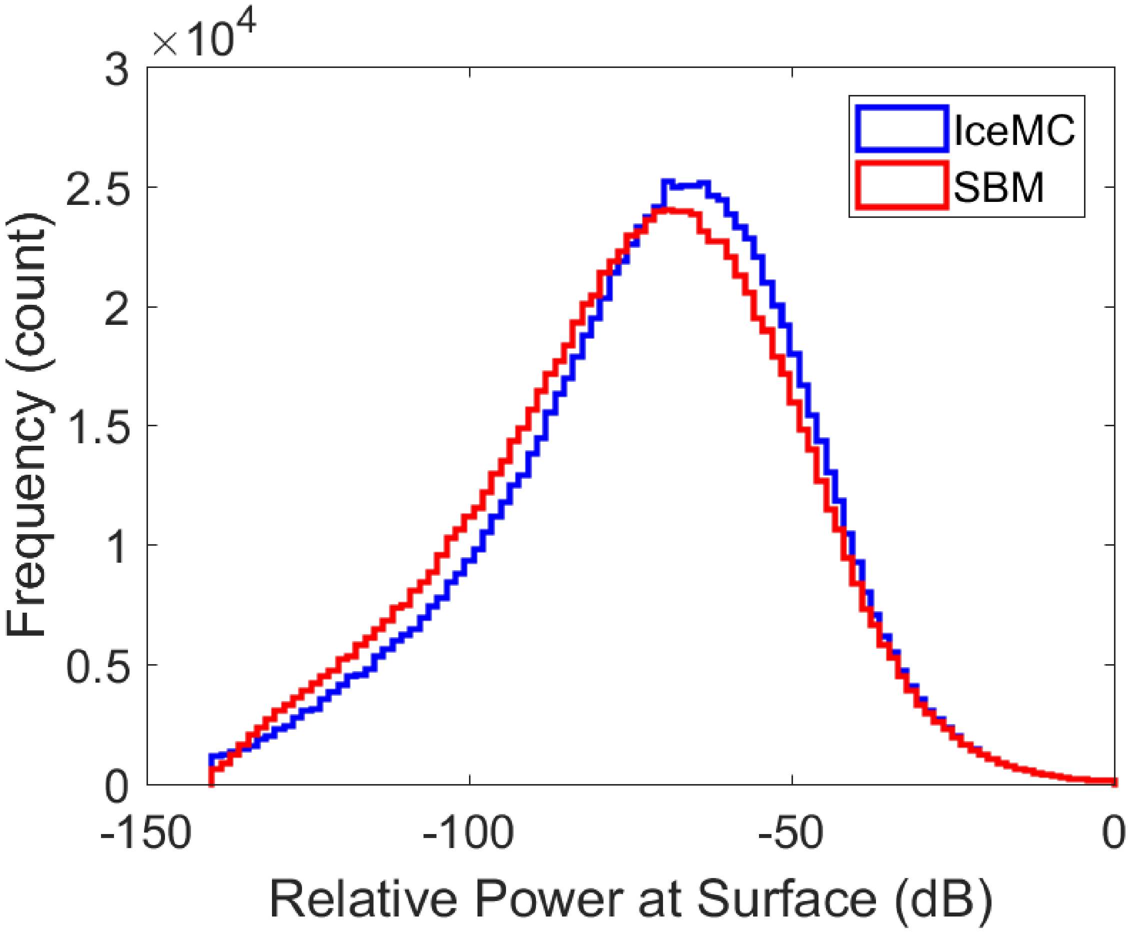

Figure 4.46: Histogram of the relative power at the surface for monte carlo generated signals that propagate through the IceMC attenuation length profile (blue) and the Surface-Bottom Model-scaled attenuation length profile (red). On average, assuming a propagation distance to ANITA of 200km, both of these signals would be further reduced by 43dB before entering the ANITA DAQ.

It is clear that from the differences of power at the surface from the two attenuation length profiles (map in Fig. 4.47, histogram of values in Fig. 4.48) that even though the overall threshold distribution looks similar there is a tradeoff in relatively less effective volume in East Antarctica and relatively more effective volume in West Antarctica when scaling to conform to Surface-Bottom modeled values. The histogram of the difference in surface power values (Fig. 4.48) suggests that there is a possible 15-20% effect in the signal amplitude at the surface.

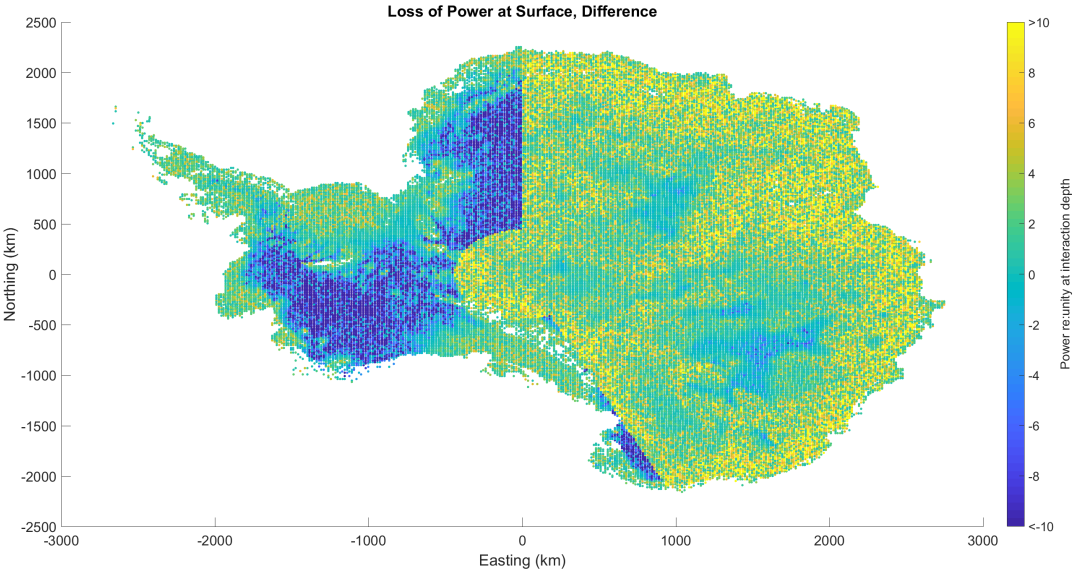

Figure 4.47: Map of the difference in the relative power at the surface for monte carlo generated signals that propagate through the IceMC attenuation length profile and the Surface-Bottom Model-scaled attenuation length profile.

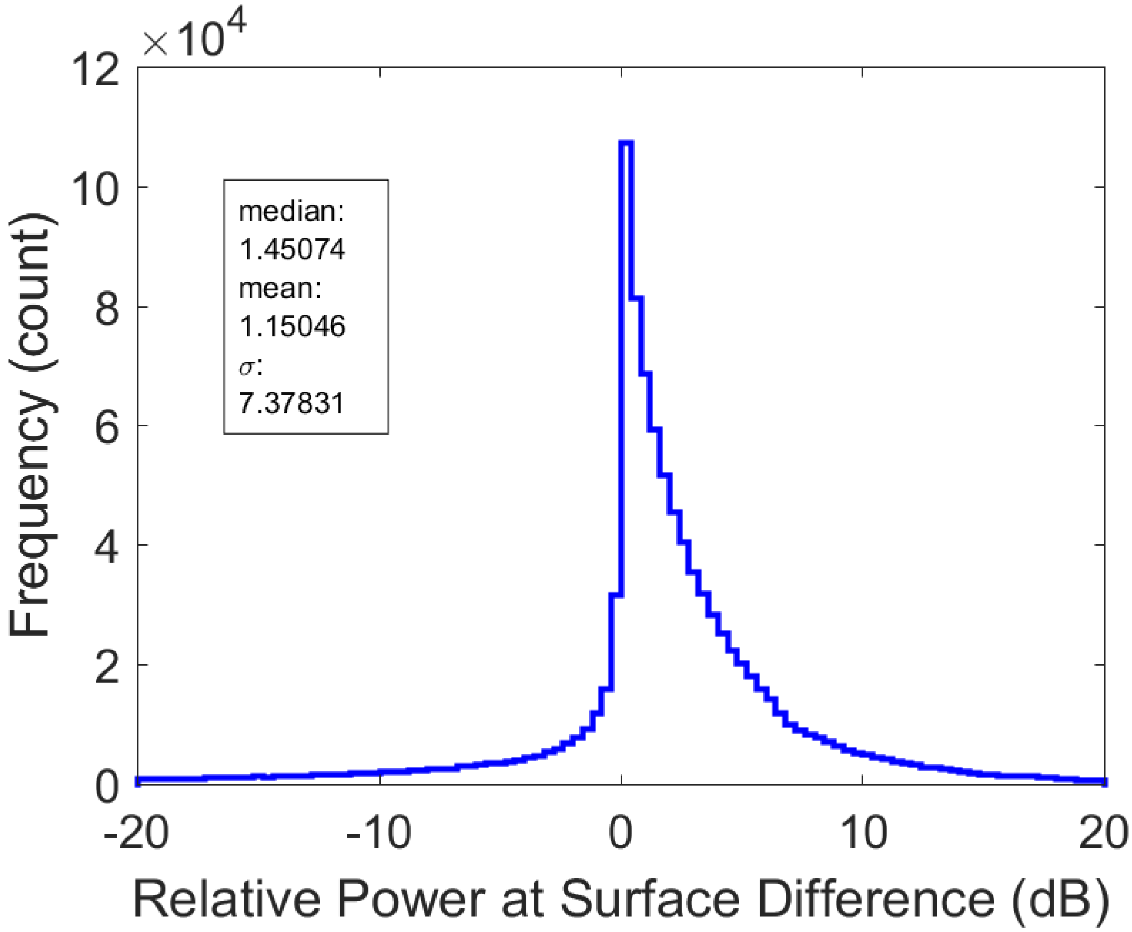

Figure 4.48: Histogram of the difference in the relative power at the surface for monte carlo generated signals that propagate through the IceMC attenuation length profile and the Surface-Bottom Model-scaled attenuation length profile. The large positive peak is largely due to the relative boost in attenuation length that IceMC gives East Antarctica.

4.8 Conclusions and Discussion

Quantitatively, we find the following:

1. For the first time using direct radar measurement the assumed attenuation length dependence on temperature/depth has been verified (Section 4.5). Assuming that the underlying reflection mechanism is uniform through the upper 2/3 of the ice sheet, we have verified the expected temperature-dependent reduction of the attenuation length as a function of depth into Greenland at the Summit site, lending credence to measurements which build this de-

pendence into their models [48].

Numerically, we obtain a depth-averaged attenuation length of 500^{+90}_{-60} m based on the depth-dependent method at Summit, in agreement with the value of 546 ± 23 m obtained using the ratio of surface to bedrock return strengths, and also consistent with Summit measurements (albeit at 75 MHz, and with no focusing correction of the type we apply here, see Section 4.7) [46], and measurements made by comparing the reflectivity of internal layers. We find excellent agreement between our derived values and those of Winebrenner *et al.* [64] in the vicinity of WAIS. In general, our values for the field attenuation length are approximately 30% smaller than values obtained using the relative strengths of internal layer reflections as done by MacGregor *et al*. [48] (note that the method described in that paper is not the same as used in this chapter for the depth-dependent attenuation length estimate). Additionally, whereas that prior measurement has uncertainties that are typically of order 5%, we find systematic errors that are typically a factor of two to four times larger. Note that reflections due to internal layers, prior to the bed reflection, are counted as 'losses' and therefore are implicit in our quoted attenuation length.

2. As expected, given the temperature profiles, we observe longer average field attenuation lengths for the interior ice, compared to the coast, for both polar ice regions.

3. Assuming a temperature profile similar to GRIP (Figure 4.25), the top-half only average attenuation can be estimated. This value perhaps offers a more realistic value to be used when determining detector effective volume. Typically, the top-half only average attenuation length is ≈ 1.7 times larger than the value for depth-averaged attenuation length for the full ice depth.

4. Attenuation values based on the surface-bottom method for Antarctica are generally about 30% lower than those predicted by the SAM model in [20]

5. Comparisons with the ANITA monte carlo, IceMC, indicate that ANITA may currently be overestimating attenuation length in East Antarctica and underestimating it in West Antarc-

tica, with an overall average difference in the signal amplitude reaching the surface of 15-20%. This estimation is given by scaling the current IceMC values to have the same depth-averaged attenuation length as values derived from the surface-bottom CReSIS measurements and incorporated into a simple model based on only the bottom depth. While most of the attenuation happens in the lower, warmer ice, ANITA is more sensitive to shallow angles and is more affected by the attenuation in the upper ice. To obtain upper ice only attenuation values a temperature profile must be applied to the full depth attenuation length value to give it depth-dependence. The upper half only attenuation length values can vary greatly while maintaining the same depth-averaged attenuation length.

CReSIS is currently mapping the ice surface, and the internal ice sheets with improved hardware, sensitive over the range from 150 MHz–18 GHz [36, 65]. Future available data sets should therefore offer improved measurements of ice properties, allowing investigation of the frequency dependence of ice radioglaciology.

4.9 Future Work Prospects

1. Update analysis with new CReSIS data - CReSIS has published a couple of years worth of new data. This data is even more heavily concentrated toward the coasts and is more limited than past years, but would still be worth checking for consistency.

2. Development of surface model based on the results from HiCal, the ANITA solar reflection measurements, photographs, and the satellite data. To test this model the expected NRCS should be produced to compare with Aquarius data.

3. Refinement of upper-half attenuation length estimates, or top-1km attenuation length estimates. ANITA is most sensitive to this ice and the value of attenuation here can vary widely without a large effect on the depth-averaged value. Perhaps the SAM model can be refined so that it is constrained to use measured depth-averaged attenuation length values where

available. The maximum value at the surface should also be constrained to not differ from the expected value based on surface temperature measurements.

4. Reconciliation of attenuation length systematically being lower than other published values for the same or similar locations.

References

[1] Matthew J. Mottram. *A Search for Ultra-high Energy Neutrinos and Cosmic-Rays with ANITA-2*. PhD thesis, University College London, February 2012.

[2] Peter G. Gorham. Radio detection of ultra-high energy cosmic rays and neutrinos. *SLAC Summer Institute on Particle Physics (SSI04)*, pages 2–13, Aug 2004.

[3] Peter G. Gorham. Observation of the askaryan effect in ice. *Phys. Rev. Lett*, 99, 2007.

[4] W. F. Hanlon. *The Energy Spectrum of Ultra High Energy Cosmic Rays Measured By The High Resolution Fly's Eye Observatory in Stereoscopic Mode*. PhD thesis, University of Utah, 2008.

[5] Samridha Kunwar. *Design And Development Of An Autonomous Radar Receiver For The Detection Of Ultra High Energy Cosmic Rays*. PhD thesis, University of Kansas, 2015.

[6] D.S. Barnhill. *Composition Analysis of Ultra High Energy Cosmic Rays Using the Pierre Auger Observatory Surface Detector*. PhD thesis, UCLA, 2005.

[7] Kenneth Greisen. End to the cosmic-ray spectrum? *Phys. Rev. Lett.*, 16:748–750, Apr 1966. doi: 10.1103/PhysRevLett.16.748. URL `https://link.aps.org/doi/10.1103/PhysRevLett.16.748`.

[8] G. T. Zatsepin and V. A. Kuzmin. Upper limit of the spectrum of cosmic rays. *JETP Lett.*, 4: 78–80, 1966. [Pisma Zh. Eksp. Teor. Fiz.4,114(1966)].

[9] L. Bergström and A. Goobar. *Cosmology and Particle Astrophysics*. Praxis Publishing Ltd, 2004. ISBN 3-540-43128-4., 2004. doi: 10.1007/3-540-37719-0.

[10] J. W. Cronin. “the highest-energy cosmic rays”. *Nuclear Physics B Proceedings Supplements*, 138:465–491, jan 2005.

[11] Federico Fraschetti. On the acceleration of ultra-high-energy cosmic rays. *Philosophical Transactions of the Royal Society of London A: Mathematical, Physical and Engineering Sciences*, 366(1884):4417–4428, 2008.

[12] W.D. Apel et al. The spectrum of high-energy cosmic rays measured with kascade-grande. *Astroparticle Physics*, 36(1):183 – 194, 2012.

[13] Kumiko Kotera and Angela V. Olinto. The astrophysics of ultrahigh-energy cosmic rays. *Annual Review of Astronomy and Astrophysics*, 49(1):119–153, 2011.

[14] P. Abreu et al. Measurement of the proton-air cross section at $\sqrt{s}$=57 TeV with the pierre auger observatory. *Phys. Rev. Lett.*, 109:062002, Aug 2012.

[15] J. Abraham et al. Measurement of the depth of maximum of extensive air showers above 10^{18} eV. *Phys. Rev. Lett.*, 104:091101, Mar 2010.

[16] R. U. Abbasi et al. Study of ultra-high energy cosmic ray composition using telescope array’s middle drum detector and surface array in hybrid mode. *Astroparticle Physics*, 64:49–62, apr 2015.

[17] J. P. Ralston. Radio surf in polar ice: A new method of ultrahigh energy neutrino detection. *Phys Rev D.*, 71(1):011503, January 2005. doi: 10.1103/PhysRevD.71.011503.

[18] J. Paden et al. “ wideband measurements of ice sheet attenuation and basal scattering”. *IEEE Geoscience and Remote Sensing Letters*, 2, 2005.

[19] J. MacGregor. *Development and Applications of a Radar-Attenuation Model for Polar Ice Sheets*. PhD thesis, University of Washington, 2008.

[20] A. Javaid. *Monte Carlo Simulation for Radio Detection of Ultra-High Energy Air Shower Cores by ANITA-II*. PhD thesis, U. of Delaware, 2012.

[21] J. Paden. *Synthetic Aperture Radar for Imaging the Basal Conditions of the Polar Ice Sheets*. PhD thesis, University of Kansas, August 2006.

[22] F. Rémy and S. Parouty. Antarctic ice sheet and radar altimetry: A review. *Remote Sensing*, 1(4):1212–1239, 2009.

[23] L. Brucker, E. Dinnat, and L. Koenig. *Aquarius L3 Weekly Polar-Gridded Normalized Radar Cross Section, Version 5. 25 August 2011 to 28 May 2015*. NASA National Snow and Ice Data Center Distributed Active Archive Center, Boulder, Colorado USA, 2015. doi: https://doi.org/10.5067/Aquarius/AQ3_NRCS.005. Date Accessed: 2015.

[24] C. Matzler and U. Wegmuller. Dielectric properties of freshwater ice at microwave frequencies. *Journal of Physics D Applied Physics*, 20:1623–1630, dec 1987.

[25] S Fujita, T Matsuoka, T Ishida, K Matsuoka, and S Mae. *A summary of the complex dielectric permittivity of ice in the megahertz range and its application for radar sounding of polar ice sheets, Physics of Ice Core Records, ed. T. Hondoh*. Hokkaido University Press, Sapporo, 2000.

[26] J. A. MacGregor, D. P. Winebrenner, H. Conway, K. Matsuoka, P. A. Mayewski, and G. D. Clow. Modeling englacial radar attenuation at siple dome, west antarctica, using ice chemistry and temperature data. *J. Geophys. Res*, 112, 2007.

[27] John W. Clough. Radio-echo sounding: Reflections from internal layers in ice sheets. *Journal of Glaciology*, 18:3–14, 01 1977.

[28] G de Q. Robin, S Evans, and J T. Bailey. Interpretation of radio echo sounding in polar ice sheets. *Philosophical Transactions of The Royal Society A: Mathematical, Physical and Engineering Sciences*, 265:437–505, 12 1969.

[29] C H. Harrison. Radio echo sounding of horizontal layers in ice. *Journal of Glaciology*, 12: 383–397, 01 1973.

[30] J G. Paren and G De Q. Robin. Internal reflections in polar ice sheets. *Journal of Glaciology*, 14:251–259, 01 1975.

[31] L Brekovskikh. *Waves in Layered Media*. Academic Press, 1976.

[32] Gorham P. W. et al. Antarctic surface reflectivity measurements from the anita-3 and hical-1 experiments. *Journal of Astronomical Instrumentation*, 06(02):1740002, 2017.

[33] S. Prohira et al. Antarctic Surface Reflectivity Calculations and Measurements from the ANITA-4 and HiCal-2 Experiments. *ArXiv e-prints*, January 2018.

[34] M. Stockham, J. Macy, and D. Besson. Radio frequency ice dielectric permittivity measurements using cresis data. *Radio Science*, 51(3):194–212, 2016. doi: 10.1002/2015RS005849.

[35] P. Fretwell. 'bedmap 2: improved ice bed, surface and thickness datasets for antarctica". *The Cryosphere*, 7:375–393, 2013.

[36] B. Panzer. et al. *"An ultra-wideband, microwave radar for measuring snow thickness on sea ice and mapping near-surface internal layers in polar firn"*, 59, 2013.

[37] J. Li, J. Paden, C. Leuschen J., F. Rodriguez-Morales, R. Hale, E. Arnold, R. Crowe, D. Gomez-Garcia, and P. Gogineni. Research high-altitude radar measurements of ice thickness over the antarctic and greenland ice sheets as a part of operation ice bridge. *IEEE Transactions on Geoscience and Remote Sensing*, 51(2):742–754, 2012.

[38] E. Rignot, J. Mouginot, and B. Scheuchl. Ice flow of the antarctic ice sheet. *Science*, 333, 2011.

[39] J. Mouginot, B. Scheuchl, and E. Rignot. Mapping of ice motion in antarctica using synthetic-aperture radar data. *Remote Sens*, 4:2753–2767, 2012.

[40] Hugh F. J. Corr and D. G. Vaughn. A recent volcanic eruption beneath the west antarctic ice sheet. *Nature Geoscience*, 1:122–125, 2008.

[41] S. G. Warren. Optical constants of ice from the ultraviolet to the microwave. *Appl. Opt*, 23, 1984.

[42] J. Li. Mapping of ice sheet deep layers and fast outlet glaciers with multi-channel-high-sensitivity radar. Technical report, *CReSIS Technical Report* **145**, 2010.

[43] F. Rodriguez-Morales et al. "advanced multifrequency radar instrumentation for polar research". *IEEE Transactions on Geoscience and Remote Sensing*, 52(5):2824–2842, 2014.

[44] P. Kanagaratnam, P. Gogineni, V. Ramasami, and D. Braaten. A wideband radar for high-resolution mapping of near-surface internal layers in glacial ice. *IEEE Transactions on Geoscience and Remote Sensing*, 42:483–490, 2004.

[45] L. Smith, J. Paden, C. Leuschen, and S. Gogenini. Beamwidth analysis for sar processing of airborne depth-sounder data over ice sheets. *Geoscience and Remote Sensing Symposium (IGARSS)*, 1109:4596–4599, 2010.

[46] J. Avva et al. "an in situ measurement of the radio-frequency attenuation in ice at summit station, greenland". *J. Glac*, 61:1005–1011, 2015.

[47] J. W. Clough. Radio-echo sounding: reflections from internal layers in ice sheets. *Journal of Glaciology*, 18:3–14, 1977. doi: 10.1017/S002214300002147X.

[48] Joseph A. MacGregor et al. Radar attenuation and temperature within the greenland ice sheet. *Journal of Geophysical Research: Earth Surface*, 120(6):983–1008, 2015.

[49] Dave Besson, Ilya Kravchenko, Andres Ramos, and Juliet Remmers. Radio frequency birefringence in south polar ice and implications for neutrino reconstruction. *Astroparticle Physics*, 34, 05 2010.

[50] T. Barrella, S. Barwick, and D. Saltzberg. Ross ice shelf (antarctica) in situ radio-frequency attenuation. *J. Glac*, 57:61–66, 2011.

[51] S. Barwick, D. Besson, P. Gorham, and D. Saltzberg. South polar in situ radio-frequency ice attenuation. *J. Glac*, 51:231–238, 2005.

[52] D. Z. Besson et al. "in situ radioglaciological measurements near taylor dome, antarctica and implications for ultra-high energy (uhe) neutrino astronomy". *Astropart. Phys*, 29:130–157, 2008.

[53] V. V Bogorodsky, C. R. Bentley, and P. E. Gudmandsen. *Radioglaciology*. Riedel, Dordrecht, Holland, 1985.

[54] S. Evans. Dielectric properties of ice and snow – a review. *J. Glac*, 5:773–792, 1965.

[55] S. Fujita, T. Matsuoka, and S. Mae S. Morishima. The measurement on the dielectric properties of ice at hf, vhf and microwave frequencies. *Geoscience and Remote Sensing Symposium, 1993. IGARSS '93*, 1993.

[56] T. Matsuoka, S. Fujita, and S. Mae. Effect of temperature on dielectric properties of ice in the range 5–39 ghz. *J. Appl. Phys*, 80, 1996.

[57] K. Matsuoka, J. A. MacGregor, and F. Pattyn. Predicting radar attenuation within the antarctic ice sheet. *Earth and Planetary Science Letters*, 359:173–183, 2012.

[58] R. Drews, O. Eisen, I. Weikusat, S. Kipfstuhl, A. Lambrecht, D. Steinhage, F. Wilhelms, and H. Miller. Layer disturbances and the radio-echo free zone in ice sheets. *The Cryosphere*, 3: 195–203, 2009.

[59] S. Fujita, T. Matsuoka, T. Ishida, K. Matsuoka, and S. Mae. A summary of the complex dielectric permittivity of ice in the megahertz range and its application for radar sounding of polar ice sheets. In *Physics of Ice Core Records*, pages 185–212. T. Hondoh, Hokkaido University Press, Sapporo, 2000.

[60] J. Paren. Reflection coefficient at a dielectric interface. *J. Glac*, 27:203–204, 1981.

[61] D. Z. Besson et al. “antarctic radio frequency albedo and implications for cosmic ray reconstruction”. *Radio Sci.*, 50, 2015.

[62] Sigfus J. Johnsen, Dorthe Dahl-Jensen, Willi Dansgaard, and Niels Gundestrup. Greenland palaeotemperatures derived from grip bore hole temperature and ice core isotope profiles. *Tellus B: Chemical and Physical Meteorology*, 47(5):624–629, 1995. doi: 10.3402/tellusb.v47i5.16077.

[63] W. S. B. Paterson K. M. Cuffey. *The Physics of Glaciers, ed. 4*. Elsevier, Burlington, MA, 2010.

[64] D. P. Winebrenner, B. E. Smith, G. A. Catania, H. B. Conway, and C. F. Raymond. Radio-frequency attenuation beneath siple dome, west antarctica, from wide-angle and profiling radar observations. *Ann. Glaciol*, 37:226–232, 2003.

[65] J. McDaniel. Design, integration, and miniaturization of a multichannel ultra-wideband snow radar receiver and passive microwave components. Technical report, CReSIS Technical Report, no. 161, Lawrence, KS, University of Kansas, pp. 113, 2015.

[66] Yetang Wang and Shugui Hou. A new interpolation method for antarctic surface temperature. *Progress in Natural Science*, 19(12):1843 – 1849, 2009.

Appendix A

Surface Reflection - Additional Figures

These are additional figures related to the Aquarius-based satellite reflection analysis as described in Chap. 3.

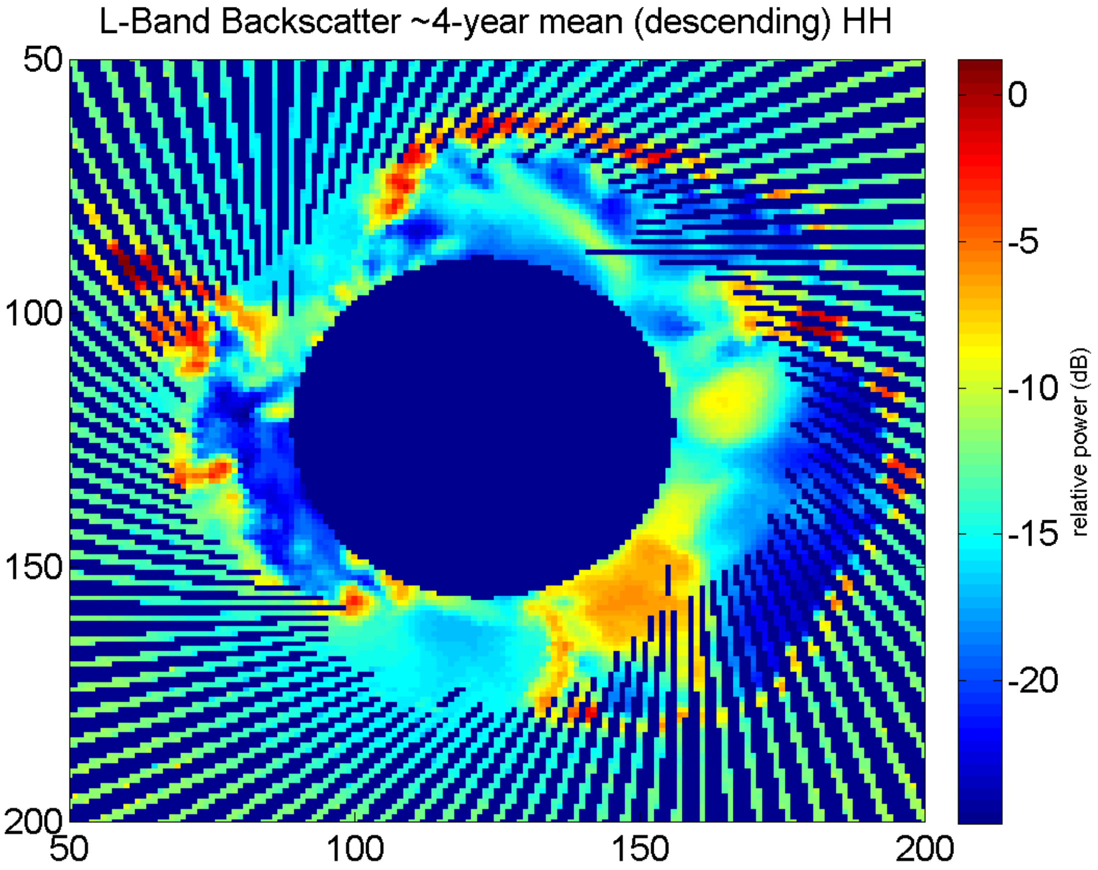

Figure A.1: The ~ 4 year weekly mean values of NRCS in the H-pol transmit, H-pol receive configuration on descending orbit. The x- and y-axis values are 36km grid numbers.

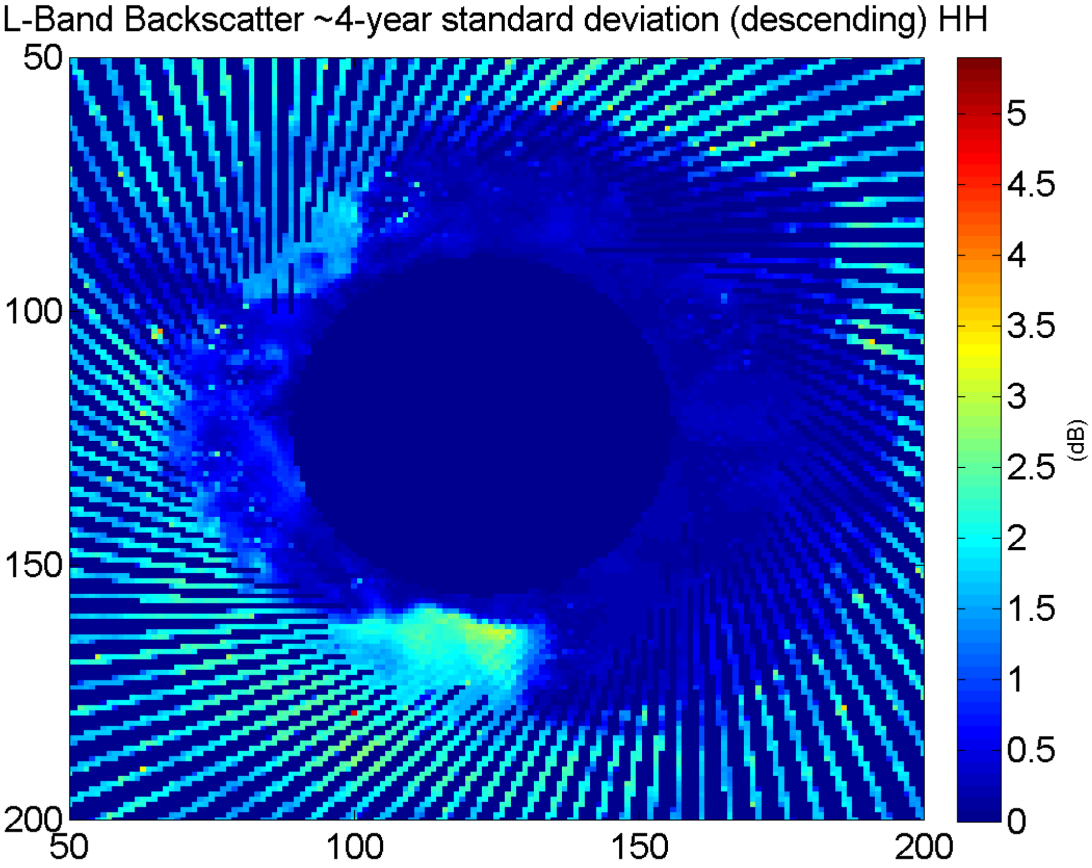

Figure A.2: The ~ 4 year weekly standard deviation values of NRCS in the H-pol transmit, H-pol receive configuration on descending orbit. The x- and y-axis values are 36km grid numbers. Areas outside of the Ross and Ronne Ice Shelves exhibit steadiness on the years-long timescale.

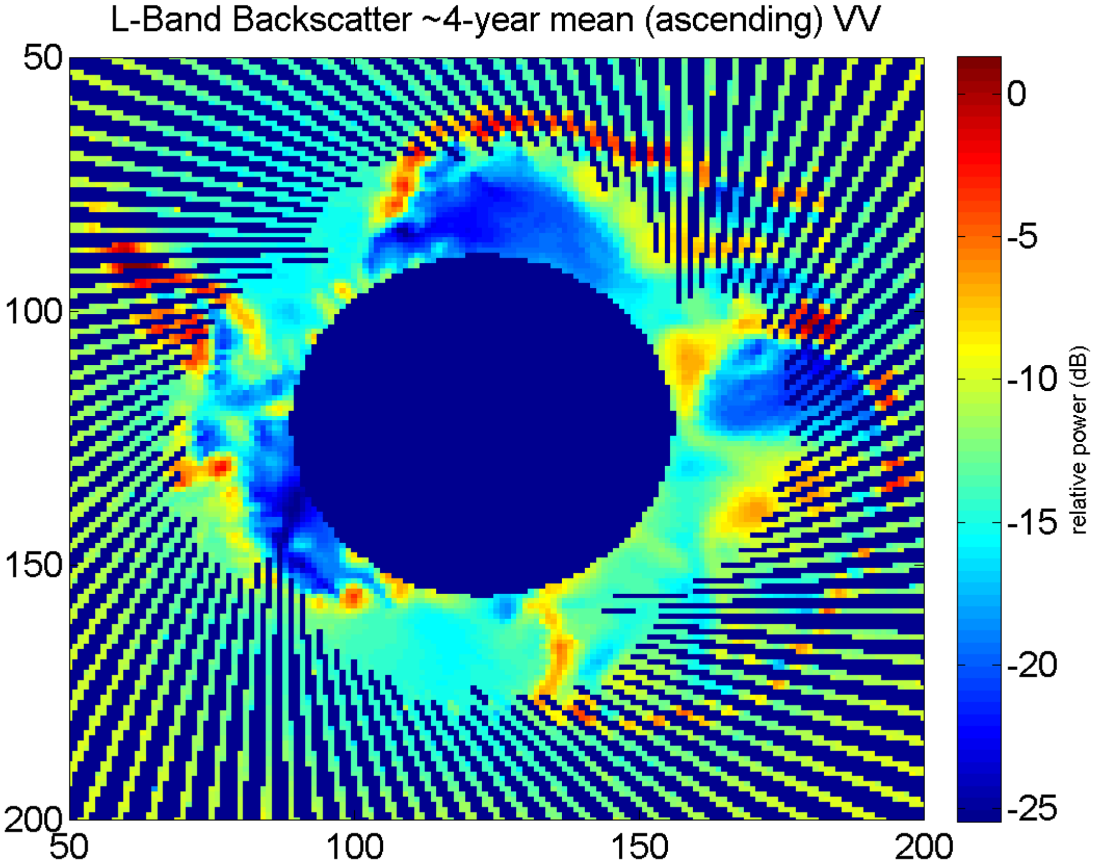

Figure A.3: The ~ 4 year weekly mean values of NRCS in the V-pol transmit, V-pol receive configuration on ascending orbit. The x- and y-axis values are 36km grid numbers.

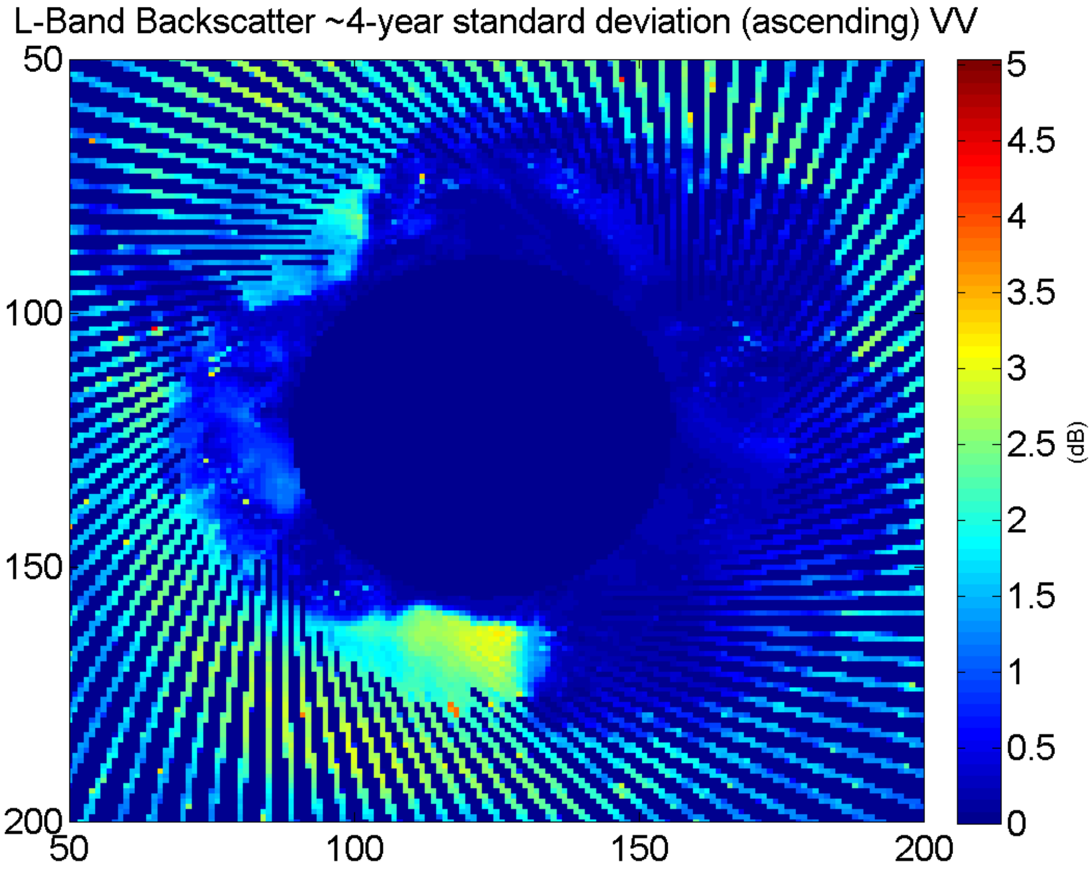

Figure A.4: The $\sim$ 4 year weekly standard deviation values of NRCS in the V-pol transmit, V-pol receive configuration on ascending orbit. The x- and y-axis values are 36km grid numbers. Areas outside of the Ross and Ronne Ice Shelves exhibit steadiness on the years-long timescale.

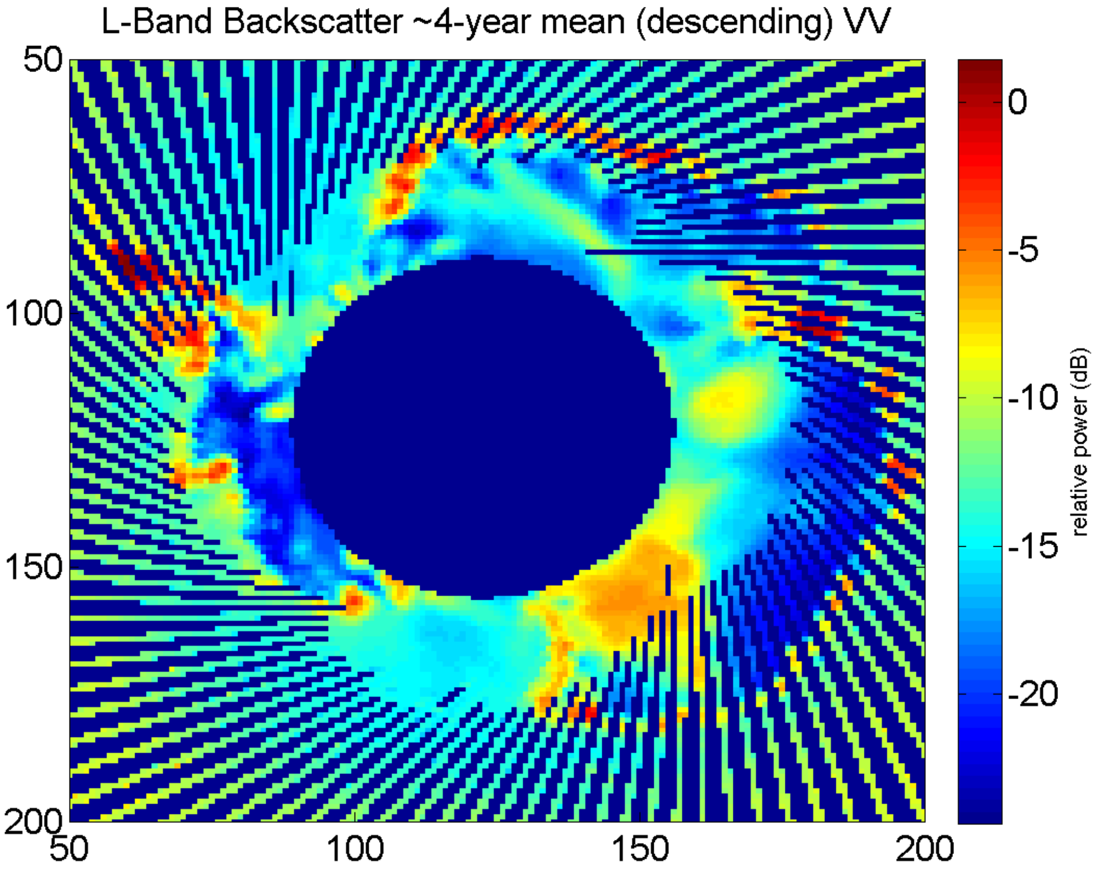

Figure A.5: The ~ 4 year weekly mean values of NRCS in the V-pol transmit, V-pol receive configuration on descending orbit. The x- and y-axis values are 36km grid numbers.

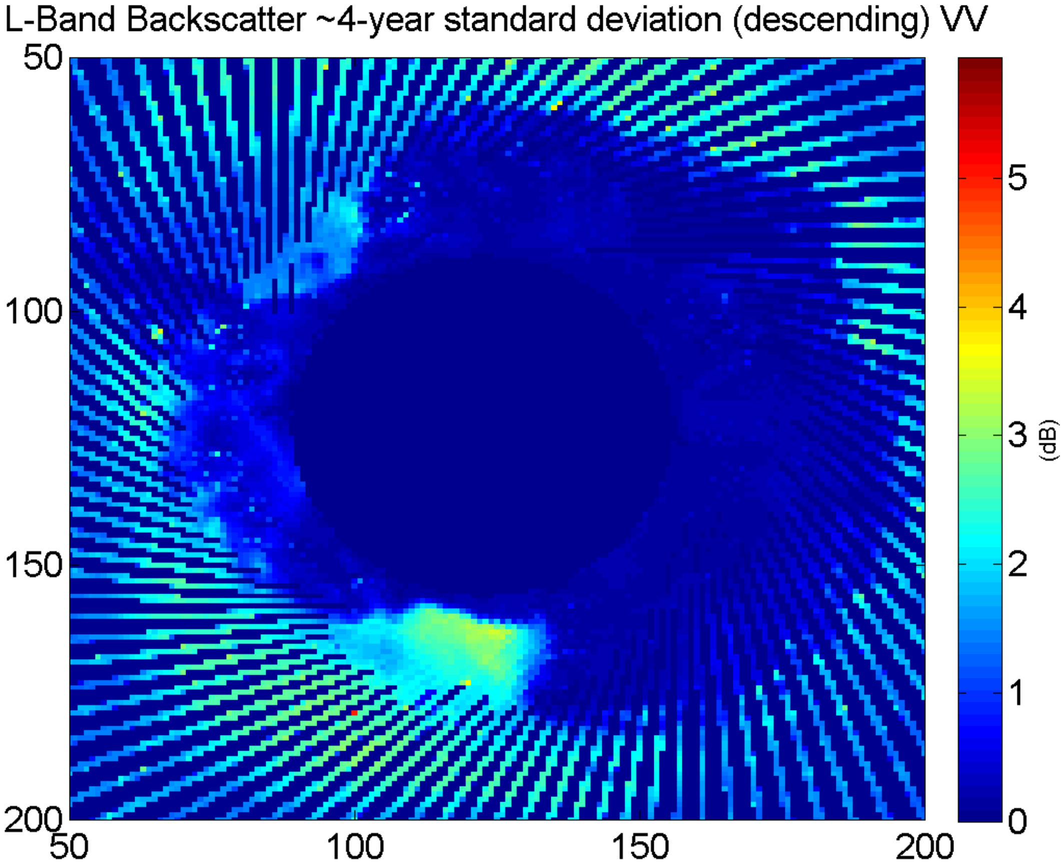

Figure A.6: The $\sim$ 4 year weekly standard deviation values of NRCS in the V-pol transmit, V-pol receive configuration on descending orbit. The x- and y-axis values are 36km grid numbers. Areas outside of the Ross and Ronne Ice Shelves exhibit steadiness on the years-long timescale.

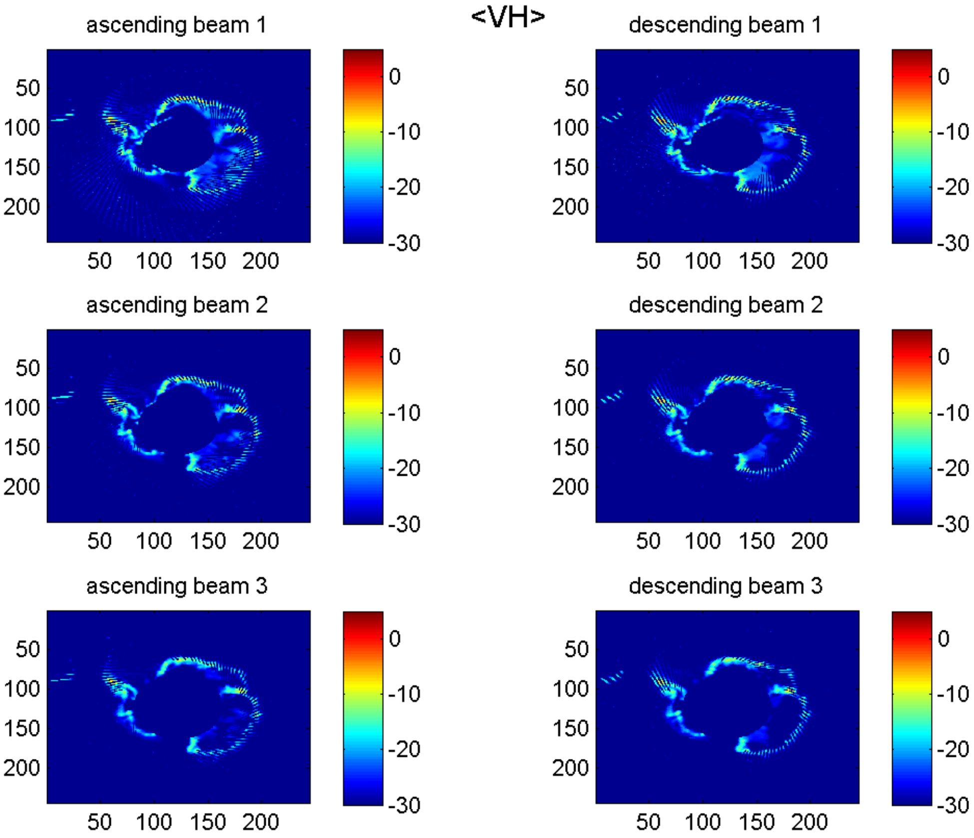

Figure A.7: The ~ 4 year weekly mean values of NRCS in the V-pol transmit, H-pol receive configuration on ascending and descending orbit in all three beams. The x- and y-axis values are 36km grid numbers. The non-zero points on the ice sheet indicate that there is some cross-polarization that occurs during reflection.

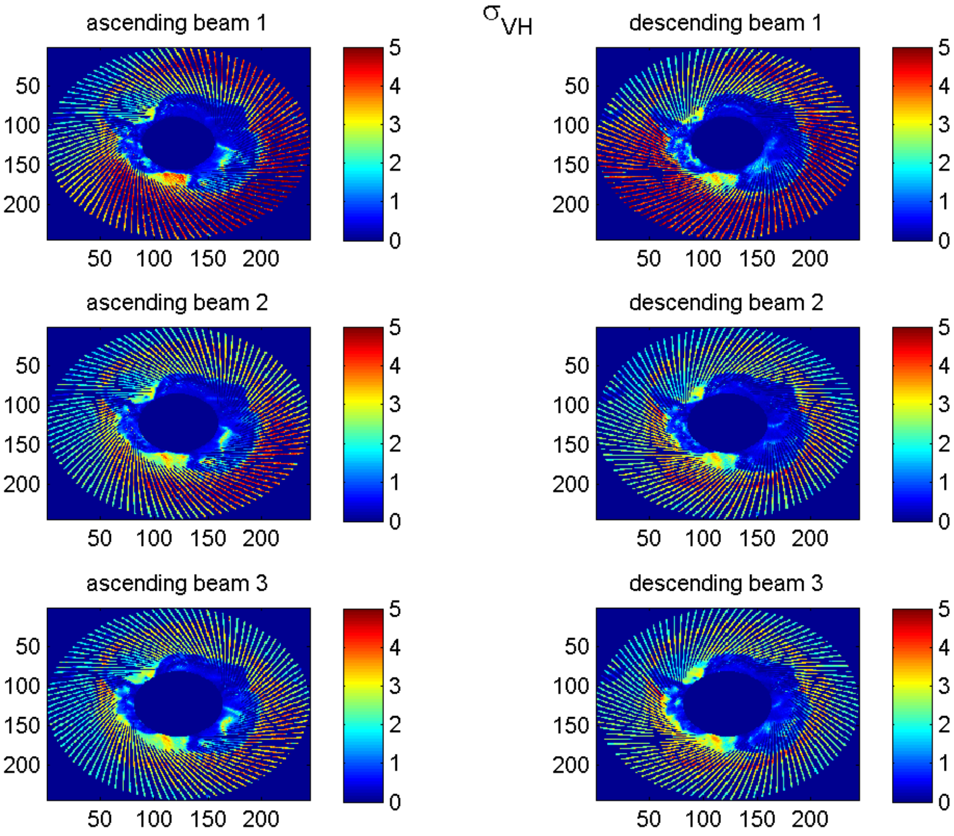

Figure A.8: The ~ 4 year weekly standard deviation values of NRCS in the V-pol transmit, H-pol receive configuration on ascending and descending orbit in all three beams. The x- and y-axis values are 36km grid numbers. Like the co-polarized standard deviations, the Ross and Ronne ice sheets show a lot of variation on the timescale of years while most of the ice sheet is relatively stable, with some isolated areas in East and West Antarctica that also display more variation than the same areas in co-polarization.

Appendix B

Attenuation Length - Additional Figures

These are additional figures related to the attenuation length analysis presented in Chap. 4.

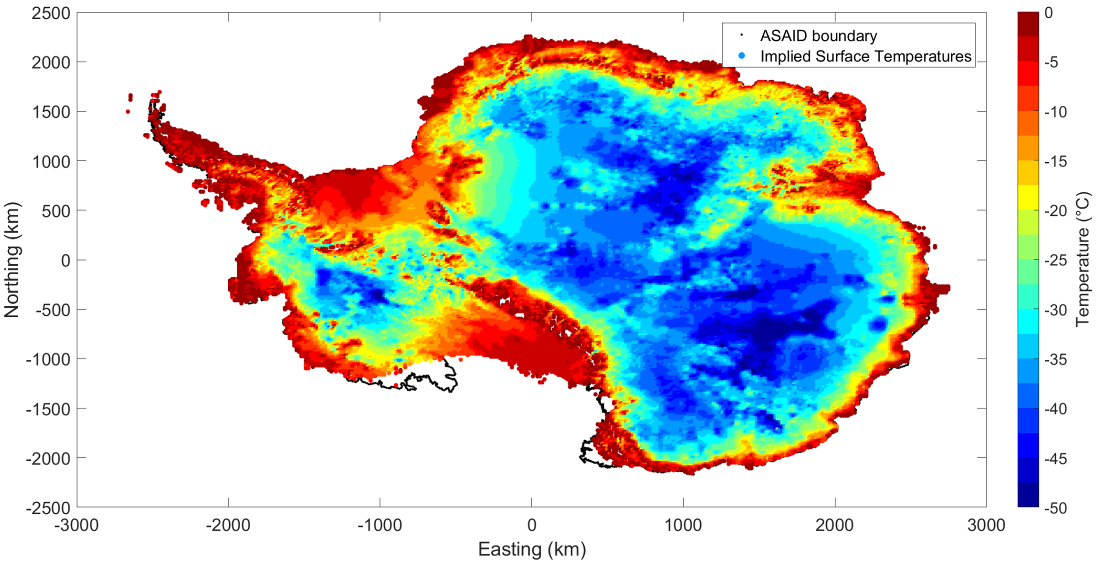

Figure B.1: Implied surface temperature from the Surface-Bottom Model. If the GRIP-like temperature model is assumed, the top-half of the ice is approximately isothermal. Solving (4.7) for the upper half (and therefore surface) attenuation length the surface temperature can be estimated by using the empirical relationship $L_\alpha = \frac{1.701}{(A+Bf^{C+1})}$, where $A = 5.03097\exp(0.134806T)$, $B = 0.172082T + 10.629$, $C = -0.00199175T - 0.703323$, f is frequency in GHz, and T is temperature in °C.

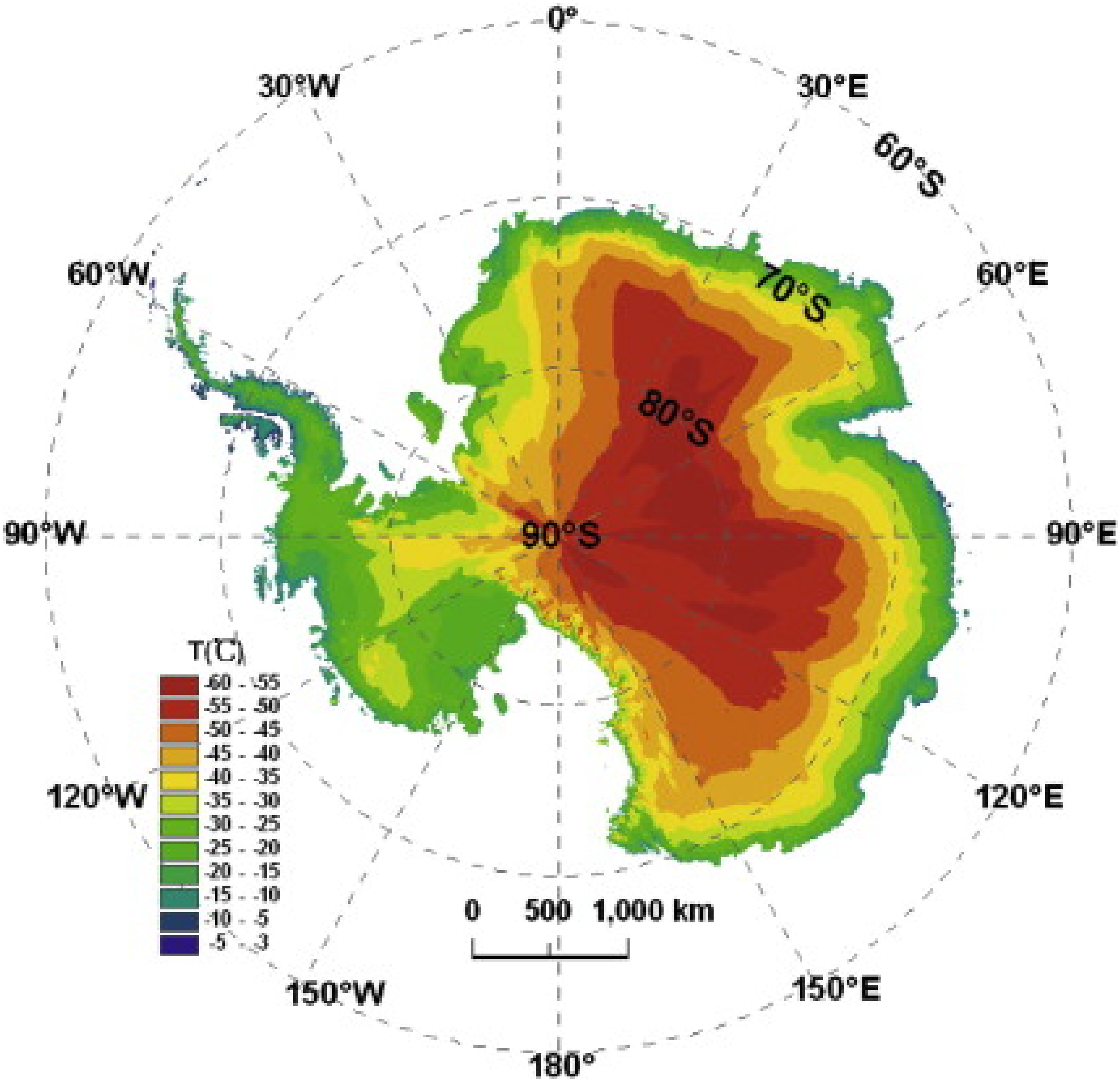

Figure B.2: Annual mean surface temperature (interpolated). Figure from [66].

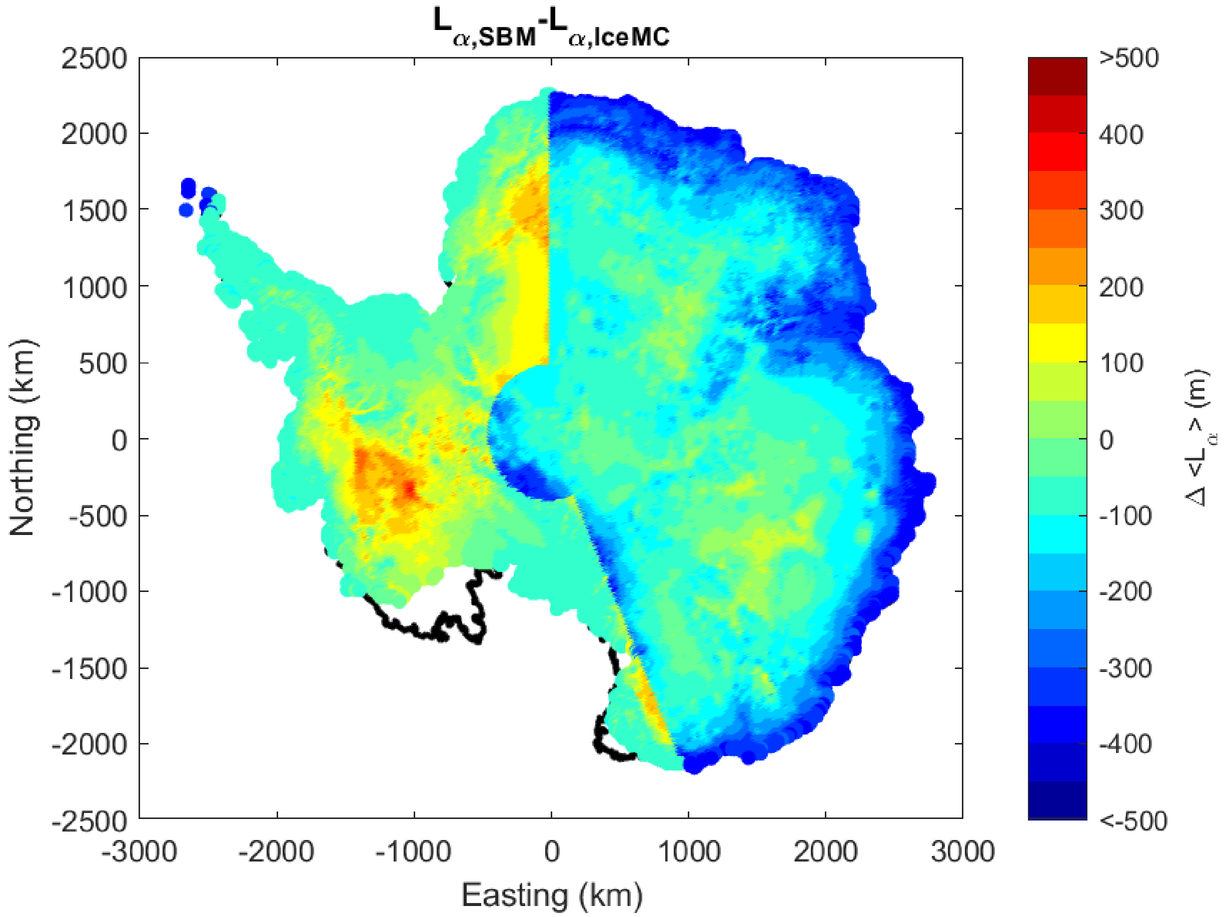

Figure B.3: Map of the differences in depth-averaged attenuation length between Surface-Bottom Model values and values from IceMC.

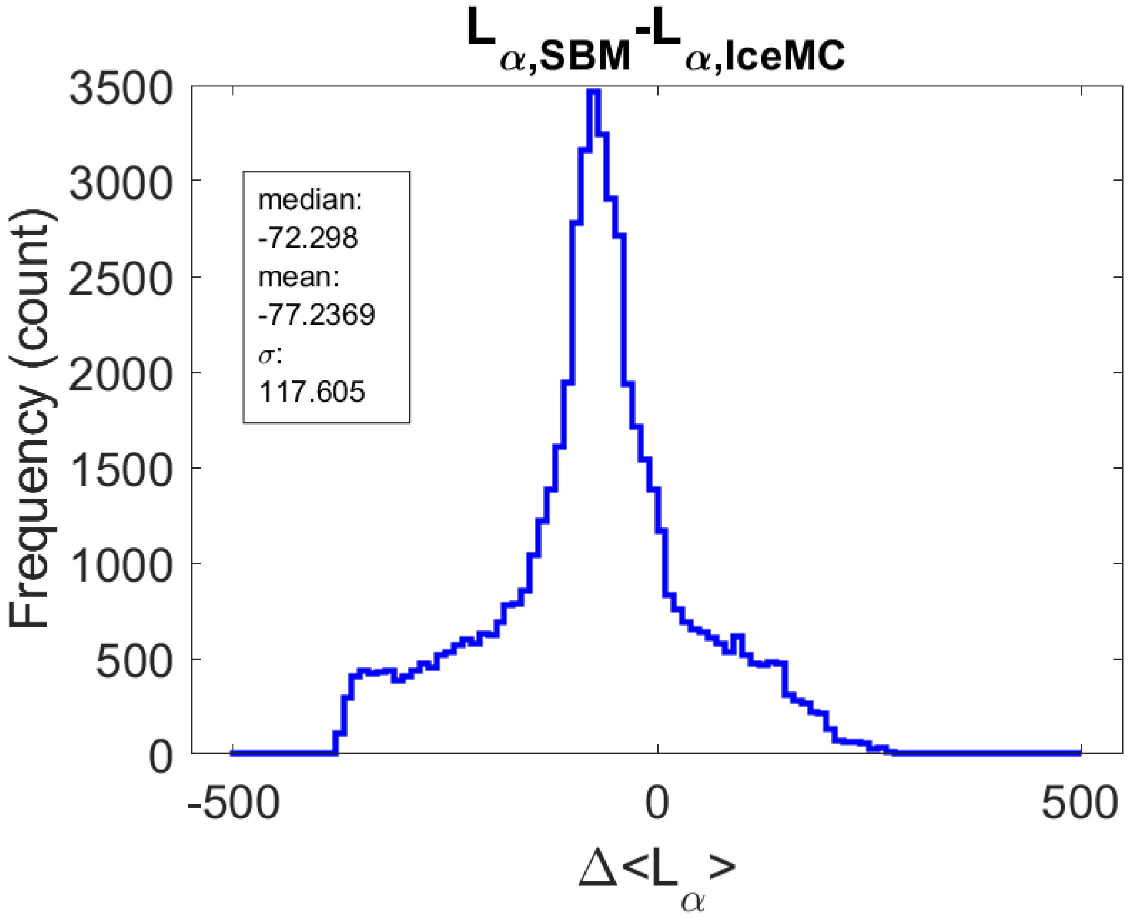

Figure B.4: Histogram of the differences in depth-averaged attenuation length between Surface-Bottom Model values and values from IceMC.

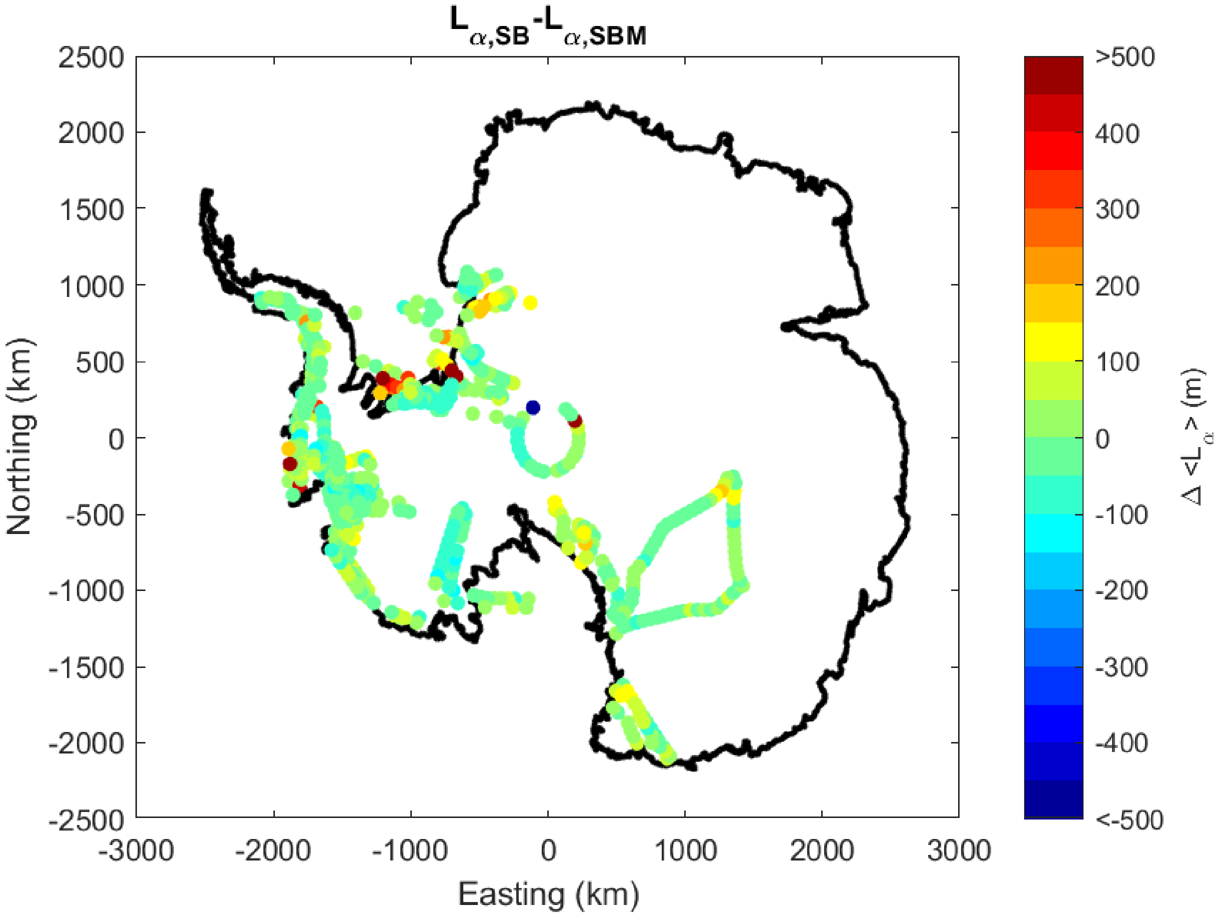

Figure B.5: Map of the differences in depth-averaged attenuation length between Surface-Bottom method measurements and values produced from the Surface-Bottom Model.

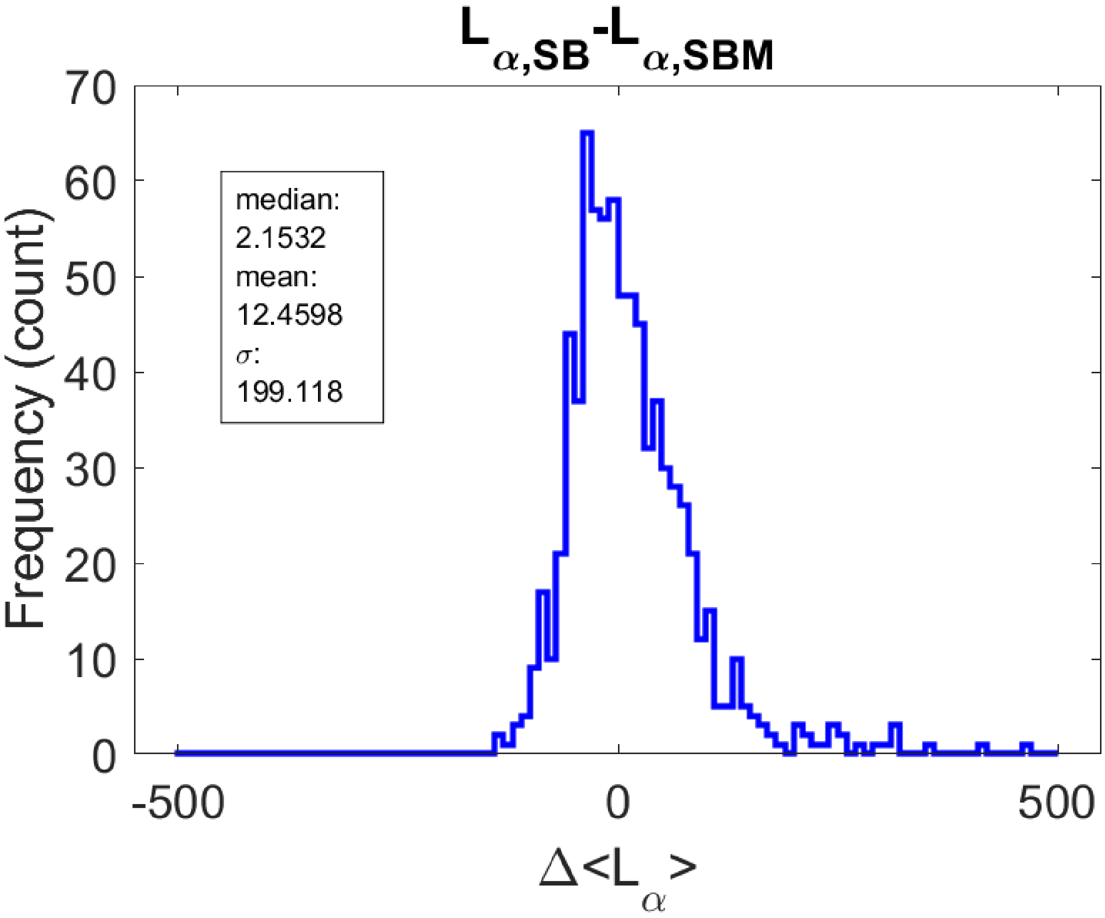

Figure B.6: Histogram of the differences in depth-averaged attenuation length between Surface-Bottom method measurements and values produced from the Surface-Bottom Model.

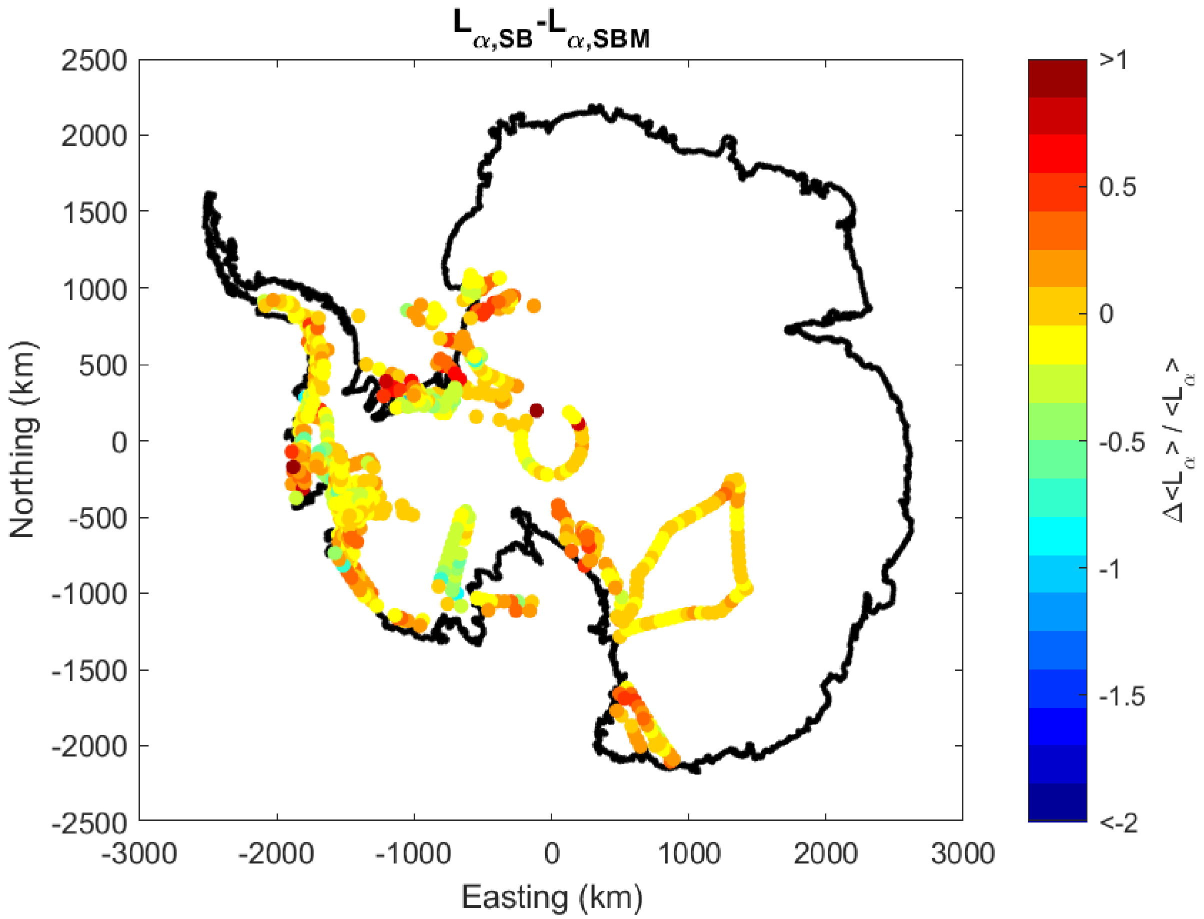

Figure B.7: Map of the fractional differences in depth-averaged attenuation length between Surface-Bottom method measurements and values produced from the Surface-Bottom Model.

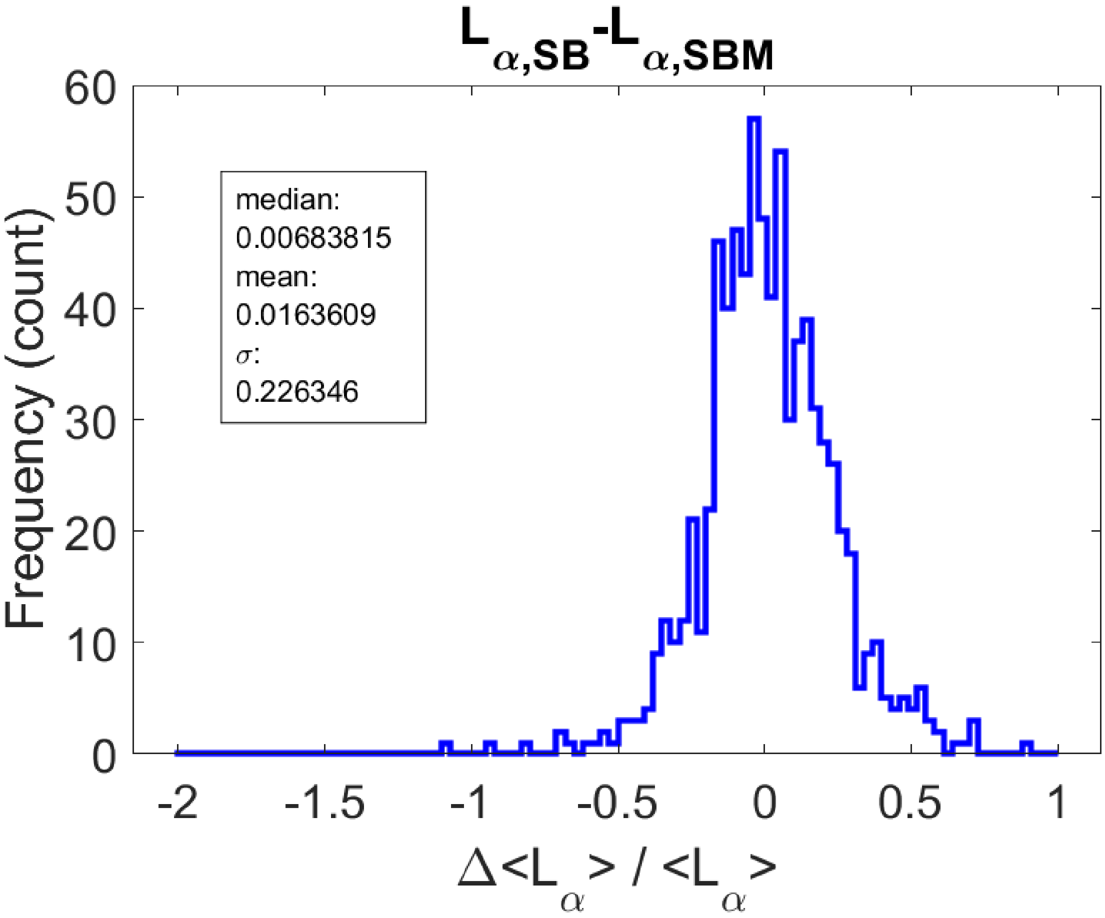

Figure B.8: Histogram of the fractional differences in depth-averaged attenuation length between Surface-Bottom method measurements and values produced from the Surface-Bottom Model.